Defect Chemistry of Bulk and Thin Film Lithium Chalcogenides

Von der Fakultät Chemie der Universität Stuttgart
zur Erlangung der Würde eines

Doktors der Naturwissenschaften

(Dr. rer. nat.) genehmigte Abhandlung

Vorgelegt von
Simon Martin Lorger
aus Limburg a. d. Lahn, Deutschland

Hauptberichter:	Prof. Dr. Joachim Maier
Mitberichter:	Prof. Dr. Thomas Schleid
Prüfungsvorsitzender:	Prof. Dr. Frank Gießelmann

Tag der Einreichung:	21.01.2019
Tag der mündlichen Prüfung:	18.03.2019

Max-Planck-Institut für Festkörperforschung
Stuttgart
2019

Erklärung über die Eigenständigkeit der Dissertation

Ich versichere, dass ich die vorliegende Arbeit mit dem Titel

Defect Chemistry of Bulk and Thin Film Lithium Chalcogenides

selbstständig verfasst und keine anderen als die angegebenen Quellen und Hilfsmittel benutzt habe; aus fremden Quellen entnommene Passagen und Gedanken sind als solche kenntlich gemacht.

Declaration of Authorship

I hereby certify that the dissertation entitled

Defect Chemistry of Bulk and Thin Film Lithium Chalcogenides

is entirely my own work except where otherwise indicated. Passages and ideas from other sources have been clearly indicated.

Name/name: *Simon Martin Lorger*

Unterschrift/signature:

Datum/date: Stuttgart, 21.01.2019

Table of Contents

Zusammenfassung

Lithiumchalkogenide (Li_2X mit X = O, S, Se oder Te) sind eine technologisch interessante Materialklasse aufgrund der hohen theoretischen Energiedichten als Batteriekonversionselektroden. Trotz chemisch einfacher, binärer Struktur und technischer Relevanz, wurden die Transporteigenschaften noch nicht für alle vier Materialien im Detail beschrieben. Die Defektchemie des Li_2X zu verstehen bildet jedoch die Grundlage für die Weiterentwicklung von Batterien und ist weiterhin elementar für die Untersuchung von komplizierteren (ternären) Lithiumchalkogeniden.

In dieser Arbeit wurden polykristalline Proben aller vier Materialien mit AC und DC Messungen untersucht, um ein Defektmodell erstellen zu können, das die Transporteigenschaften klärt. Messungen der elektromotorische Kraft zeigen, dass der ionische Transport in dieser Stoffklasse über einen weiten Lithiumaktivitätsbereich und Temperaturen bis zu 450 °C überwiegt. Die elektrischen Minoritätsladungsträger wurden in Li_2O und Li_2S mittels Hebb-Wagner Messungen untersucht, bei der σ_{eon} als Funktion der Lithiumaktivität bestimmt werden kann. Es wurde weiterhin gezeigt, dass σ_{ion} bei niedrigen Temperaturen und, wie aus dem erstellten Defektmodell vorhersagbar, für alle vier Materialien stark von der extrinsischen Donorkonzentration abhängt. Bei höheren Temperaturen wurde ein Übergang hin zum intrinsischen Bereich aufgrund der vorliegenden Frenkelfehlordnung festgestellt. Für bestimmte Dotierungen (z.B. Halogene) kommt es zu einer Verringerung der freien Lithiumleerstellen durch Assoziation an den kristallographischen Positionen der Dotierelemente, woraus auch eine verringerte Leitfähigkeit resultierte. Dotierversuche mit bekannten Konzentrationen erlaubten die Feststellung von Löslichkeitsgrenzen, die für die SEI-Eigenschaften von großer Bedeutung sind.

Diese Arbeit liefert grundlegende Daten zum Defektmodell, erlaubt dadurch die Bestim-

mung der Mobilitäten mancher Defekttypen, sowie der thermodynamischen und kinetischen Parameter wie Enthalpie und Entropie der Assoziation, Bildung und Migration, die dem Modell zu Grunde liegen. Dünne Filme von Li_2X wurden durch Sputterabscheidung und Verdampfung hergestellt, um Grenzflächeneffekte untersuchen zu können. Das Wachstum wurde zunächst mit dem Ziel optimiert, gleichmäßig dichte Filme herzustellen. Neben der strukturellen und chemischen Charakterisierung der Filme wurden deren Transporteigenschaften mit AC und DC elektrochemischen Methoden unter verschiedenen Temperatur- und Elektrodenbedingungen untersucht. Unabhängig von der Präparationsmethode wurden polykristalline, phasenreine Li_2O, Li_2S und Li_2Se Filme hergestellt, mit Korngrößen unterhalb von 100 nm. Die Leitfähigkeit der Filme parallel zur Oberfläche zeigt eine anfangs bis zu 10^4-fach erhöhte Leitfähigkeit gegenüber Pulverproben. Durch Aufheizen geht ein Teil, aber nicht die gesamte erhöhte Leitfähigkeit verloren. Ein 100-fach höheres σ_{ion} bleibt bestehen, was anhand von Grenzflächeneffekten und Dotierung diskutiert wird.

Weiterhin werden in dieser Arbeit Unterschiede und Trends in den Transporteigenschaften der Lithiuchalkogenide und im Vergleich zu den chemisch verwandten Erdalkalifluoriden diskutiert. Eine Zusammenfassung der Defektparameter zur Beschreibung der Transporteigenschaften wird gegeben, die im Falle des Li_2S einen Bereich von mehr als vier Größenordnungen in der ionischen Leitfähigkeit umfasst.

Die Anwendbarkeit der dargestellten Transporteigenschaften von Li_2X in Bezug auf Batterien hängt teils stark von deren Auftreten innerhalb der Batterie ab. Während Li_2O die thermodynamisch stabilste Verbindung als SEI an der Anode wäre, ist deren niedrige elektronische Leitfähigkeit nachteilig für eine Anwendung als Kathodenmaterial. Li_2Te hingegen zeigt eine weit höhere ionische Leitfähigkeit, wohingegen die niedrige Spannung, hohes Gewicht und Toxizität es weit weniger vorteilhaft als Kathodenmaterial erscheinen lässt. Die Untersuchung von strukturellen Defekten, wie zum Beispiel Versetzungen, und von Dotierkonzentrationen in dünnen Filmen dient weiterhin als Grundlage zur Optimierung der Transporteigenschaften der Lithiumchalkogenide.

Abstract

Lithium chalcogenides (Li_2X with X = O, S, Se, or Te) are technologically interesting for an application in energy storage devices due to their high energy density when converted in battery cathodes. Despite their chemical simplicity, the bulk transport properties have not been studied in detail for all four compounds before. Understanding the defect chemistry of Li_2X is therefore the basis for further improvements of batteries and fundamentally important for studying more complex (ternary) lithium chalcogenides.

In this work bulk, polycrystalline samples of all four materials were prepared and both a.c. and d.c techniques were used to develop a defect model that explains the transport. Electromotive force measurements show that ionic transport is dominant in this class of materials in a wide range of lithium activities and temperatures up to at least 450 °C. The minority electronic transport of Li_2O and Li_2S was investigated by using selectively blocking electrodes in a Hebb-Wagner type measurement enabling the measurement of σ_{eon} as a function of lithium activity. It was found further, that at low temperatures σ_{ion} of all four materials strongly depends on the extrinsic donor dopant concentration, as predicted from such defect models. At higher temperatures a crossover to the intrinsic regime appears due to Frenkel cation disorder. For certain dopants (e.g., halides), at low temperatures trapping of lithium vacancies at dopant sites results in a decrease in the free vacancy concentration which as a consequence lowers the conductivity. Doping studies reveal solubility limits for certain anions, which is relevant for the SEI performance in batteries.

From a fundamental point of view this work provides evidence for the defect model, enabled the determination of the mobilities of the defect species, and allows the calculation of thermodynamic and kinetic parameters such as both enthalpies and entropies of association, formation and migration. Thin films of Li_2X were prepared by both sputter deposition and

evaporation in order to study interface effects. The growth parameters were explored and adjusted to achieve uniform dense films. Besides structural and chemical characterization, the thin film transport was measured with a.c. and d.c. electrochemical methods under various temperatures and electrode configurations. All preparations yield polycrystalline phase-pure Li_2O, Li_2S, or Li_2Se with sub-100 nm grains. The in-plane ionic conductivity of the thin films is found to be initially enhanced compared to the bulk samples up to a factor of 10^4. Upon heating, some but not the entire enhancement - 100 times higher σ_{ion} - is lost which is discussed in terms of interface effects and doping.

This work compares the defect properties and discusses the differences and trends within the family of lithium chalcogenides. It further compares these properties with the chemically similar class of alkali earth fluorides. A framework of parameters is given from which transport properties can be estimated, spanning e.g. in Li_2S more than four orders of magnitude in the ionic conductivity.

From a practical point of view, the applicability of Li_2X in batteries strongly depends on the functional occurrence within the battery at the anode or cathode or both. While Li_2O is certainly the most stable compound for an SEI, its low electronic conductivity may, however, be detrimental for a cathode application. Likewise, Li_2Te shows a higher ionic conductivity, whereas the low voltage, high weight, and toxicity appear less favorable for a cathode material. The discussion of structural defects and doping dependence in thin films further provides a guide for optimizing the transport properties of Li_2X.

Previous publications

Parts of the thesis are based on the following publications by the author:
S. Lorger, R.E. Usiskin, J. Maier, Transport and Charge Carrier Chemistry in Lithium Sulfide, *Adv. Funct. Mater.*, **2019**, *29*, 1807688.

1 Introduction

1.1 Motivation

The defect chemistry of binary lithium chalcogenides (Li_2X with X = O, S, Se, Te) is important for both technological and basic scientific reasons.

Technologically, Li_2X is the discharge product in a cathode based on elemental X. It is also a key final discharge product in all conversion reactions involving the lithiation of metal chalcogenides

$$2Li^+ + 2e^- + X \rightleftharpoons Li_2X \tag{1.1}$$

$$2nLi^+ + 2ne^- + MX_n \rightleftharpoons nLi_2S + M \tag{1.2}$$

The reaction $2Li + X \rightleftharpoons Li_2X$ provides a high theoretical energy density (approximately 1800, 1160, 580 and 380 Ah/kg, respectively) compared to commercialized materials such as $Li_{1+x}(Ni_{0.33}Co_{0.33}Mn_{0.33})_{1-x}O_2$ with approximately 250 Ah/kg. Despite a lower discharge voltage and more complex reaction mechanism for these conversion reactions[1] than for intercalation reactions, conversion reactions that produce Li_2X have attracted considerable attention in recent battery investigations.[2]

A particular focus is laid on battery electrodes containing sulfur due to good reversibility, low cost, and low weight associated with the conversion reactions.

The operation of a lithium sulfur battery depends on the reversible formation of electrochemically active interfaces. In a standard battery cell, three ingredients are necessary: the active material itself needs to be sufficiently small (nano-scale) to enable a high surface-to-volume ratio and a sufficiently fast diffusion in spite of the relatively small diffusion

coefficients. In practice, these issues are addressed by nano-structuring the active materials into porous carbon matrices for electronic connection and using liquid electrolytes as an ion supply. In such an active cell, the interfaces at which the reaction takes place can hardly be controlled or studied during operation and are not fully understood.[3] This process is mainly limited by the transport kinetics of ionic and/or electronic charge carriers.

In lithium air batteries electrochemical energy is generated from the oxygenation of lithium. The mechanism of those cells is discussed based on the occurrence of LiO_2, Li_2O_2, or Li_2O, depending on electrolyte, temperature, catalyst presence, and other factors during operation.[4,5] Lithium selenide and lithium telluride have also been investigated as cathodes.[6,7] One advantage is the relatively high electronic conductivity of elemental selenium and tellurium that forms upon delithiation.

At battery anodes Li_2X formation is also common in conventional liquid batteries in the form of passivation layers, due to the thermodynamic instability of chalcogen containing liquid electrolytes under very reducing conditions. Li_2X can also slowly accumulate on the anode surface due to shuttling of polychalcogenide species from the cathode during operation, as is well-studied for polysulfides.[3] Additionally, in solid state batteries typical Li^+-conducting chalcogenide solid electrolytes are also instable in contact with low voltage anodes, and they are consequently passivated by the formation of a Li_2X containing solid electrolyte interface (SEI). The transport properties of this SEI are critical to the overall battery performance: the ionic conductivity must be high enough to enable rapid Li^+ insertion and extraction from the anode, while the electronic conductivity must be low in order to slow SEI growth and the associated electrolyte decomposition and increased ion transfer resistance. Technologically, the main use of lithium oxide is found as an additive in ceramics, glass and glaze production, and, due to the high lithium density, it was investigated as a potential breeder material in the fusion reactor process.[8] In all these applications above, defect transport is critical and can limit the overall battery performance.

Lithium chalcogenides are also interesting from a crystal-chemical perspective. The inverse structure to Li_2X is the fluorite structure realized typically for alkali earth fluorides, that is well-studied in terms of transport properties. It has been hypothesized that many properties are analogous to Li_2X with antifluorite structure.[9–12] An understanding of the

charge carrier behavior, as achieved here, provides a foundation for investigating the defect chemistry in more detail and allows for a pertinent comparison. It also forms the base for the investigation of more complex compounds, e.g. ternary lithium chalcogenides.

Besides bulk transport phenomena, the transport across or along interfaces is particularly important for the understanding of energy storage devices. Especially in conversion reaction cathodes, every charge and discharge cycle depends on electrochemically active interfaces and their transport properties. In related ionic conductors fundamentally interesting transport phenomena are observed that, if present for Li_2X, may have significant impacts on battery applications as well. If one considers only the anode electrolyte interface in a battery, which consists of a complex mixture of different compounds, transport may involve interface effects arising from grain boundaries, doping, or even amorphous contents. These phenomena may strongly affect the SEI behavior. For example, one might predict enhanced Li^+ transport at Li_2O/Li_2S interfaces, by analogy with the enhanced transport observed at CaF_2/BaF_2 interfaces.[13] The transport properties in lithium chalcogenides are probed in thin films for those reasons in this work as well.

1.2 Literature review on bulk lithium chalcogenides

1.2.1 Structure and stability

All four binary lithium chalcogenides crystallize in the antifluorite structure,[14] as illustrated in Figure 1.1. In the antifluorite structure, anions (grey) form a face-centered cubic (fcc) substructure while the smaller lithium cations (green) occupy the tetrahedral voids (2 per anion). Fairly large empty octahedral voids (1 per anion) enable the structure to take up ions interstitially. Note that the fluorite structure has an identical space group ($Fm\bar{3}m$) and structure, except with cations forming the fcc lattice of immobile counterions while the much smaller fluoride anion is mobile.

No crystallographic phase transitions in Li_2X are reported up to the melting points at ambient pressure.[14] High pressure studies (above 12 GPa) reveal a phase change to the hexagonal anticotunnite structure (*Pnma*) for Li_2S;[15] an analogous transition is observed

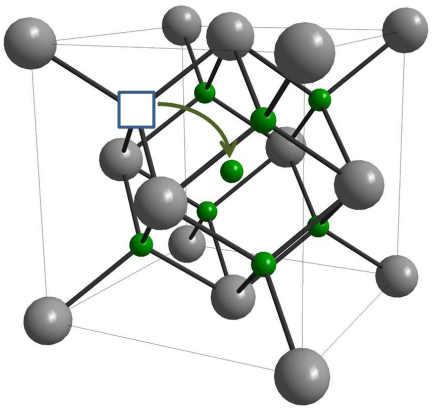

Figure 1.1: Unit cell of the antifluorite structure ($Fm\bar{3}m$). The arrow shows the formation of a Frenkel cation defect.

in fluorite-structured PbF_2 (cotunnite) as well.[16,17] The sizes of the corresponding anions and interstitial sites in Li_2X are given in Table 1.1 together with possible substitutes for the anion. Mg^{2+} (0.57 *Å*), Cu^{2+} (0.57 *Å*), Zn^{2+} (0.60 *Å*), or Fe^{2+} (0.63 *Å*) have comparable ionic radii to Lithium (0.59 *Å*) and can replace it substitutionally. All ionic radii in this work are cited from Shannon *et al.*[18] Ionic radii depend on coordination number which varies in antifluorites depending on the site of added dopant. For ease of comparison, ionic radii are quoted for a coordination number of six unless otherwise noted.

Table 1.1: Ionic radii in *Å* for the relevant anion dopants of Li_2X.

Coordination #	unit cell	X^{-2} 6	F^- 6	Cl^- 6	Br^- 6	I^- 4	N^{3-} 4	Intersitial void
Li_2O	4.62[14]	1.40	1.33				1.46	1.24
Li_2S	5.72[19]	1.84		1.81				1.72
Li_2Se	6.01[14]	1.98			1.96			1.85
Li_2Te	6.52[14]	2.21				2.21		2.06

Phase diagrams for the lithium chalcogenides are shown in Figure 1.2.

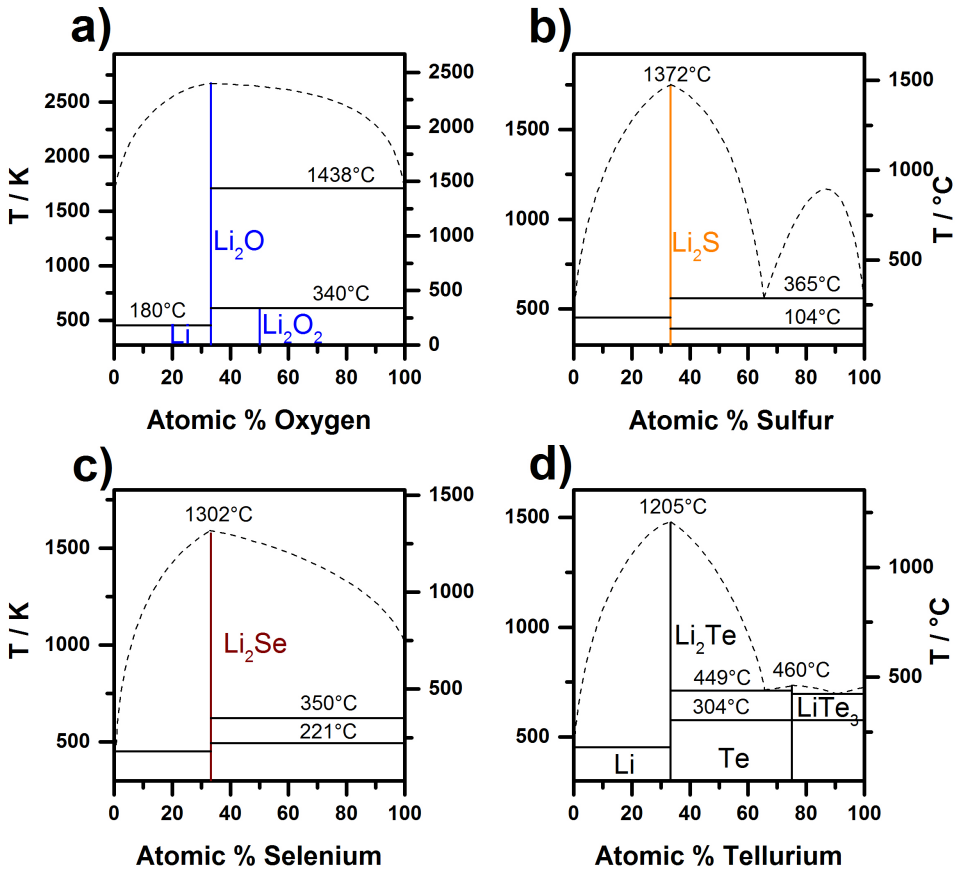

Figure 1.2: Phase diagrams of Li_2X adapted for a) Li_2O,[20] b) Li_2S,[21] c) Li_2Se,[22] and d) Li_2Te.[23] In this work the line compounds Li_2X are investigated.

The most stable compound at ambient pressure below 250 °C in the Li-O_2 system is lithium peroxide according to Figure 1.3. The decomposition voltage of Li-O_2 versus metallic lithium, calculated from thermodynamic data, is shown in Figure 1.3a) as a function of temperature and in b) as a function of pO_2. In this work, Li_2O was handled exclusively in low pO_2 environments (glovebox for bulk samples, high vacuum for thin films) where Li_2O_2 is not stable. The defect chemistry of Li_2O_2 was investigated in detail by Gerbig *et al.*.[24] The superoxide LiO_2 was proposed to form as a metastable product before oxidation to the peroxide takes place in Li-air batteries.[25] In the present work no peroxide or superoxide species were ever observed, yet peroxide species may occur as point defects in the Li_2O structure.[26] Furthermore, thermogravimetric analysis of the peroxide shows in-

stability above 400 °C and of lithium hydroxide above 600 °C at ambient pressure.[24] The annealing procedure of several hours at 900 °C, as described in chapter 4, is sufficient to decompose the peroxide and hydroxide (and carbonate) into Li_2O.

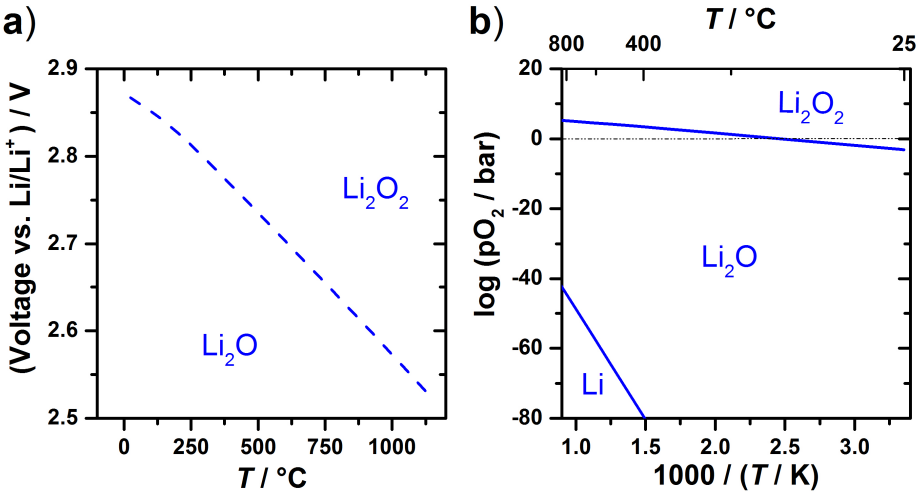

Figure 1.3: Thermodynamic stability of Li_2O versus lithium and versus oxygen partial pressure pO_2(calculated according to JANAF tables).[27]

It was shown that polychalcogenides can form in solution in the Li-S,-Se and -Te systems,[28–30] however, they are rarely found in solid state and were not observed in this work.

1.2.2 Lithium oxide

There is general consensus that charge transport in Li_2O is dominated by lithium ions over a wide range of conditions. Of all the Li_2X compounds, Li_2O is the most well-studied, because it was a candidate blanket material for fusion reactors at high temperatures. Radiation with γ-rays on Li_2O was shown to create oxygen vacancies[31] and peroxide species as defects.[26] The oxygen vacancies can further trap electrons to form so-called F-centers.[32] Electron paramagnetic resonance studies indicate the possibility of hydrogen in interstitial sites having an eight-fold coordination of lithium ions.[33] Under very reducing conditions, the self-diffusion of hydrogen species in Li_2O (hydrogen, deuterium and tritium) was measured and found to be orders of magnitude lower than that of lithium species.[34] Isotope

exchange experiments indicated that the lithium self-diffusion[35] is several orders of magnitude higher than the oxygen self-diffusion.[36,37]

Additionally, many experimental reports exist on lithium transport. Both transport in polycrystalline and single crystal Li_2O[38] show predominant ionic conduction by comparing NMR[10,39,40] and impedance spectroscopy results[12,41–46] in the range 200 °C to 900 °C. Good agreement is generally obtained, as shown below in Figure 4.10. Between 650 - 800 °C a change in activation energy is typically observed, which most authors attributed to an extrinsic-to-intrinsic transition. Transport in nanosized Li_2O was investigated as well by Indris *et al.*.[45] Micro-sized particles were ball-milled to achieve nanopowder that did not exhibit altered transport compared to the bulk. Doping studies with fluorine or magnesium ions[39] revealed that lithium vacancies are the mobile defect species, and evidence on vacancy-dopant association was seen below 250 °C.[40,47]

Molecular dynamics studies[16,48–55] concluded that vacancy transport dominates at low temperature,[49] while more complex transport phenomena were reported at higher temperatures as well, including vacancy,[53,54] interstitial,[49–51] and cooperative motion.[48] At high temperatures an interstitial mechanism was suggested from neutron scattering.[52]

All these findings are in qualitative agreement with a defect model based on Frenkel cation disorder. However, the derived model parameters exhibit significant scatter. Specifically, the enthalpies of Frenkel disorder, vacancy migration, and interstitial migration vary between 1.1 to 2.5 eV, 0.3 to 1.0 eV, and 0.6 to 1.2 eV, respectively. These discrepancies are partially due to incorrect or missing defect chemical modeling and hence to an incorrect data interpretation.

1.2.3 Lithium sulfide

Isolated aspects of the defect chemistry of Li_2S have been studied in the literature, but a unified model is lacking. Several groups have measured the ionic conductivity by impedance spectroscopy[10,41,56–58] or nuclear magnetic resonance (NMR).[10] The measurements show consistent conductivities between most reports,[10,41,57,58] however, the values reported by Lin *et al.*[56] are anomalously low as will be discussed further in chapter 4. The same pub-

lication suggested that nanosized Li_2S shows 100x enhanced transport compared to bulk material. A change in activation energy was usually observed between 500 - 600 °C, which is typically attributed to the extrinsic to intrinsic transition.[10] However, the reported activation energies by Mousa *et al.* were different between NMR and conductivity measurements even though using same polycrystalline starting material, which was not explained. It was observed by Raman spectroscopy[9,59] and neutron scattering,[60] that changes in the [100] phonon modes, C11, C12 elastic constants, and in the temperature dependence of the (111) Bragg reflection, respectively, appear around the same transition temperature. Despite the absence of a change in lattice symmetry, a so-called diffuse phase transition was assumed to cause such changes.[9,58–60]

There is also disagreement on the dominant defect migration mechanism. From quasielastic neutron scattering measurements, lithium ion hopping between interstitial and regular lattice sites was claimed at 900 - 1100 °C,[61] with interstitial concentrations as high as 14% at 1050 °C obtained by refinements.[60] Impedance measurements by Schoch *et al.*[57] reported a decreased conductivity with increasing sulfur partial pressure, which also suggests an interstitial mechanism. However, Huggins[41] found a higher conductivity and lower activation energy when using Li electrodes under He atmosphere than when using Mo electrodes under vacuum. While this comparison suggests an interstitial mechanism, the conductivity also decreased with time when using Li metal electrodes, which suggests a vacancy mechanism. Both Schoch *et al.* and Huggins[41,57] noted that the ionic conductivity can vary by orders of magnitude at lower temperatures, depending on sample preparation and measurement conditions. Moradabadi and Kaghazchi[62] found a lower formation energy for lithium interstitials but a lower enthalpy of migration for lithium vacancies using density functional theory (DFT) calculations. Overall a vacancy mechanism was concluded to be more favorable. DFT calculations by Kim *et al.*[63] agreed with this finding based on *ab-initio* molecular dynamics simulations. Jand *et al.*[64] reported a superionic phase transition at 630 °C, arguing that vacancies are dominant below this temperature and interstitials, due to an increasing concentration, above this temperature.

1.2.4 Lithium selenide and lithium telluride

Despite growing interest in using both Li_2Se and Li_2Te in batteries, the ionic and electronic transport has not been investigated in the literature. A superionic phase transition was reported[65] with an increasing lithium density at interstitial positions above 600 and 800 °C for Li_2Se and Li_2Te, respectively. DFT results on Li_2Te report an activation energy of 0.25 eV[66] for lithium self-diffusion including an interstitial transition state.

1.3 Thin Films

1.3.1 Growth

Several methods are reported for the growth of Li_2X thin films. Sputter deposition of Li_2O was reported to be challenging due to an unstable plasma, target instability causing cracks, and presumably oxygen loss in the target.[67,68] Hence, pure phase Li_2O thin films are yet unreported. Li_2S thin films have been prepared and tested in battery applications. Using atomic layer deposition 100 nm layers of amorphous Li_2S were obtained that show good battery cycling.[69] Sputter deposition of Li_2S led to polysulfide species for as-grown films, also showing good cycling kinetics, while crystalline Li_2S formed by high temperature annealing was claimed to be electrochemically inactive.[70]

Reports on composite thin films containing B_2O_3[71] or Al_2O_3[72] or other glass network former with Li_2X exist as well as ternary and quaternary compounds.[73–75]

1.3.2 Benefits of thin film investigations

Thin films exhibit several important differences from bulk materials: Preparing thin films requires well controlled substrate interfaces, which can control and alter the overall properties of the film compared to the bulk. Strain between thin film and substrate due to lattice mismatch can impact the growth: when the lattice mismatch is negligible, epitaxial films can be grown which may be difficult to grow in macro-sized crystals. Furthermore, crystal orientation can dictate the orientation of the growing film. As a result surfaces can be tailored and

measured, that are not easily accessible in the bulk. When the mismatch is small, thermodynamically unstable phases in the bulk can be stabilized, and when mismatch is large dense nanocrystalline films can be grown. All these morphological aspects can influence the transport, optical or other physical properties. Depending on preparation technique, metastable compositions may be frozen in during preparation that can not be achieved easily in the bulk. Patterning of the thin film or contacts is technologically important for measurements and device preparation, which is difficult in the bulk. Moreover, extreme aspect ratios can be achieved and size effects can be investigated. Small sample size and little material can be used which may be more cost-effective for large scale production. Transport processes can be investigated at thin film interfaces in composites, with well-controlled geometry, as well. In general, thin films show a higher proportion of interfacial effects, and bulk and interface effects can be separated by thickness variations.

In light of the possible analogy between antifluorite and fluorite compounds, it is also relevant to review thin film studies of the latter. As such, enhanced ionic conductivity was observed at interfaces of CaF_2/BaF_2 heterolayers due to a transfer of F^- from BaF_2 to CaF_2.[13] Such redistribution was fully explained using a space charge model.[76,77] Cation intermixing and disorder induced by high energy ball milling of CaF_2/BaF_2 mixtures led to an even higher conductivity.[78] Space charge effects can further arise between same grains, e.g. in CaF_2, as well.[79] In particular, in nanocrystalline samples the volume fraction of particle-to-particle interfaces can dominate the whole sample volume. When interfaces are percolating or when the grain size approaches the dimension of the charged interface region (nm range), the space charge can percolate throughout the sample and lead to an enhanced transport.[80] Interface regions can further be altered by surface treatments: BF_3 or SbF_5 vapor treatment of CaF_2 surfaces activates the grain boundary regions for transport. Adsorption of these lewis acids increases the fluorine vacancy concentration at the surface of CaF_2 which influences the conductivity directly.[81,82]

These transport effects are not a peculiarity of fluorites but have been observed e.g. for lithium halides. Both LiI/Al_2O_3 composites[83] and LiI thin films on Al_2O_3[84] were reported to have enhanced transport compared to the pure ionic conducting bulk LiI. More recently LiF thin films sputtered on various substrates are investigated in terms of space charge zones

as well.[85] Similar features are obtained for silver halide mixtures, where space charge effects can cause enhanced transport, too.[86] Furthermore, for individual single phase AgCl, grain boundaries[87] and individual grain surfaces[88] show enhanced transport as shown by microcontact impedance measurements.

Turning to lithium conductors, these effects are largely unexplored despite the growing interest for lithium ion batteries.

1.4 Outline of this thesis

All of these findings explain the fundamental interest to study bulk transport and interface effects in antifluorite Li_2X. A clearly defined reference state of bulk Li_2X is necessary before investigating space charge effects and thin film transport and this work therefore starts with the investigation of the charge carrier chemistry of bulk Li_2X.

In this work a defect chemical model is constructed for the binary lithium chalcogenide class in chapter 2 from the well known defect chemical treatment provided by the literature. Even though certain aspects of the charge carrier chemistry have been addressed for bulk Li_2O and Li_2S previously, a unified treatment providing thermodynamic and kinetic parameters was lacking especially for Li_2Se and Li_2Te. Experimental details are discussed in chapter 3. The ionic transport is analyzed for bulk samples in chapter 4 for a range of temperatures and doping concentrations. A comparison of the defect chemistry with the well studied class of alkaline earth fluorides is drawn as well, showing besides structural similarities that the trends in defect chemistry are very similar. Thin films are successfully grown in pure phase by two different techniques and electrochemically investigated as reported in chapter 5. In particular, films grown by molecular beam epitaxy (MBE) have not been reported in the literature yet but are successfully grown here. The implications for batteries will be discussed at the end in chapter 6.

The current work gives therefore insight into the underlying charge carrier chemistry of Li_2X that allows for further investigation of other defect phenomena and gives insight into technologically important key parameter for the prediction of lithium battery SEI or cathodes.

2 Theoretical background

2.1 Defect chemistry of lithium chalcogenides

The transport properties in Li_2X (X = O, S, Se, or Te) depend on the ionic and electronic defects whose concentrations may vary by orders of magnitude depending on small but non-negligible deviations in the stoichiometry. The defect model below is constructed for lithium chalcogenides based on well known concepts developed for a variety of other ionic crystals.[89–93] Typical compounds such as the fluorites[94] or Na_2S,[11] or Li_2O_2,[24] and numerous metal halides[89] including AgCl, LiF,[95] or NaCl,[96,97] exhibit typically three regimes in conductivity measurements as a function of temperature. This thesis will show that the chemistry of all four Li_2X materials is well-described for the first time fully by a charge carrier model based on Frenkel cation disorder, migration of both cation vacancies and interstitials, and association between vacancies and positive dopants. Following these assumptions, first the defect thermodynamics are constructed for Li_2O, followed by a kinetic model based on ion hopping, which will be validated in chapter 4.

2.1.1 Defect thermodynamics

The general defect equilibria describing the formation of dilute point defects and the corresponding mass action laws are:

$$\mathrm{Li}_{\mathrm{Li}}^{\times} + V_i^{\times} \rightleftharpoons \mathrm{Li}_i^{\bullet} + V_{\mathrm{Li}}' \qquad \text{with} \qquad K_F = [\mathrm{Li}_i^{\bullet}][V_{\mathrm{Li}}'] \tag{2.1}$$

$$\mathrm{O}_{\mathrm{O}}^{\times} + V_i^{\times} \rightleftharpoons \mathrm{O}_i'' + V_{\mathrm{O}}^{\bullet\bullet} \qquad \text{with} \qquad K_{\bar{F}} = [\mathrm{O}_i''][V_{\mathrm{O}}^{\bullet\bullet}] \tag{2.2}$$

$$2\mathrm{Li}_{\mathrm{Li}}^{\times} + \mathrm{O}_{\mathrm{O}}^{\times} \rightleftharpoons V_{\mathrm{O}}^{\bullet\bullet} + 2V_{\mathrm{Li}}' + \mathrm{Li}_2\mathrm{O} \qquad \text{with} \qquad K_S = [V_{\mathrm{O}}^{\bullet\bullet}][V_{\mathrm{Li}}']^2 \tag{2.3}$$

$$\mathrm{Li}_2\mathrm{O} + 3V_i^{\times} \rightleftharpoons 2\mathrm{Li}_i^{\bullet} + \mathrm{O}_i'' \qquad \text{with} \qquad K_{\bar{S}} = [\mathrm{Li}_i^{\bullet}]^2[\mathrm{O}_i''] \tag{2.4}$$

$$\mathrm{nil} \rightleftharpoons \mathrm{e}' + \mathrm{h}^{\bullet} \qquad \text{with} \qquad K_b = [\mathrm{e}'][\mathrm{h}^{\bullet}] \tag{2.5}$$

Here Kröger-Vink nomenclature is used: $[\mathrm{Li}_i^{\bullet}]$ equals the concentration of the given element on an interstitial site with +1 effective charge relative to that site in the perfect crystal; $[V_{\mathrm{Li}}']$ is the concentration of a vacancy on a lithium site with effective -1 charge; neutral effective charges are labeled by $\times$, and $[\mathrm{e}']$ and $[\mathrm{h}^{\bullet}]$ refer to the concentration of excess electrons and electron holes. Reactions 2.1-2.5 are the cation-Frenkel- (2.1), anion-Frenkel- (2.2), Schottky- (2.3), Anti-Schottky- (2.4), and the band-equilibrium reactions (2.5).

It was shown for $\mathrm{Li}_2\mathrm{O}$,[36] that the oxygen self-diffusivity is orders of magnitude lower than for lithium and that the Schottky formation enthalpy is high (5.15 eV[12]). From optical absorption measurements in $\mathrm{Li}_2\mathrm{O}$ it was concluded that the band gap is at least 4.4 eV[98] or higher (6.6 eV[99]) and it is therefore assumed, that intrinsically electrons and holes are minority charge carriers, $K_F \gg K_B$. Additionally, K_B values have been calculated by DFT to be 4.6 eV (or higher for $\mathrm{Li}_2\mathrm{O}$[98–101]), 3.0 eV (or higher for $\mathrm{Li}_2\mathrm{S}$[62,63,102–105]), 4.1 eV ($\mathrm{Li}_2\mathrm{Se}$[106]), and 2.2 eV (or higher for $\mathrm{Li}_2\mathrm{Te}$[102,107,108]). The antifluorite structure provides empty interstitial sites, however, the anion-Frenkel (i.e., formation of anion interstitials and vacancies) and anti-Schottky reactions i.e., formation of anion and cation interstitials) are not favorable, since both require the formation of a chalcogen ion on an interstitial position that is too small to accommodate the anion. Therefore, the anion defect concentration is expected to be frozen in and predominant intrinsic ionic disorder due to the cation-Frenkel equilibrium reaction is expected. The empty interstitial position is suitable for lithium defects. At

high temperatures, where intrinsic disorder prevails (intrinsic region), the concentrations of lithium vacancies and interstitials will follow from

$$K_F = [\mathrm{Li}_i^{\bullet}][V'_{\mathrm{Li}}] = N_i N_{\mathrm{Li}} \exp\left(\frac{\Delta_F S^{\circ}}{k_B}\right) \exp\left(-\frac{\Delta_F H^{\circ}}{k_B T}\right) \tag{2.6}$$

where $N_i = {}^{4}/_{a_0^3}$ and $N_{\mathrm{Li}} = {}^{8}/_{a_0^3}$ are the concentrations of available interstitial and lithium sites, a_0 is the lattice parameter of Li_2X (Table 1.1), while $\Delta_F H^{\circ}$, $\Delta_F S^{\circ}$, k_B and T denote the standard enthalpy and entropy of Frenkel cation defect formation, Boltzmann's constant, and temperature, respectively. If a positively charged dopant is added with a concentration C, charge neutrality requires that predominantly lithium vacancies form accordingly to balance the additional charge. At medium temperatures, i.e., in the extrinsic regime, $\sqrt{K_F} < C$ and consequently the concentration of lithium vacancies is fixed. Higher valent metal impurities act as positive dopants, whereas on the anion lattice site substitution by pnictides leads to negative and by halogenides to positive dopants. Some possible anion dopants are listed in Table 1.1,[18] and some example doping reactions are:

$$\mathrm{MgO} + 2\mathrm{Li}_{\mathrm{Li}}^{\times} \rightleftharpoons \mathrm{Li_2O} + \mathrm{Mg}_{\mathrm{Li}}^{\bullet} + V'_{\mathrm{Li}} \tag{2.7}$$

$$2\mathrm{LiF} + \mathrm{O}_{\mathrm{O}}^{\times} \rightleftharpoons \mathrm{Li_2O} + \mathrm{F}_{\mathrm{O}}^{\bullet} + V'_{\mathrm{Li}} \tag{2.8}$$

$$\mathrm{Li_3N} + \mathrm{O}_{\mathrm{O}}^{\times} \rightleftharpoons \mathrm{Li_2O} + \mathrm{N}'_{\mathrm{O}} + \mathrm{Li}_i^{\bullet} \tag{2.9}$$

$$\mathrm{H_2O} + \mathrm{O}_{\mathrm{O}}^{\times} + \mathrm{V}_{\mathrm{O}}^{\bullet\bullet} \rightleftharpoons 2\mathrm{OH}_{\mathrm{O}}^{\bullet} \tag{2.10}$$

Additionally, the antifluorite structure provides large interstitial sites in which impurity ions can be added. As an example the formation of F^- interstitials can be formulated as

$$\mathrm{LiF} + 2V_i^{\times} \rightleftharpoons \mathrm{Li}_i^{\bullet} + \mathrm{F}'_i \tag{2.11}$$

At lower temperatures, an association regime arises, in which electrostatic association causes the mobile ionic oppositely charged carrier to be partially trapped near the immobile dopant

site. This leads to the formation of an immobile dipole. A possible association reaction is

$$V'_{\mathrm{Li}} + \mathrm{D}^{\bullet} \rightleftharpoons (V_{\mathrm{Li}}\mathrm{D}) \tag{2.12}$$

where (V_{Li}D) is the associated complex. The mass action law of Equation 2.12 reads

$$K_A = \frac{[(V_{\mathrm{Li}}\mathrm{D})]}{[\mathrm{Li}_i^{\bullet}][V'_{\mathrm{Li}}]} = \frac{N_A}{N_{\mathrm{Li}} N_D} \exp\left(\frac{\Delta_A S^{\circ}}{k_B}\right) \exp\left(-\frac{\Delta_A H^{\circ}}{k_B T}\right) \tag{2.13}$$

Here, K_A is the association equilibrium constant, and $\Delta_A S^{\circ}$ and $\Delta_A H^{\circ}$ are the standard entropy and enthalpy of association. For association caused by a cation dopant on a lithium site, N_{D} and N_{A} equal N_{Li} and $6\mathrm{N}_{\mathrm{Li}}$, respectively. For dopants on the chalcogenide site, the concentrations of available sites for positive dopants are $N_{\mathrm{D}} = {}^{4}/_{a_0^3}$ and for associates $N_{\mathrm{A}} = {}^{32}/_{a_0^3}$. Electroneutrality in $\mathrm{Li_2X}$ is described in general by

$$[V'_{\mathrm{Li}}] + [\mathrm{e}'] + \sum_k [\mathrm{A}'_k] + [\mathrm{X}''_i] = [\mathrm{Li}_i^{\bullet}] + [\mathrm{h}^{\bullet}] + \sum_k [\mathrm{D}_k^{\bullet}] + [V_{\mathrm{O}}^{\bullet\bullet}] \tag{2.14}$$

where $[\mathrm{A}'_k]$ is the concentration of the k^{th} negative dopant A'_k and $[\mathrm{D}_k^{\bullet}]$ is the concentration of the k^{th} positive dopant $D_k^{\bullet}$, neglecting higher valences. Due to the above given structural assumption for Schottky- and anti-Frenkel disorder, it is assumed that chalcogen defects have negligible concentrations. Their presence can not be ruled out but is not necessary to explain the results obtained below. For simplicity, it will be further assumed in this work that only one positive and one negative dopant are dominant; then Equation 2.14 and the entire defect calculation simplifies considerably. The majority defect pair typically changes with stoichiometry, doping content and temperature. From mass conservation, the total dopant concentration C obeys

$$\mathrm{C} = [\mathrm{D}^{\bullet}] + [(V_{\mathrm{Li}}D)]. \tag{2.15}$$

In Equation 2.15 each positive dopant (D) is either unassociated ($[\mathrm{D}^{\bullet}]$) or associated with a lithium vacancy ($[(V_{\mathrm{Li}}\mathrm{D})]$). If one considers the case of positive doping, such as LiF in $\mathrm{Li_2O}$

due to reaction 2.8, the electroneutrality condition can be approximated as

$$[V'_{\mathrm{Li}}] = [\mathrm{Li}_i^{\bullet}] + [\mathrm{F}_{\mathrm{O}}^{\bullet}] \tag{2.16}$$

In the intrinsic regime, $[\mathrm{Li}_i^{\bullet}] >> [\mathrm{F}_{\mathrm{O}}^{\bullet}]$, and the condition simplifies further to yield the typical Brouwer approximation:

$$\text{regime I:} \quad [V'_{\mathrm{Li}}] = [\mathrm{Li}_i^{\bullet}] = \sqrt{K_F} \tag{2.17}$$

At lower temperatures in regime II, the opposite relation $[\mathrm{Li}_i^{\bullet}] << [\mathrm{F}_{\mathrm{O}}^{\bullet}]$ holds, yielding

$$[V'_{\mathrm{Li}}] = [\mathrm{F}_{\mathrm{O}}^{\bullet}] = \mathrm{C} \tag{2.18}$$

In regime II the concentration of associates is negligible due to a low K_A, so for Equation (2.15) it follows that $\mathrm{C} = [\mathrm{F}_{\mathrm{O}}^{\bullet}]$, resulting in

$$\text{regime II:} \quad [V'_{\mathrm{Li}}] = \mathrm{C} \tag{2.19}$$

Approaching lower temperatures, the concentration of associates is no longer negligible, so Equation (2.15) reads $\mathrm{C} = [\mathrm{F}_{\mathrm{O}}^{\bullet}] + [(V_{\mathrm{Li}}\mathrm{F}_{\mathrm{O}})]$ and has to be used and inserting this into Equation (2.19) gives

$$[V'_{\mathrm{Li}}] = \mathrm{C} - [(V_{\mathrm{Li}}\mathrm{F}_{\mathrm{O}})] \tag{2.20}$$

Combining this expression with Equation (2.13) and considering Equation (2.19) leads to

$$[V'_{\mathrm{Li}}] = \mathrm{C} - K_{\mathrm{A}}[V'_{\mathrm{Li}}]^2 \tag{2.21}$$

The concentration of V'_{Li} can then be obtained by solving this quadratic formula. For strong association ($\mathrm{C} = [(V_{\mathrm{Li}}\mathrm{D})]$), i.e. in regime III, it holds that

$$\text{regime III:} \quad [V'_{\mathrm{Li}}] = \sqrt{C/K_A} \tag{2.22}$$

If the equilibrium constants in Equation (2.17), (2.19), and (2.22) are expressed by Equation (2.6) and (2.13) and consistency of the corresponding enthalpy and entropy of the reactions is assumed, the thermodynamic parameters follow. The resulting functions are plotted versus inverse temperature for a given set of thermodynamic parameters in Figure 2.1 (Kröger-Vink diagrams). Analogous results are obtained for predominant negative doping. The results are summarized in Table 2.1.

Table 2.1: Defect concentrations for ionic species are given for regime I to III for dominating positive ($D^\bullet$) and negative (A') doping. Note, that C refers to the sum of all positive dopants including positive background metal impurities.

	Positive-doped				Negative-doped	
	I. intrinsic	II. extrinsic	III. association		I. intrinsic	II. extrinsic
$\mathbf{[V'_{Li}]=}$	$\boldsymbol{\sqrt{K_F}}$	$\mathbf{[D^\bullet]}$	$\boldsymbol{\sqrt{[D^\bullet]/K_A}}$	$[V'_{Li}]=$	$\sqrt{K_F}$	$K_F/[A']$
$[Li_i^\bullet]=$	$\sqrt{K_F}$	$K_F/[D^\bullet]$	$K_F\sqrt{K_A/[D^\bullet]}$	$\mathbf{[Li_i^\bullet]=}$	$\boldsymbol{\sqrt{K_F}}$	$\mathbf{[A']}$
$C=$	$[D^\bullet]$	$[D^\bullet]$	$\sqrt{[D^\bullet]/K_A}$	$C=$	$[A']$	$[A']$
$[(V_{Li}D]=$	$K_A\sqrt{K_F}[D^\bullet]$	$K_A[D^\bullet]^2$	$[D^\bullet]$			

In the general case of the presence of positive (background) and negative dopants the electroneutrality equation reads

$$[V'_{Li}] = [Li_i^\bullet] + [D^\bullet] - [A'] \tag{2.23}$$

$$= [Li_i^\bullet] + C \tag{2.24}$$

with C being the effective donor concentration. Again in the intrinsic region at high temperatures, the intrinsic defect concentrations exceed the extrinsic dopant concentrations ($[F'_i] < [V'_{Li}]$), leading to

$$\text{regime I:} \quad [V'_{Li}] = [Li_i^\bullet] = \sqrt{K_F} \tag{2.25}$$

Assuming (as discussed in chapter 4) that the dissolved negative dopant concentration is

much higher than the background impurities ($[A'] \gg [D^{\bullet}]$), the following Brouwer approximation is obtained:

$$\text{regime II:} \quad [Li_i^{\bullet}] = [A'] \tag{2.26}$$

In principle association of fluorine interstitials and lithium interstitials may occur, but this effect was not observed in any of the investigated systems, perhaps because the interstitial-interstitial site spacing (a_0) is much larger than the Li-X site spacing ($\sqrt{3}/4 \cdot a_0$). As Before, a Brouwer diagram can be constructed as shown in Figure 2.1b from the Brouwer approximations summarized in Table 2.1.

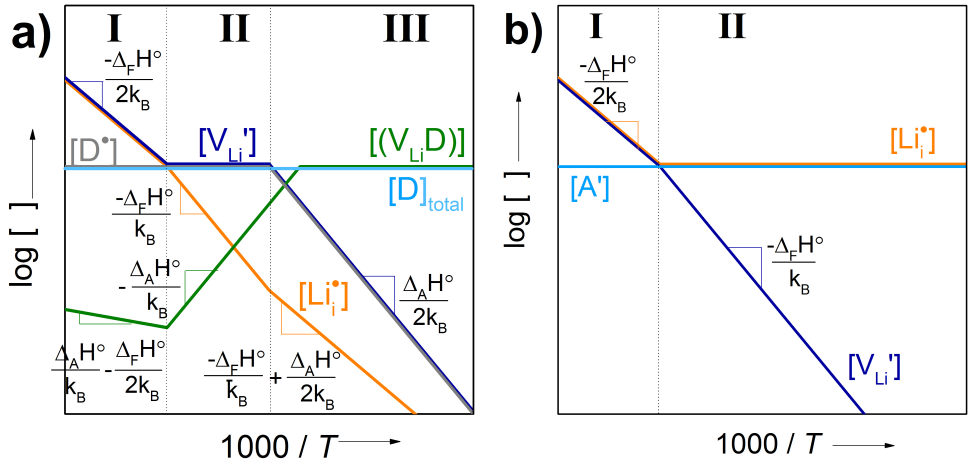

Figure 2.1: Defect concentrations as a function of inverse temperature in a) positive- and b) negative-doped Li_2X.

The dependence on doping is shown in Figure 2.2. Note that for positive-doped Li_2X, the vacancy concentration scales to the power 0.5 or 1.0 in regime III or II.

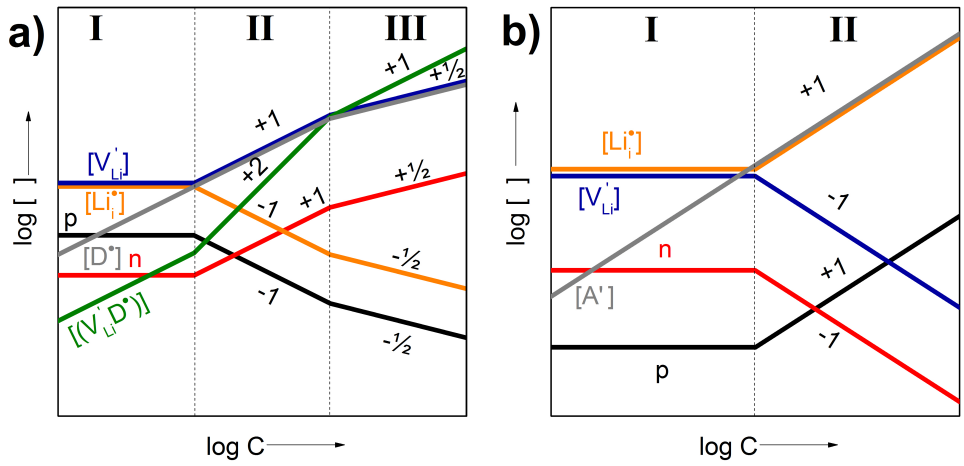

Figure 2.2: Defect concentrations in Li_2X as a function of net added dopant C for a) positive and b) negative doping. Association of interstitial ions was not observed and thus is not considered in b).

Figure 2.2 also includes schematically the minority carrier concentrations. In equilibrium with the surrounding gas phase, these defect concentrations are redox-coupled to the oxygen partial pressures by

$$Li_2O + 2V'_{Li} + 2h^{\bullet} \rightleftharpoons 2Li^{\times}_{Li} + \frac{1}{2}O_2 \qquad \text{with} \qquad K_O = \frac{\sqrt{p_{O_2}}}{[h^{\bullet}]^2[V'_{Li}]^2} \tag{2.27}$$

For predominant ionic disorder $[V'_{Li}] = [Li^{\bullet}_i]$ still holds. Chalcogen defect concentrations are neglected here. Approaching more extreme activity values, such as the stability limits of Li_2X as is the case when lithiating or delithiating a chalcogenide in a battery, such considerations are important. At intermediate temperatures, where diffusivities are high enough to reach reasonable equilibration times, solving Equation 2.27 by assuming ionic disorder with Equation 2.19 and rearranging gives

$$[h^{\bullet}] = p_{O_2}^{1/4}[C]^{-1}K_O^{-1/2} \tag{2.28}$$

Combining Equation 2.28 with Equation 2.5 results in

$$[e'] = p_{O_2}^{-1/4}[C]^{1}K_O^{1/2}K_B^{-1} \tag{2.29}$$

At higher or lower oxygen partial pressures Equation 2.19 does not hold any more. The electroneutrality equation 2.14 then simplifies under the assumption of $K_B \gg K_F$ and C=D$^\bullet$ and $K_B \gg [\mathrm{D}^\bullet]$. The Brouwer approximation than gives $\mathrm{p} = [V'_{\mathrm{Li}}]$ and $n = [\mathrm{Li}_i^\bullet]$, respectively. Combining these again with Equation 2.27 results in new functions as shown in Table 2.2, which are schematically shown in Figure 2.3.

Table 2.2: Defect concentrations for both ionic and electronic species are summarized as a function of oxygen partial pressure.

defect	n= $[\mathrm{Li}_i^\bullet]$	$[V'_{\mathrm{Li}}] = [\mathrm{D}^\bullet]$	p= $[V'_{\mathrm{Li}}]$
$[V'_{\mathrm{Li}}] =$	$p_{\mathrm{O}_2}^{1/8} K_{\mathrm{O}}^{-1/4} K_B^{-1/2} K_F^{1/2}$	$[\mathrm{D}^\bullet]$	$p_{\mathrm{O}_2}^{1/8} K_{\mathrm{O}}^{-1/4}$
$[\mathrm{Li}_i^\bullet] =$	$p_{\mathrm{O}_2}^{-1/8} K_{\mathrm{O}}^{1/4} K_B^{1/2} K_F^{1/2}$	$K_F/[\mathrm{D}^\bullet]$	$p_{\mathrm{O}_2}^{-1/8} K_{\mathrm{O}}^{1/4} K_F$
p=	$p_{\mathrm{O}_2}^{1/8} K_{\mathrm{O}}^{-1/4} K_B^{1/2} K_F^{-1/2}$	$p_{\mathrm{O}_2}^{1/4} [\mathrm{D}]^{-1} K_{\mathrm{O}}^{-1/2}$	$p_{\mathrm{O}_2}^{1/8} K_{\mathrm{O}}^{-1/4}$
n=	$p_{\mathrm{O}_2}^{-1/8} K_{\mathrm{O}}^{1/4} K_B^{1/2} K_F^{1/2}$	$p_{\mathrm{O}_2}^{-1/4} [\mathrm{D}] K_{\mathrm{O}}^{1/2} K_B$	$p_{\mathrm{O}_2}^{-1/8} K_{\mathrm{O}}^{1/4} K_B$

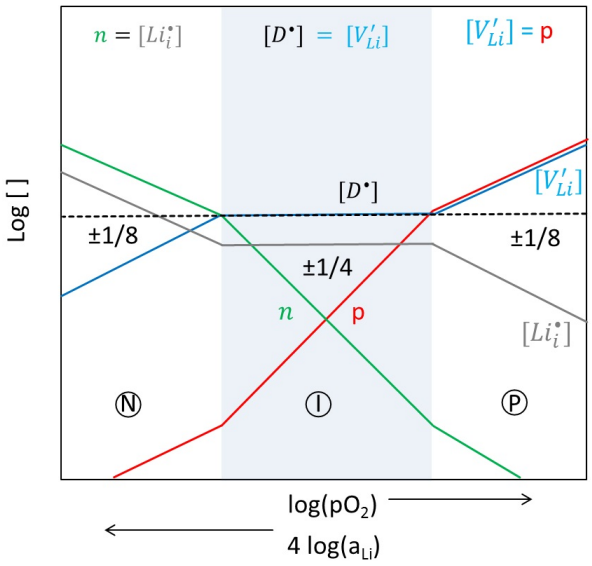

Figure 2.3: Defect concentrations in $\mathrm{Li_2O}$ as a function of lithium activity or oxygen partial pressure.

The regimes at very high and low lithium activity when chalcogen defects are the compensating defects (*i.e.*, n= $2[V_{\mathrm{O}}^{\bullet\bullet}]$ and $\mathrm{p} = 2[\mathrm{O}_i'']$) are not shown because they do not appear

in the measurements. The three regimes are typically labeled intrinsic-, n- or p-type regime, referring to the dominant charge carrier in these regimes as indicated in Figure 2.3. The posited defect model above describes the concentration relations from defect thermodynamics. In order to probe the model with conductivity measurements (Equation 2.31), the kinetics of defect migration have to be considered.

2.1.2 Defect kinetics

Assuming a typical random walk diffusion model[89,109] for dilute defects, the mobility of defect species k is expressed by

$$u_k T = \frac{r_k^2 e}{N k_B} \nu_0 \exp\left[\frac{\Delta_m S_k}{k_B}\right] \exp\left[-\frac{\Delta_m H_k}{k_B T}\right] \tag{2.30}$$

Here $\Delta_m S_k$ and $\Delta_m H_k$ are the enthalpy and entropy of migration of species k, ν_0 is the attempt frequency, r_k is the distance between neighboring sites available for the defect, and N is the number of neighboring sites,[110] which equals 6 in the antifluorite. The distance r_k equals $\frac{a_0}{2}$ for vacancies and $\frac{a_0\sqrt{2}}{2}$ for interstitials, with the unit cell dimensions a_0 given in Table 1.1. The jump attempt frequency ν_0 can be estimated to be 10^{13} Hz according to $\nu_0 = k_B \Theta_D / h$,[111,112] where h is Planck's constant and Θ_D is the Debye frequency (300 K). The conductivity σ_k of a species k with charge z_k is given by

$$\sigma_k T = z_k e [k] u_k T \tag{2.31}$$

with the mobility u, the concentration of the mobile defect $[k]$ and e as the elemental charge. The conductivity of a defect k can be described by inserting the Brouwer approximations of regime I to III given above (Equation 2.17, 2.19, 2.22) and Equation 2.30. The result is shown schematically in Figure 2.4.

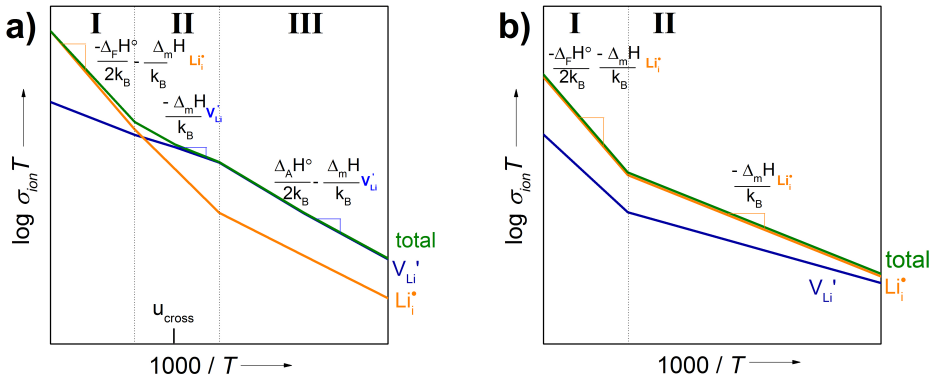

Figure 2.4: Conductivity versus inverse temperature for predominantly a) positive-doped and b) negative-doped Li_2X.

In chapter 4 the model given above will by validated by experiment.

3 Experimental methods

3.1 Bulk sample preparation

Lithium chalcogenides are hygroscopic and hydrolyze in air to form lithium hydroxide and the corresponding H_2X compound. Therefore, all preparation and characterization was done in an inert atmosphere: glovebox (oxygen and water below 1ppm), vacuum ($p < 10^{-5}$ mbar) or flowing argon during measurements (99.999% Westfalen AG). Lithium oxide (99.99%, American Elements) and lithium sulfide (99.95%, Sigma-Aldrich) were used as received with no detectable impurities by XRD. Lithium telluride (99.9%, Cerac) showed $LiTe_3$ impurities that reacted to Li_2Te during sintering with excess lithium as described below. Doped samples were achieved by adding (all from Sigma-Aldrich) LiF (99.99%), LiCl (99.99%), LiBr (99.999%), LiI (99.9%), LiH (95%), $LiOH{\cdot}H_2O$ (99.9%), MgS or Li_3N (99.5%) to the chalcogenides. MgS was synthesized from $MgBr_2$ at 700 °C under flowing H_2S (5 mol% in Argon).

Nanocrystalline Li_2X was synthesized by adding elemental sulfur (99.999%, Sigma-Aldrich), selenium (99.99%, Sigma-Aldrich), or tellurium (99.99%, Sigma-Aldrich) to a 1 M solution of lithium-triethylborohydride in tetrahydrofuran (THF) (Sigma-Aldrich). A yellow (Li_2S), orange (Li_2SE), or white (Li_2Te) powder precipitated upon adding hexane. The precipitate was filtered off, washed with THF, dried, and sintered at 400 °C for 2 h in the glovebox on a hot plate.[7]

All samples were uniaxially cold-pressed in a glovebox (15-60 kN, 10 mm diameter, 1-5 mm thick) and subsequently sintered in alumina boats sealed in quartz ampules under argon or vacuum (10^{-5} mbar) at 900 °C (Li_2O, Li_2S) or 750 °C (Li_2Se, Li_2Te), ramp rates are typically 5 °C and dwell times 2 to 5 h, resulting in densities of 75 - 85% by measuring volume

and mass. To avoid additional contamination, all pellets were covered by excess powder of the same material or mixture during sintering. A porosity correction was omitted. Grain sizes for sintered Li_2X were in the range of 30 - 100 μm obtained from scanning electron microscopy images (Zeiss Merlin) after carbon coating (Leica EM ACE200) as shown in Figure 3.1.

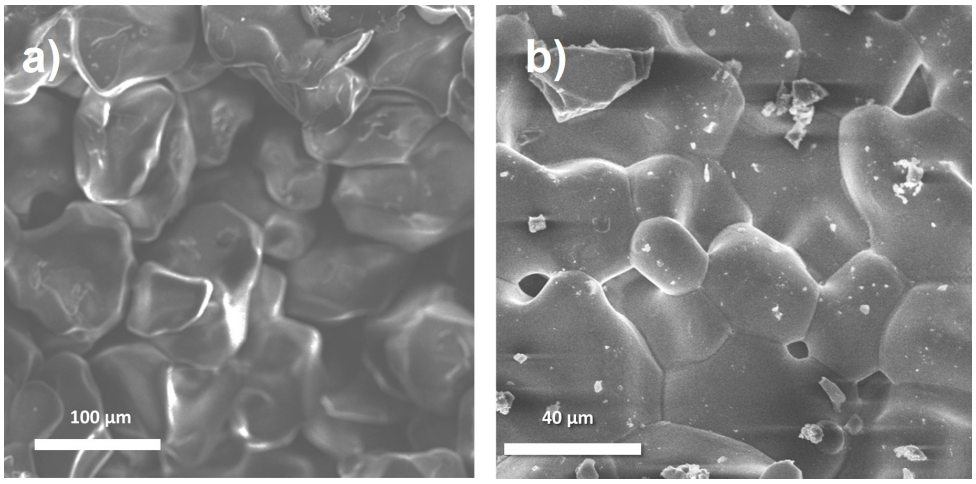

Figure 3.1: SEM images acquired from sintered pellets of a) Li_2O and b) Li_2S after carbon coating.

Sintering of Li_2X above 900 °C was avoided as it led to evaporation and reactivity with the quartz ampule, which ultimately led to pellet cracking and ampule leakage. Both Li_2Se and Li_2Te showed a tendency to lose lithium upon annealing in vacuum, traces of elemental tellurium and selenium were visible by XRD after sintering. To avoid this loss and ensure full conversion of any $LiTe_3$ to Li_2Te, small amounts of (excess) metallic lithium were added to the ampule to increase the partial pressure of lithium during annealing. This excess lithium reacted completely with the sample, alumina boats, and quartz ampules, and was not detected in the pellets after sintering visibly or by XRD.

Single crystals were grown from Li_2S (99.9%, Alfa Aesar) and Li_2O powders (99.99%, American Elements) that were pressed into pellets. For lithium sulfide, the powder was placed in two nested sealed tantalum crucibles and heated to 1400 °C, dwelled for 5 h, cooled to 1000 °C at 5 °C/h and then cooled to 25 °C at 3 °C/min. Li_2O single crystals were grown by the floating zone technique.[38] Single crystals had dimensions of 4 mm diameter

and 2 mm thickness for Li_2S and 8 mm diameter and 12 mm length (rod) for Li_2O.

3.2 Thin film preparation

This section briefly describes the sputter and MBE setup used to grow Li_2X thin films. Prior to film growth, the substrates (10 *x* 10 *x* 0.5 mm, Crystec GmbH, Germany) were cleaned in acetone in an ultrasonic bath and transferred into the glovebox.

3.2.1 Sputter deposition

During sputtering energetic ions are created by a plasma, accelerated to a target by an electric field, and blast the target material into a plume that then deposits material on a substrate to produce a thin film. Two types of targets were used in this work: a ceramic Li_2X target or reactive sputtering by co-deposition of the elements, form either elemental targets (Li, S) or the gas phase (O). The ceramic Li_2X targets were prepared as shown in Figure 3.2

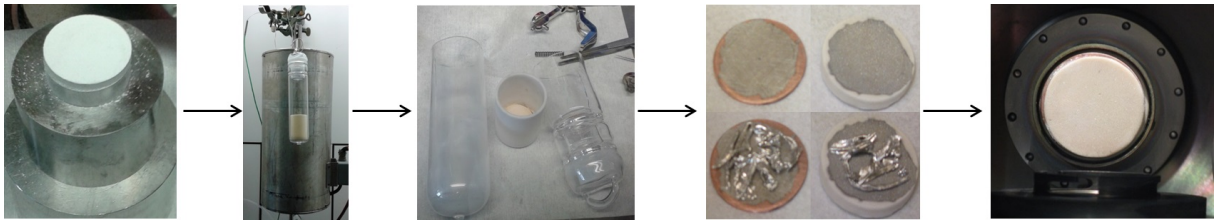

Figure 3.2: Ceramic target preparation: Li_2S powder was cold pressed in a glovebox, sintered in an ampule under inert atmosphere, polished in a glovebox afterwards, bonded to a copper backing plate, and transferred to the sputter chamber without exposure to air.

Pressed pellets were sintered under inert atmosphere in ampules at 900 °C. These targets (33 mm diameter, 4 to 5 mm thickness, 80% density) were bonded to copper backing plates by first pre-sputtering the backside of the pellets with platinum, then melting indium over the platinum using a hot plate, pressing the copper plate against the molten indium, and allowing the assembly to cool. Elemental targets were made by melting metallic lithium (99.9%, Alfa Aesar) or sulfur (99.995%, Sigma-Aldrich) in a pellet-shaped die with the

backing plate at the bottom. A slight reaction of the copper with lithium was observed. For sulfur targets, an aluminum backing plate was used to avoid reaction with the backing plate forming copper sulfide. After solidification the target was polished. All targets were transfered to the growth chamber without exposure to air using a custom transfer tool.

Argon was used as a plasma gas when thin films were deposited from Li_2O or Li_2S targets. Mixtures of argon and O_2 (90%/10%) were used with the lithium target in reactive sputtering to produce Li_2O. The deposition pressure was 0.01 mbar adjusted with mass flow controllers at a total throughput of 100 sccm. Li_2S films were grown by sputtering simultaneously from sulfur and lithium targets.

The sputter system was custom-built at the Max Planck Institute for Solid State Research. The spherical growth chamber had several attachments as shown schematically in Figure 3.3: a sample manipulator stage (one-axis), a load lock system, and two sputter sources.

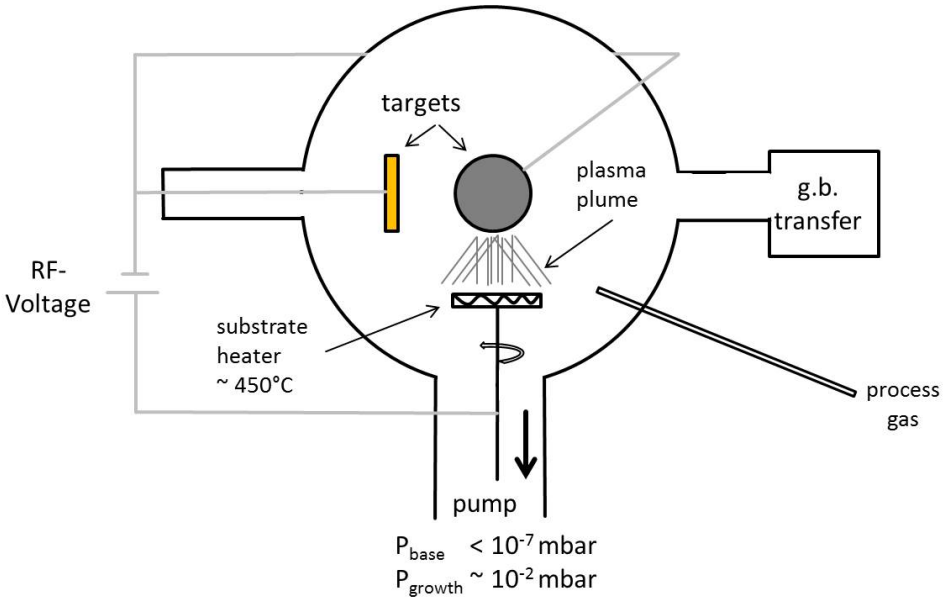

Figure 3.3: Apparatus for sputter deposition of Li_2S and Li_2O.

The manipulator provided vertical translation and was equipped with a resistive heater ($T_{max} = 450$ °C) and a motorized rotating sample stage. The resistive heater was controlled by a thermocouple. The heater was calibrated with a pyrometer (Heitronics KT19.99) that was attached to the growth chamber and pointed to a $SrTiO_3$ (100) substrate as a reference

(emissivity 0.913). The temperature profile followed the calibration shown in Figure 3.4, such that all temperatures given in the following refer to the surface temperature of the substrate prior to deposition, assuming similar thermal absorption of all used substrates.

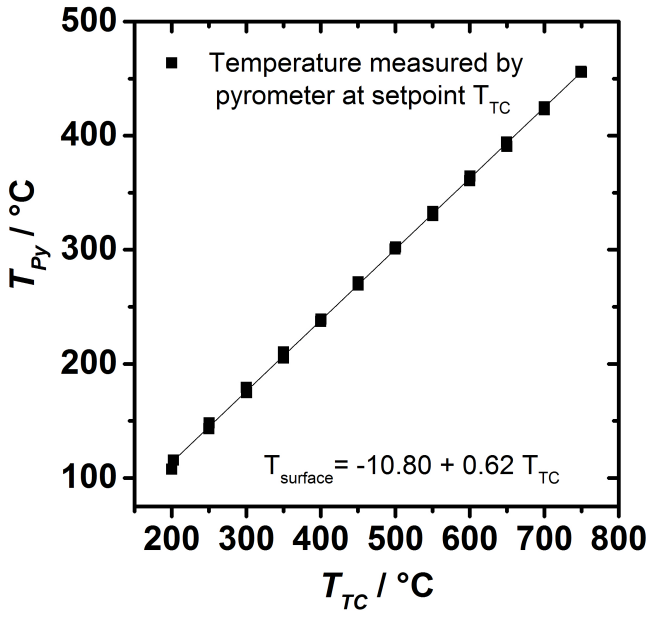

Figure 3.4: Calibration of the resistive heater controlled by a thermocouple (T_{TC}) with a pyrometer (T_{Py}) in the sputter system.

The load lock chamber was used for the transfer of substrates from the glovebox to the growth chamber. A manipulator with a valve can be connected to both the glovebox and the load lock chamber guaranteeing sample transfer without exposure to air. The load lock was pumped by a scroll pump and connected to a high purity (99.9999%, Westfalen AG) argon bottle. The sputter sources (MAK 1.3 inch diameter) are water-cooled, equipped with shutters to provide cleaning of the surface prior to each deposition, and are attached each to a RFX-300 generator (Meivac) with automatic matching unit. A turbopump with scroll-type backing pump provided a high vacuum atmosphere (base pressure below 10^{-6} mbar). High purity argon and oxygen (99.999%, Westfalen AG) process gases were connected from gas cylinders to the main chamber by leak-tested metal tubing. Mass flow controllers provided a constant flow of process gas. For higher pressure sputter deposition (0.1 to 10 mbar), the

turbopump was throttled with a gate valve. The sample stage was mounted in an off-axis geometry with a distance of approximately 4 cm relative to the targets. Reactive sputtering caused the lithium metal target to partially corrode, forming Li_2O at the surface when oxygen is introduced. Sputtering for prolonged times in argon cleaned the surface again, as shown in Figure 3.5. Between growth of different materials, such cleaning was necessary to obtain pure films.

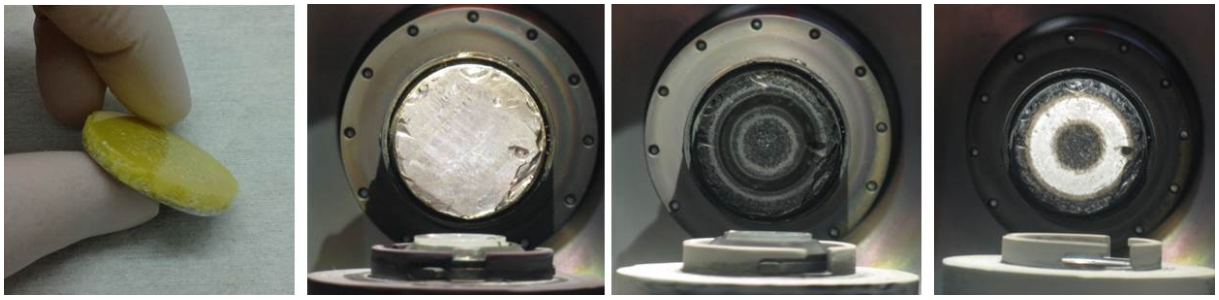

Figure 3.5: From left to right: Fresh sulfur target; lithium target before sputtering, after sputtering in a mixed argon/oxygen atmosphere, and after subsequent sputter-cleaning in pure argon.

3.2.2 Molecular Beam Epitaxy

Molecular beam epitaxy uses thermal evaporation in an ultrahigh vacuum to achieve high purity and precise control during thin film preparation. In comparison to sputter deposition which includes high energy plasmas, here the kinetic energy of the atomic flux is orders of magnitude lower, leading to less intermixing and reactivity with the substrate during film growth. When growing Li_2O, Li_2S and Li_2Se (compare to Figure 1.2) only the binary compositions are stable under the used conditions.

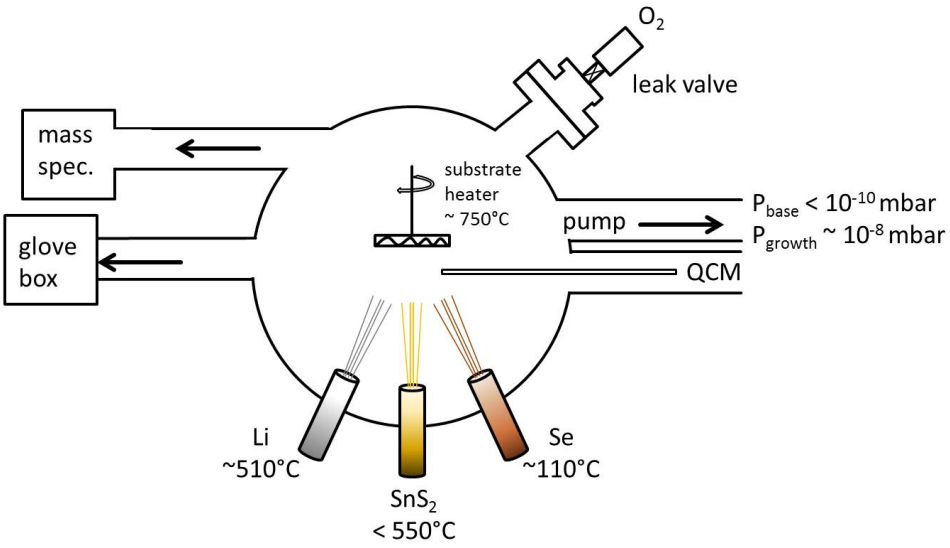

Figure 3.6: Schematic of the molecular beam epitaxy system used for deposition of Li_2O, Li_2S and Li_2Se films.

Off-stoichiometric films, as often observed for alloys or ternary compounds, were never observed. Note that excess of any one precursor (lithium (99.9%, Alfa Aesar), sulfur (99.995%, Sigma-Aldrich), SnS (99.999%, Reliable Chemicals), selenium (99.99%, Sigma Aldrich), or oxygen (99.999%, Westfalen AG)) is expected to sublime or re-evaporate at the elevated temperatures used, such that only the desired stoichiometric compositions remains.

The MBE includes a load lock system connected to a glovebox. The growth chamber is equipped with five water-cooled effusion cells, each pointing to a substrate placed upside down in the center of the chamber. The stage is heated with resistive elements controlled by a thermocouple in the back of the substrate (operating up to 825 °C) and is motorized to allow both rotation and vertical movement. Each effusion cell is equipped with a shutter to switch the evaporation fluxes that reach the sample. Pumping is achieved by a turbo-pump backed with a scroll pump (load lock) as well as ion, turbo, and cryopumps (growth chamber). Background and beam pressures are measured by multiple pressure gauges at different positions in the main chamber. The effusion cells are loaded through the load lock, which allows a continuous operation of the growth chamber without venting for refilling and allows the use of air sensitive materials such as lithium metal to be evaporated. Prior to the

growth, the substrates were held at the growth temperature for 30 min to ensure thermal equilibrium. The sources were heated from their standby temperature (200 °C for lithium and SnS_2) to the selected growth temperature (typically between 450 and 550 °C) resulting in beam pressures of 10^{-7} mbar as measured with a beam pressure gauge at the position of the substrate, resulting in growth rates of about 2 nm/minute.

Growth rates were further monitored by a quartz crystal balance system. The substrate is heated by a resistive element (operating up to 800 °C) controlled by a thermocouple in the back of the substrate. A nozzle is used to feed in oxygen gas for the growth of Li_2O by an automated valve controlling the oxygen supply to $5{\cdot}10^{-6}$ mbar. Higher pressures were avoided due to the risk of oxidizing the resistive heaters of the effusion cells. Background pressures are below 10^{-10} mbar and it was observed that prolonged lithium evaporation presumably reacted with surface water in the chamber and thereby helped to decrease the background pressure.

3.2.3 Handling of air sensitive thin films

Due to severe humidity sensitivity of Li_2X thin films, leak tested chambers were used for sample transfer and characterization or electrochemical measurements. Both the sputter chamber and MBE setup allowed for safe sample transfer directly to a glovebox. However, leaks were initially observed that were solved by always following a standard routine: the sputter transfer tool had to be evacuated below 10^{-2} mbar at least three times and refilled with bottled argon (99.9999% purity) to provide a save transfer. The MBE load lock was pumped by a turbopump backed by a membrane pump. Before venting and sample transfer to the glovebox, the membrane pump had to be disconnected by an additional valve due to back-diffusion of water vapor from ambient atmosphere. Additionally, a connection from the glovebox argon supply had to be permanently attached, because the 99.999% purity argon previously used caused thin film degradation.

Transfer of the thin films between gloveboxes was done by using quartz chambers (empty desiccators) with greased fittings that were evacuated below 10^{-1} mbar prior to the transfer with a membrane pump.

Even in the glovebox, thin films decomposed to the hydroxide after several weeks. This hydrolysis was further slowed by storage in evacuated desiccators inside the glovebox. Adding a drying agent such as silica worsened the storage life and led to detectable water concentrations (several ppm) measured by the glovebox water sensor. Storage for weeks (or months) in the load lock of the MBE at pressures below 10^{-6} mbar without decomposition was also possible. In conclusion, storage under vacuum is best for avoiding film hydrolysis.

Leak testing of the impedance measurement cells was also frequently done. In particular, BNC connectors were a common source of leakage in such cells. Leakage was lowest when BNC connectors with ceramic isolation were welded to the stainless steel flanges of the cells.

3.3 Sample characterization

3.3.1 Bulk samples

The phase purity of pellets was verified by X-ray diffractometry (Panalytical Empyrean, Cu K_α) on samples sealed under argon using a polycarbonate dome sample holder (Anton Paar). Phase-pure patterns were obtained before and after impedance measurements for all four Li_2X materials. A Zeiss Merlin scanning electron microscopy (SEM) setup with GEMINI column was used to estimate grain sizes. Impurities in powders and sintered pellets were measured by inductively coupled plasma optical emission spectroscopy (Spectro Ciros CCD) as shown in Table 3.1.

3.3.2 Thin films

Scanning Electron Microscopy setup

The SEM mentioned above was also used for investigation of surface morphologies of thin films. A focused ion beam (FIB-SEM) was available (Zeiss Crossbeam) for the fabrication of cross-sections in order to study porosity and thickness of the air sensitive films. Figure 3.7 shows an in-house build transfer tool that allowed for safe transfer of thin films between glovebox and the SEM chamber.

Table 3.1: Impurities observed in ICP-OES measurements for vendor purity Li_2O (99.99%) and Li_2S (99.95%) and sintered Li_2S.

Element	Li_2O ppm	Li_2S ppm	Li_2S sintered ppm
Al	10	15	75
B	20	15	20
Ba	0.5	0.5	5
Ca	20	40	45
Fe	10	5	10
K	85	85	70
Na	100	150	250
Si	200	10	35
Zn	< 5	10	20

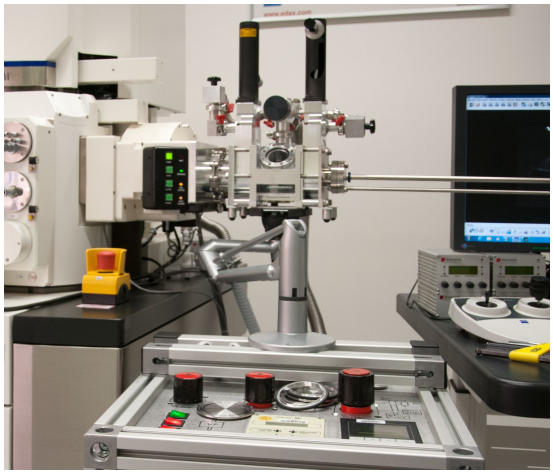

Figure 3.7: An in-house build transfer tool allowed for an air-free transfer of Li_2X thin films and pellets to a carbon coater and the SEM from a glovebox.

The aluminum chamber is pumped by a turbo pump backed by a scroll pump below pressures of 10^{-4} mbar. Transfer to a carbon coater (Leica EM ACE200) prior to SEM was possible with the tool without exposure to air as well.

X-Ray diffraction setup

For Li_2X thin films an in-house-built x-ray setup (Dr. D. Fischer, Department Prof. J. Mannhart) was used that operates in ultra-high vacuum. A theta/theta D8-Advance powder diffractometer (Bruker AXS) was used at 10^{-7} mbar vacuum. The temperature during measurements could be adjusted by a resistive heater in vacuum that allowed transfer without exposure to air from a glovebox to the XRD chamber as well. The residual gas was recorded by a mass spectrometer. Initially, XRD on thin films was measured under argon using a polycarbonate-domed transfer tool. The dome leak-rate was tested with bulk Li_2S powder, where LiOH peaks were detected after approximately 12 h. Thin films were measured within 1 h but visual changes due to unavoidable leaks were observed after XRD and the films were discarded after XRD and the XRD setup under high vacuum was preferred. For powder samples the domed transfer holder was stable for approximately 24h with no detectable impurities as shown in Figure 3.8. Powders or pellets measured by XRD were not used for further analysis or measurements to avoid LiOH contamination.

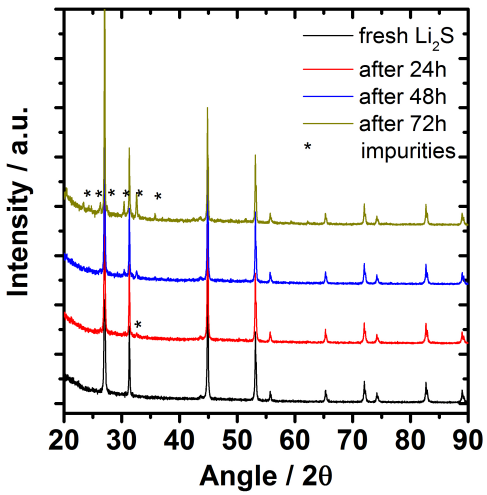

Figure 3.8: XRD measurements of Li_2X in a polycarbonate domed tool.

Raman spectroscopy

Raman spectroscopy was available as an attachment to the XRD setup of thin films: a microscope laser Raman spectrometer with confocal geometry (473 nm, 20 mW) was used.

3.4 Electrochemical measurements

3.4.1 Impedance spectroscopy

Method

In impedance spectroscopy the current response of a small applied alternating voltage is measured for a broad range of frequencies which enables the analysis of transport- and dielectric properties of a sample.[113–115] The obtained spectra are typically interpreted with the aid of electrical circuit models based on serial and parallel resistors (R) and capacitors (C). A common circuit for an ideal sample-electrode assembly is a single RC element with the bulk resistance

$$R = \frac{L}{\sigma A} \tag{3.1}$$

and the geometrical capacitance according to the dielectric properties of the sample

$$C = \frac{A\epsilon_0\epsilon_r}{L} \tag{3.2}$$

where L and A are the pellet thickness and electrode area, and ϵ_0 the permittivity of free space, and σ the specific conductivity and ϵ_r the dielectric constant of the sample. The time constant τ for such an RC element follows as

$$\tau = RC \tag{3.3}$$

In real measurements, the assumption of ideal uniformly active electrodes typically is not valid; instead a dispersion in the time constants is seen that can be modeled by constant

phase elements (CPE).[114] The impedance of a CPE is given by

$$\hat{Z}(\omega) = \frac{1}{(j\omega)^n Q} \tag{3.4}$$

where Q and n are the magnitude and exponent of a constant phase element (CPE), which can account for non-ideal ($n \neq 1$) behavior such as porosity and surface heterogeneities but can reflect pure capacitive ($n = 1$) behavior, too. The effective capacitance of a CPE follows as

$$C = Q^{(1/n)} R^{(1/n-1)} \tag{3.5}$$

In the Nyquist representation of impedance data used here (real vs. imaginary part of impedance) RC elements appear as semicircles. For more complex samples, several different processes may appear with different time constants and their resistances and capacitances can be obtained by fitting. For the sintered pellets used in this work, bulk, grain boundary, or electrode processes are expected that have different capacitances on the order of 10^{-12}, 10^{-9}, and 10^{-6} F or more, due to the different geometries involved.

The conductivity analyzed below in chapter 4 was calculated using Equation 3.1 and the dielectric constant ϵ_r was calculated with Equation 3.2 and **??**.

Experimental

Pellets and single crystals were polished with 1000-grit SiC and diamond lapping paper to a mirror like finish after annealing. Samples were contacted for transport measurements by 200 - 400 nm thick ruthenium electrodes (99.95%, Lesker) by DC sputtering (Emitech K575X) at room temperature in a glovebox. For electron-blocking measurements, three-layer electron-blocking electrodes were prepared by uniaxially co-pressing LiI (Sigma-Aldrich, 99.9%), a mixture of LiI and $Li_4Ti_5O_{12}$ (Sigma-Aldrich, 99.9%), and $Li_4Ti_5O_{12}$ powders. Compacts were then sandwiched between two of these three-layer electrodes to form the overall cell $Li_4Ti_5O_{12}$ | LiI | Li_2O | LiI | $Li_4Ti_5O_{12}$ which showed reproducible results up to 200 °C. For thin film electron blocking measurements, "Lithium Ion Conductive Glass Ce-

ramic" (LICGC, Ohara company) was contacted with evaporated lithium from lithium foil (99.9%, Alfa Aesar) in a glovebox and placed on top of the thin films.

All samples were spring-loaded between platinum or carbon foil (for pellets) or wire (for thin film) contacts and installed in a quartz chamber inside a tube furnace, and heated under 50 sccm (approximately 10 cm/s) argon flow. A special quartz sample holder for thin films was used in the quartz ampule. Impedance spectroscopy measurements (Novocontrol Alpha-A) were performed at frequencies ranging from 10^6 to 10^{-3} Hz and at 25 °C steps from 25 to 900 °C. Typically, multiple thermal cycles were performed to verify reproducibility. Before each measurement a dwell time of 1 h was used at each temperature to ensure thermal equilibration. The temperature during measurement was measured by a separate thermocouple next to the sample. The software ZView (Scribner Associates, USA) was used for fitting the data.

3.4.2 DC measurements

Methods

Different cell arrangements were explored for DC measurements, e.g. for Li_2O:

$$\mathrm{Li, LiAl|Li_2O|Li_2Sb, Li_3Sb} \tag{3.6}$$

$$\mathrm{Pt}(p_{\mathrm{O}_{2,1}})\mathrm{|Li_2O|Pt}(p_{\mathrm{O}_{2,2}}) \tag{3.7}$$

$$\mathrm{Pt|Li_2O|Pt} \tag{3.8}$$

$$\ominus \quad \mathrm{LiAl|Li_2O|Ru} \quad \oplus \tag{3.9}$$

Cells 3.6 to 3.9 are used for the investigation of different charge carriers in e.g. Li_2O.[113] Cells 3.6 and 3.7 are galvanic cells with Li_2O used as a mixed conducting electrolyte separating two electrodes of different lithium activity. Focusing on a gradient in lithium potentials in cell 3.6 it follows that for a lithium potential difference a neutral lithium flux occurs as a result of predominant ionic disorder but non-negligible electronic conductivity

$$j_{Li} \propto -\sigma_{Li}^{\delta} \frac{\partial \mu_{Li}}{\partial x} \tag{3.10}$$

with $\sigma_{Li}^{\delta} = \sigma_{eon}\sigma_{eon}/\sigma$. At steady state it follows

$$j_{Li} \propto -\int_{\mu_{Li}}^{\mu_{Li}+\Delta\mu_{Li}} \sigma_{Li}^{\delta} d\mu_{Li} \tag{3.11}$$

At steady state, as a consequence of internal short circuiting currents, the open cell voltage or electromotive force E (EMF) further obeys the Nernst equation

$$V_{Nernst} = \frac{RT}{2F}\int t_{ion} d\mu_{Li} = \frac{RT}{2F} < t_{ion} > ln\left(\frac{a_{Li,1}}{a_{Li,2}}\right) \tag{3.12}$$

For an ideal ionic conductor, the full Nernst voltage is expected at open circuit. According to Equation 3.13,

$$V =< t_{ion} > V_{Nernst} \tag{3.13}$$

a mixed conductor shows a value that is lower by the average transference number $< t_{ion} >$. Therefore, the measurement of the EMF allows for a deconvolution of electronic and ionic conductivity.

Cell 3.8 is used for polarization measurements. If a constant current is applied to the cell, a voltage drop across Li_2O occurs, according to the dc resistance $\frac{I}{U} = \frac{1}{R_{dc}} = \frac{1}{R_{eon}}\frac{1}{R_{ion}}$, which depends on the partial electronic and ionic resistances. When using lithium blocking platinum electrodes, a stoichiometric polarization occurs when a current flows and a chemical potential gradient is established. When steady state is reached, the electrical potential gradient is able to compensate for the chemical potential gradient. The transient behavior is due to the chemical diffusion coefficient (D^{δ}) in the sample and its thickness (L) according to

$$D^{\delta} = \frac{L^2}{\pi^2 \tau_{\delta}} \tag{3.14}$$

An alternative procedure is the Hebb Wagner measurement[116] that makes use of the cell 3.9. Here, the electronic conductivity of predominating ionic conductors can be measured as a function of lithium activity. It comprises the measurement of a steady state current in

an asymmetric cell that is selectively polarized by an applied voltage E according to

$$\ln a_{Li} = \frac{EF}{4RT} \tag{3.15}$$

with F as Faraday's constant, R as the universal gas constant, T as temperature, and a_{Li} as activity of lithium. When the potential is applied, lithium flows according to the polarization of the cell towards the lithium electrode. Lithium is depleted on the blocking electrode first and consequently the flow of lithium ultimately vanishes because the counter electrode cannot supply additional lithium. Under steady state a chemical potential gradient of lithium balances the applied potential and the current is carried only by the unblocked electronic species. Independent migration of the defects, ideally blocking electrodes, potentials below the decomposition voltage and small deviations from non-stoichiometry and of electronic carriers to apply an ideal dilute situation are assumed. The current density J in such a situation can be described by[116,117]

$$J = \left\{ \sigma^{\circ}_{\ominus} \left[1 - \exp\left(-\frac{EF}{RT} \right) \right] + \sigma^{\circ}_{\oplus} \left[\exp\left(\frac{EF}{RT} \right) - 1 \right] \right\} \cdot \left(\frac{RT}{FL} \right). \tag{3.16}$$

The total current than depends on the ratio of hole ($\sigma^{\circ}_{\oplus}$) and electron conduction ($\sigma^{\circ}_{\ominus}$) and the electrode distance L. In the current work, both Li_2O and Li_2S single crystals have been investigated using a LiAl alloy with a defined lithium activity as negative electrode.

Experimental

Li_2Sb and Li_3Sb were synthesized separately by annealing stoichiometric amounts of lithium (99.9%, Alfa Aesar) and antimony (unknown purity and source) on tantalum boats in sealed quartz ampules at 550 °C under argon. XRD confirmed that phase-pure Li_2Sb and Li_3Sb were obtained. The two powders were then mixed manually using a mortar and pestle. EMF cells were assembled by manually pressing Al,LiAl (Elsa Metal) and either Li or Li_2Sb,Li_3Sb electrodes against a Li_2X pellet. The cells were then measured (Keithley 6514 electrometer) in a quartz chamber as described for the impedance measurements. Noble metals (Ni, Ti, Au, Pt, Ru), sputtered to Li_2X pellets in the glovebox, were used as ion-blocking electrodes.

Measurements were done in argon or mixed nitrogen/oxygen atmosphere (cell 3.8) for Li_2O.

Hebb Wagner measurements on pellets were done using LiAl (other electrodes with defined lithium activity are possible, too) and ruthenium electrodes. Long equilibration times were necessary due to sluggish kinetics and the sample showed degradation after several weeks in the quartz chamber from reactivity with accumulated water impurities from the argon (99.999% purity). A microelectrode setup was used to overcome sluggish kinetics and improve purity: A stainless steel chamber with heating stage was pumped below 10^{-5} mbar with a turbopump backed by a scroll-pump. Single crystal Li_2O and Li_2S was measured with a LiAl pellet negative electrode and Ru (sputtered) or carbon (evaporated) as positive electrode (175 μm diameter). Electrical noise from the heater during polarization was decreased by shielding the heater from the sample with a grounded aluminum foil. Temperatures between 200 and 450 °C were used. Below 200 °C, equilibration was not achieved due to sluggish kinetics, and above, lithium surface diffusion led to short circuits.

Transfer of the sample from the glovebox to the chamber was done in air. Several pumping and purging cycles (with argon) were used before the final evacuation and before the sample was heated initially. Excess lithium was placed next to the sample in the chamber to reduce the water background pressure during measurements.

4 Results for Bulk Samples

The above constructed defect model is compared to results from AC and DC measurements on doped and undoped bulk samples over a wide temperature range and lithium activity. The extracted thermodynamic and kinetic parameters are discussed and compared to previous literature at the end of the chapter. The findings provide a foundation for evaluating the thin film results (chapter 5) and applications (chapter 6).

4.1 Electromotive force

The EMF of electrochemical cells employing Li_2X as a mixed conducting electrolyte is shown in Figure 4.1. Below the melting point of Li (181°C), the cell Li | Li_2X | Al, LiAl was used. At higher temperatures, the cell Al, Li_xAl | Li_2X | Li_2Sb, Li_3Sb was employed, but temperatures above 225 °C were required to equilibrate to a stable EMF,[118,119] perhaps due to inadequate mixing or equilibration of the Li_2Sb, Li_3Sb before cell assembly. Above 450 °C reliable EMF values were not obtained. Instead, the measured voltage decreased to 0 V. This short-circuiting of the cell was caused by a grey surface coverage on the sides of the pellets, consisting most likely of metallic components (Li, Al, LiAl) due to fast surface diffusion. After polishing off the surface layer and applying new electrodes, the EMF values shown in Figure 4.1 were restored.

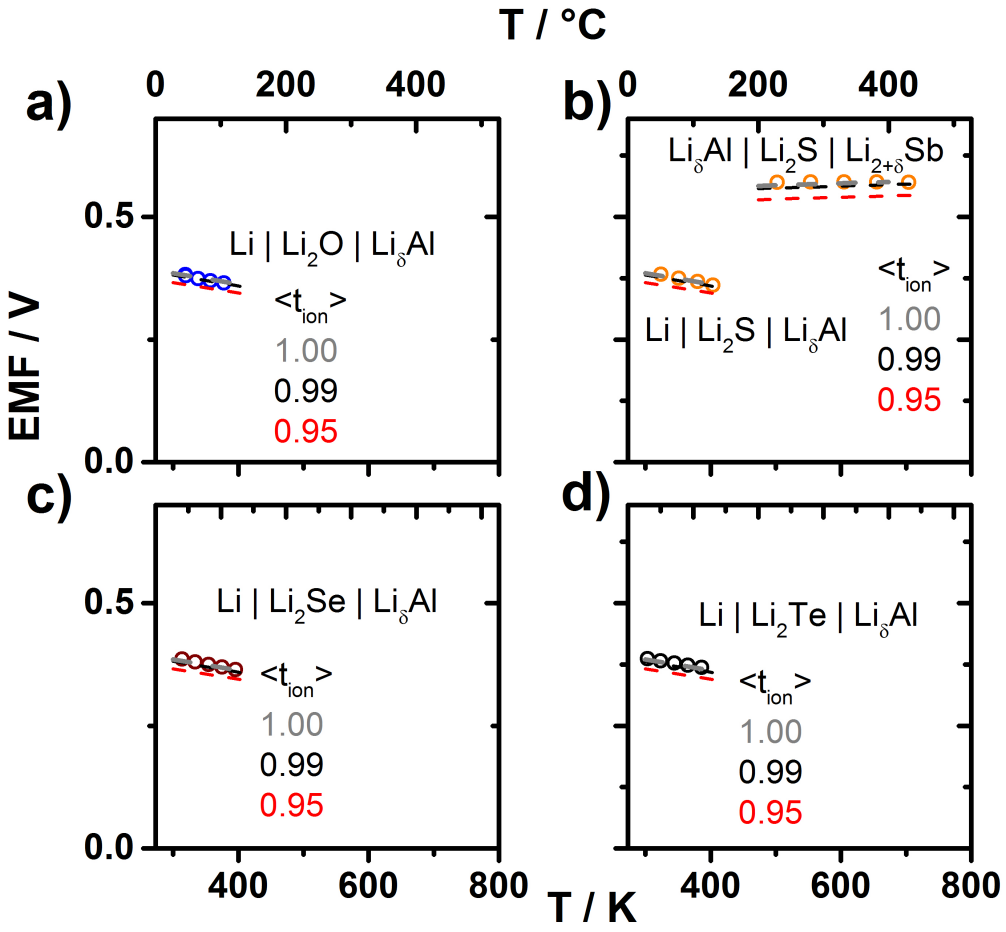

Figure 4.1: Electromotive force measurements on Li_2O, Li_2S, Li_2Se, and Li_2Te.

For all four materials, the ionic transference number is larger than 0.99 comparing the assumed t_{ion} to the data in Figure 4.1. Hence, σ_{eon} is at least two orders of magnitude lower than σ_{ion} in the given temperature and lithium activity region in nominally undoped Li_2X.

The carrier concentrations of ionic and electronic species vary with lithium activity as shown in Figure 2.3 and therefore the precise value of t_{ion} will also vary. The lithium activity in the Li_2X pellets likely did not equilibrate fully with the electrodes owing to sluggish kinetics. The result $t_{ion} \geq 0.99$ applies for the activity of Li set by the pellet sintering process. For Li_2O sintering was performed with approximately 10 ppm oxygen in the ampule, corresponding to a voltage of approximately 2.2 V. These internal gradients in the measured EMF were only compatible with predominant ionic conductivity throughout. The observed blocking behavior at low frequencies in the impedance measurements shown below pro-

vided further evidence for predominant ionic conductivity over the encompassed lithium activity. Therefore, fixing the activities in Li_2X in the impedance measurements was not necessary.

4.2 Impedance

Typical impedance spectra acquired from sintered pellets of Li_2X with ion blocking ruthenium electrodes near 50 °C are shown in Figure 4.2. All four materials show a high frequency semicircle, while Li_2S and Li_2Se also show a shoulder at lower frequencies.

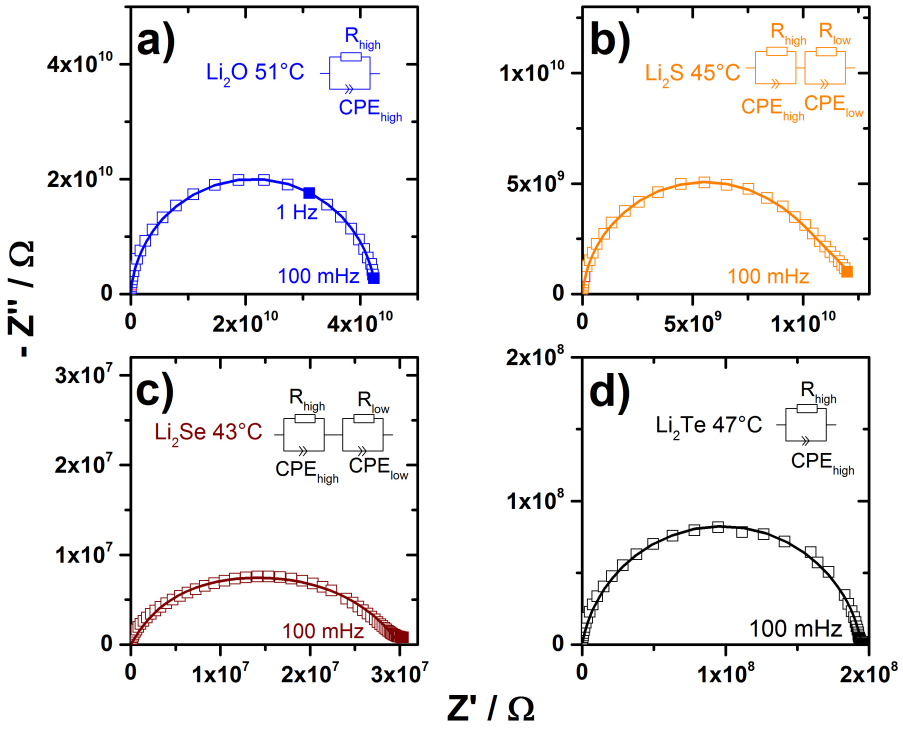

Figure 4.2: Impedance spectra (points) acquired from Li_2X near 50°C with ruthenium electrodes and a fit (line) by the given equivalent circuits.

The data were fit by the equivalent circuits shown as insets. Measurements from pellets of different thicknesses showed that only the resistance of the high frequency semicircle scales linearly with thickness, as shown in Figure 4.3.

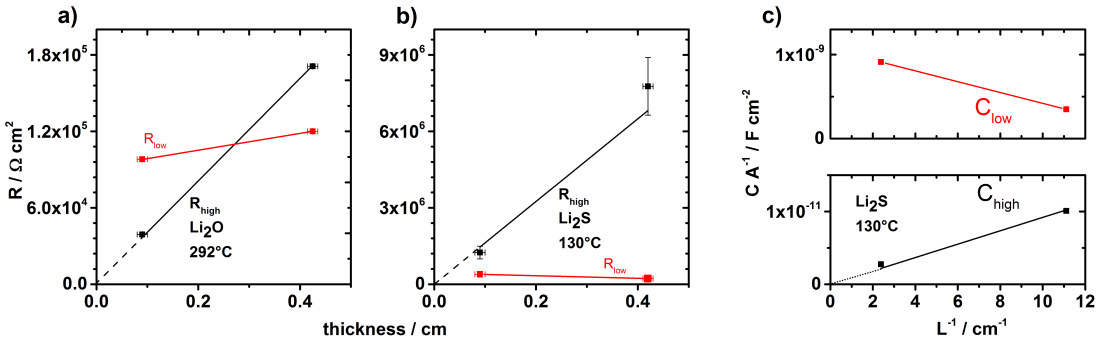

Figure 4.3: a, b) Resistances and c) capacitances extracted from the impedance measurements.

The high frequency semicircle is thus interpreted as corresponding to bulk ion transport. The capacitance of the high frequency arc took typical values (10^{-11} F) for the dielectric capacitance of such samples. Using equations 3.2 and 3.5, the dielectric constant ϵ_R of each material was calculated (Figure 4.4a). The obtained values fall in the range 10 - 30, which is typical for ionic solids.[120] The lower frequency arcs do not scale with thickness. Additionally, the capacitance extracted were around 10^{-9} F or higher, consistent with electrode processes that are not further investigated here.

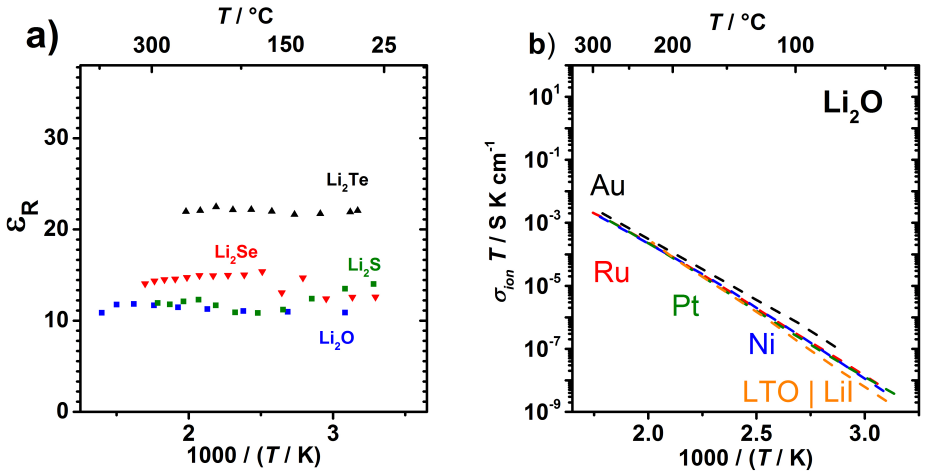

Figure 4.4: a) Dielectric constants as a function of temperature. b) Comparison of the ionic conductivity values obtained for Li_2O using different electrode materials.

Going from Li_2O to Li_2Te, the dielectric constant increases, consistent with the fact that

larger ions tend to be more polarizable.[110] Figure 4.4b compares different electrode materials used for electrical measurements of Li_2O: the measured ionic conductivity is seen to be insensitive to the choice of electrodes, as expected. However, the high temperature stability was found to be best for ruthenium electrodes, while the other metals seemed to more readily form ternary Li-M-O phases, leading to visible color changes and corrosion. Electron blocking electrodes were also tried, i.e., Li_2X was sandwiched between layers of LiI and $Li_4Ti_5O_{12}$,$Li_7Ti_5O_{12}$. The high frequency semicircle measured with these electrodes was unchanged, in agreement with dominating ionic conductivity.

At elevated temperatures, a third semicircle appears due to the blocking of lithium ions at the ruthenium electrode as shown in Figure 4.5.

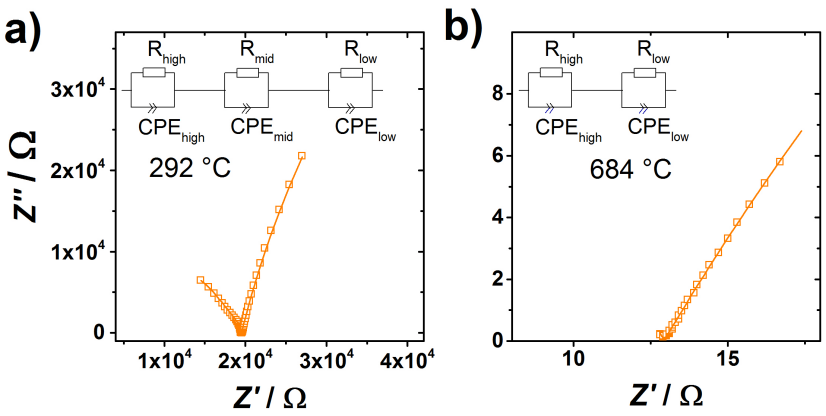

Figure 4.5: Impedance spectra of Li_2S at elevated temperatures showing a) a third semicircle due to polarization at the electrodes and b) a merged high frequency response.

The mid frequency feature shrinks in relative magnitude and becomes negligible (Figure 4.5b). This behavior is further evidence that the mid-frequency shoulder corresponds to a non-bulk process, since the activation energy of this feature is different from the bulk conduction. At the highest temperatures, the bulk behavior is only visible as an intercept to the real axis in the spectra. This intercept includes inductive effects from the cabling of the measurement setup, which was corrected for by subtracting point-wise the impedance of a short-circuited cell (Figure 4.6).

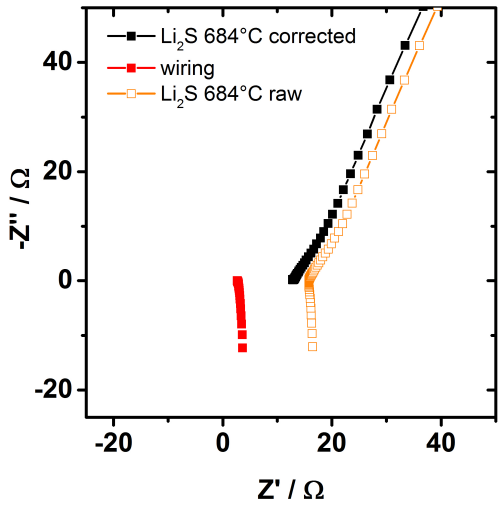

Figure 4.6: Point-wise correction of impedance data at high temperatures.

For LiF-doped Li_2S and single crystal measurements, annealing at elevated temperatures was necessary to obtain stable values (Figure 4.7).

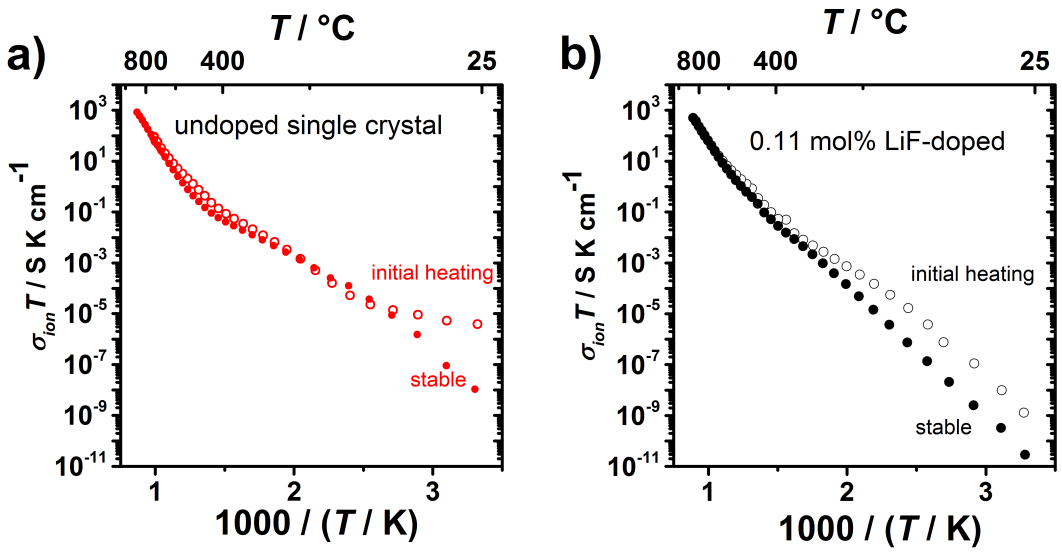

Figure 4.7: Behavior observed during first heating of a) an undoped Li_2S single crystal and b) LiF-doped polycrystalline Li_2S.

The initial enhancement seen for the single crystal in Figure 4.7a was observed both in freshly prepared Li_2O and Li_2S single crystals and Li_2S nanocrystalline specimens. For

PbF_2 an enhanced conductivity was also observed upon grinding the surface,[121] and it was speculated that the enhancement was due to frozen-in defect concentrations, line defects, or amorphous material formed on the surface from grinding. One can speculate that a similar mechanism applies to Li_2X, but this point has not been verified. For LiF-doped polycrystalline Li_2S the initial enhancement persists to somewhat higher temperature (Figure 4.7b), and heating under flowing argon was necessary to achieve stable values, for reasons that are still unknown.

Upon multiple thermal cycles during impedance measurements of Li_2S single crystals, an additional semicircle appeared in the impedance spectra at intermediate frequencies, indicating that low frequency features depend at least partially on the thermal history of the sample but not on porosity and current constriction effects as shown in Figure 4.8.

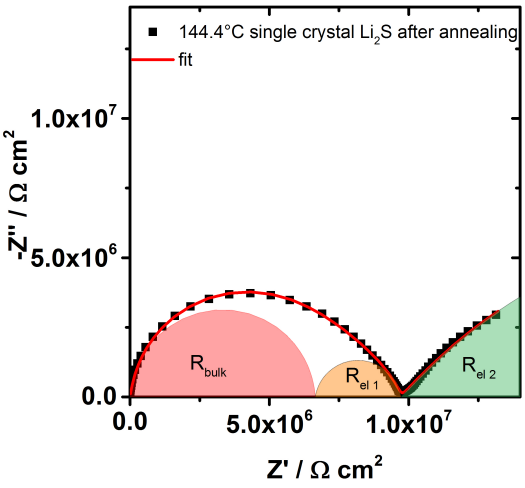

Figure 4.8: Impedance data of annealed, single crystal Li_2S showing a mid-frequency shoulder.

No sign of blocking grain boundaries was observed in any of the investigated bulk samples.

4.3 Temperature dependence of bulk conductivity

Following the defect model presented in chapter 2, the conductivity is evaluated in terms of temperature and doping dependence in the following. Arrhenius diagrams of polycrystalline

Li_2O, Li_2Se, Li_2Te, and a Li_2S single crystal are plotted in Figure 4.9. These specimens are not intentionally doped but contain small amounts of impurities from the synthesis as discussed below.

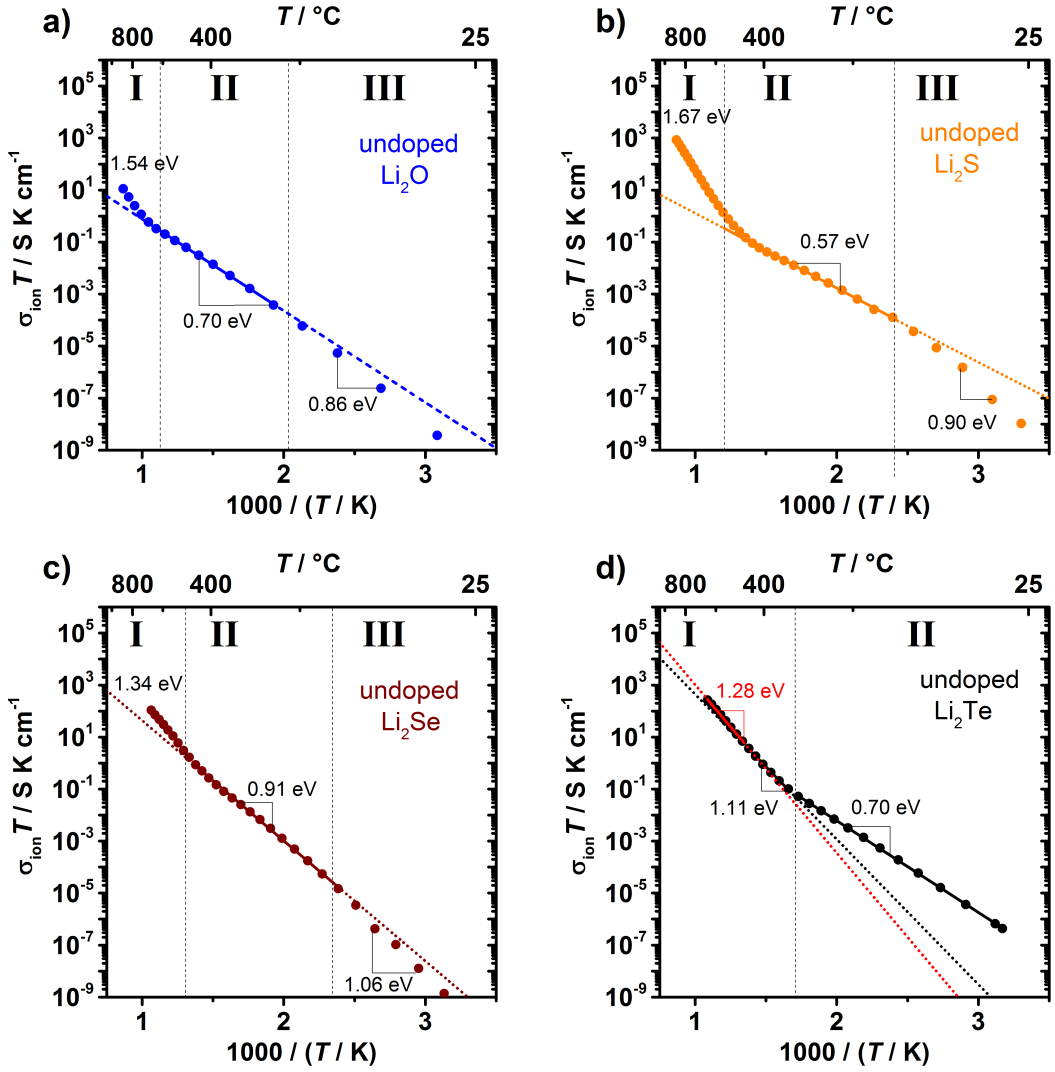

Figure 4.9: Conductivity versus inverse temperature of nominally undoped a) Li_2O, b) Li_2S, c) Li_2Se, and d) Li_2Te. Lines are linear fits to subsets of the data; dotted lines are extrapolations.

Several regimes appear (I to III), and the data in each regime are fit by lines, yielding activation energies as indicated. For Li_2O, Li_2S, and Li_2Se, three regimes are assigned, that correspond to intrinsic (regime I), extrinsic (II) and association (III) behavior. For Li_2Te association was absent in the investigated temperature range; instead the three observed

activation energies were assigned to two defect regimes as discussed below.

According to chapter 2, at high temperatures (regime I) the concentration of cation defects is determined by the Frenkel equilibrium constant (Equation 2.17). In the extrinsic regime II, the concentration of mobile defects is set by doping (Equation 2.19) and at low temperatures (region III), the mobile defect concentration depends on the extent of association between impurities and the mobile defects.

A comparison between literature values and conductivities found in this work for polycrystalline undoped Li_2O is shown in Figure 4.10a, while a comparison between polycrystalline and single crystal Li_2S together with the literature is given in Figure 4.10b.

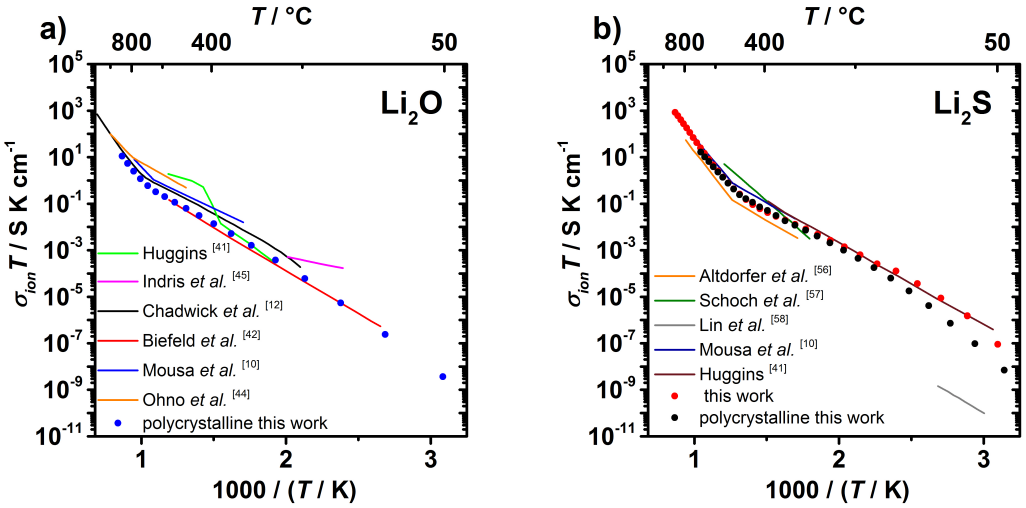

Figure 4.10: Ionic Conductivity of a) polycrystalline Li_2O and b) Li_2S single crystal (red) and polycrystalline specimen (black), compared to available literature values.

The comparison between poly- and single crystalline Li_2S further confirms the interpretation of the impedance spectra: if grain boundary contributions from blocking interfaces were present, the data would not match so well. The variations at low temperatures are due to different association energetics due to different dopants.

The ionic conductivity of the sulfide in the current work shows good agreement with the more limited datasets reported by Mousa *et al.*[10] and Huggins[41] while the agreement with Altorfer *et al.*, Schoch *et al.* and Lin *et al.*[56–58] is less good but not far off. Association was mentioned for Li_2O in previous works without providing a model or clear interpretation,

while it was not reported for Li_2S.

4.4 Doping effects on bulk conductivity

Polycrystalline Li_2X samples were doped with various concentrations of foreign ions including halides, Mg^{2+}, OH^-, N^{3-} to help identify the mobile defect.

Lithium oxide

Upon doping Li_2O with LiF (Figure 4.11), an increase in conductivity is observed.

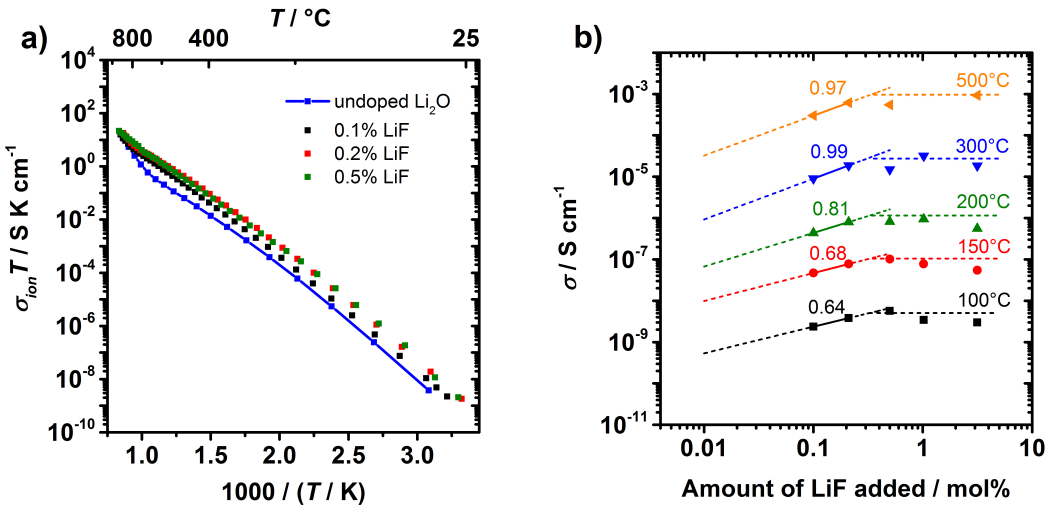

Figure 4.11: Conductivity versus inverse temperature of lithium oxide doped with LiF: a) A stepwise increase on $[F_O^\bullet]$ leads to an increase in the conductivity. Conductivity isotherms scale with added dopant as shown in b).

These data indicate lithium vacancies are the majority charge carriers according to $[V'_{Li}] = [F_O^\bullet]$. The conductivity is double logarithmically plotted as a function of added dopant in Figure 4.11b. The isotherms show two regimes. At low impurity concentrations, the scaling is approximately $1/2$ while at higher temperatures the scaling approaches 1.0. This behavior shows good agreement with the dependence predicted in Figure 2.2a. When the added fluoride amount exceeds 0.3 mol%, the isotherms plateau, suggesting that the solubility limit was reached.

Vacancy transport is favored by doping on the cation site, e.g. by MgO, according to

$$MgO + 2Li_{Li}^{\times} \leftrightharpoons Li_2O + Mg_{Li}^{\bullet} + V_{Li}' \tag{4.1}$$

A high doping content leads in the limit to $[Mg_{Li}^{\bullet}] = [V_{Li}']$ as shown in Figure 4.12. Doping with higher valent anions such as Li_3N according to

$$Li_3N + O_O^{\times} \leftrightharpoons Li_2O + N_O' + Li_i^{\bullet} \tag{4.2}$$

should increase $[Li_i^{\bullet}]$ and decrease $[V_{Li}']$ but this doping reaction did not affect the overall conductivity. Most likely the solubility limit for nitrogen on an oxygen site is lower than the impurity content due to higher coulombic repulsion and unfavorable ionic radius. Doping with LiOH

$$LiOH + Li_{Li}^{\times} + O_O^{\times} \leftrightharpoons Li_2O + OH_O^{\bullet} + V_{Li}' \tag{4.3}$$

resulted in the same effect as doping with LiF, indicating that the hydroxide species (1.37 $\AA$) substitutes for oxygen (1.40 $\AA$) and increases $[V_{Li}']$; in the limit $[OH_O^{\bullet}] = [V_{Li}']$. The solubility limits for these three dopants are tentatively below 0.1% for LiOH and MgO, while they appeared smaller for Li_3N.

Doping with LiH and Fe_3O_4 led to a different behavior. The hydride anion should favor the interstitial position and increase the interstitial lithium concentration and decrease vacancy transport (in the limit $[H_i'] = [Li_i^{\bullet}]$). Iron is expected to substitute on a lithium site due to a similar ionic radius and cause lithium vacancy transport ($n[V_{Li}'] = [Fe_{Li}^{n\bullet}]$).

The slopes below 350 °C are not changed compared to the undoped Li_2O. This indicates vacancy transport throughout but with a decrease in conductivity, which is expected for LiH if $[H_i'] < [D]$ but inconsistent with the assumed opposing doping reaction for Fe_3O_4. At intermediate temperatures even a different slope is obtained.

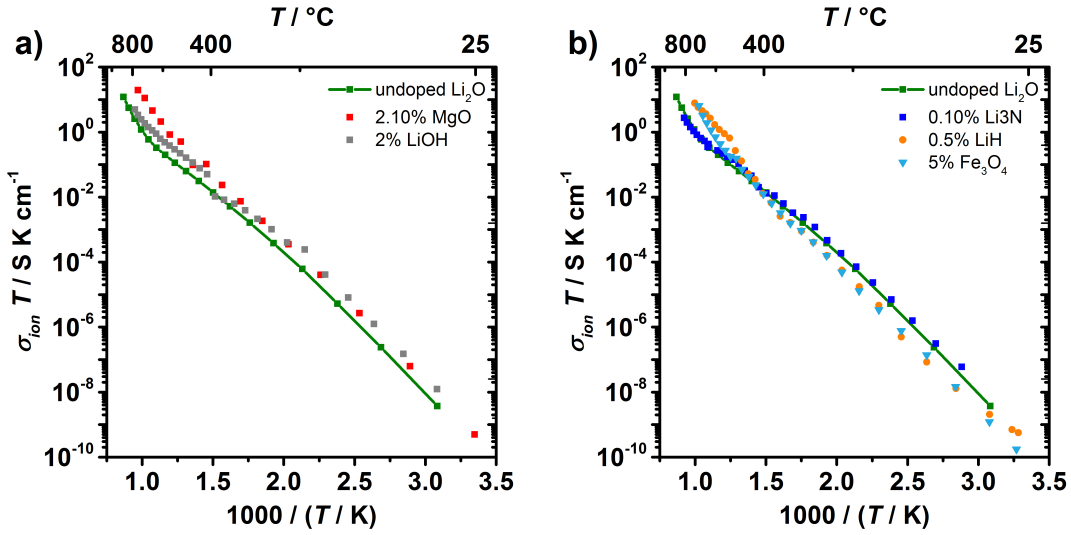

Figure 4.12: Conductivity as a function of inverse temperature for Li_2O doped by the indicated concentrations of foreign ions for a) vacancy dominated transport and b) negligible doping effects.

The high temperature behavior could be due to a temperature dependent change in solubility limit. Reactivity could cause the formation of antifluorite Li_5FeO_4.[122] Porosity and thermodynamic instability of LiH at the sintering conditions can further influence the observed data. The solubility limits are expected to be below 0.1 mol% for H_i', $Fe_{Li}^{\bullet}$ and $N_O^{\bullet}$. Due to the uncertainties discussed for LiH and iron doping, the data is considered preliminary and was not used in the quantitative analysis below.

The following $\sigma_{ion}(T)$ equations are obtained by fitting the data.

For undoped Li_2O:

$$\text{regime I:} \quad \sigma_{ion}T = 10^{5.01}\exp\left(-0.86\frac{\text{eV}}{k_BT}\right)\frac{\text{SK}}{\text{cm}} \tag{4.4}$$

$$\text{regime II:} \quad \sigma_{ion}T = 10^{3.41}\exp\left(-0.70\frac{\text{eV}}{k_BT}\right)\frac{\text{SK}}{\text{cm}} \tag{4.5}$$

$$\text{regime III:} \quad \sigma_{ion}T = 10^{7.75}\exp\left(-1.54\frac{\text{eV}}{k_BT}\right)\frac{\text{SK}}{\text{cm}} \tag{4.6}$$

For 0.1 mol% LiF the conductivities are described by the fits

$$\text{regime} \quad \text{III}: \qquad \sigma_{ion}T = 10^{5.41}\exp\left(-0.87\frac{\text{eV}}{k_B T}\right)\frac{\text{SK}}{\text{cm}} \tag{4.7}$$

$$\text{regime} \quad \text{II}: \qquad \sigma_{ion}T = 10^{4.11}\exp\left(-0.73\frac{\text{eV}}{k_B T}\right)\frac{\text{SK}}{\text{cm}} \tag{4.8}$$

The same approach results for 0.2 mol% LiF doped Li_2O in

$$\text{regime} \quad \text{III}: \qquad \sigma_{ion}T = 10^{5.77}\exp\left(-0.86\frac{\text{eV}}{k_B T}\right)\frac{\text{SK}}{\text{cm}} \tag{4.9}$$

$$\text{regime} \quad \text{II}: \qquad \sigma_{ion}T = 10^{4.09}\exp\left(-0.68\frac{\text{eV}}{k_B T}\right)\frac{\text{SK}}{\text{cm}} \tag{4.10}$$

These expressions are used below for further evaluations. Note that uncertainties introduced by the fits are neglected because they are much smaller than the uncertainty in the doping concentrations.

Lithium sulfide

A study of different dopants in Li_2S is presented in Figure 4.13. Considering first LiCl doping, the conductivity below 600 °C increases monotonically with increasing LiCl content. At higher temperatures the conductivity is essentially independent of doping, consistent with an extrinsic-to-intrinsic transition. It is expected, that sulfide ions (1.84 $\AA$) are substituted by chloride ions (1.81 $\AA$)

$$\text{LiCl} + \text{S}_\text{S}^\times + \text{Li}_\text{Li}^\times \leftrightharpoons \text{Li}_2\text{S} + \text{Cl}_\text{S}^\bullet + V'_\text{Li} \tag{4.11}$$

leading to the formation of lithium vacancies. Hence, lithium vacancies are the dominant mobile ionic defect in the extrinsic regime, scaling with conductivity as shown in 4.13b. The measured conductivity isotherms scale at certain temperatures with the power 1/2 or 1.0 dependencies ($^{d\log\sigma}/_{d\log[D]}$) in regime III (low temperature) or II (high temperature), respectively. The experimentally observed slopes from the LiCl-doped samples agree with the model predictions presented above.

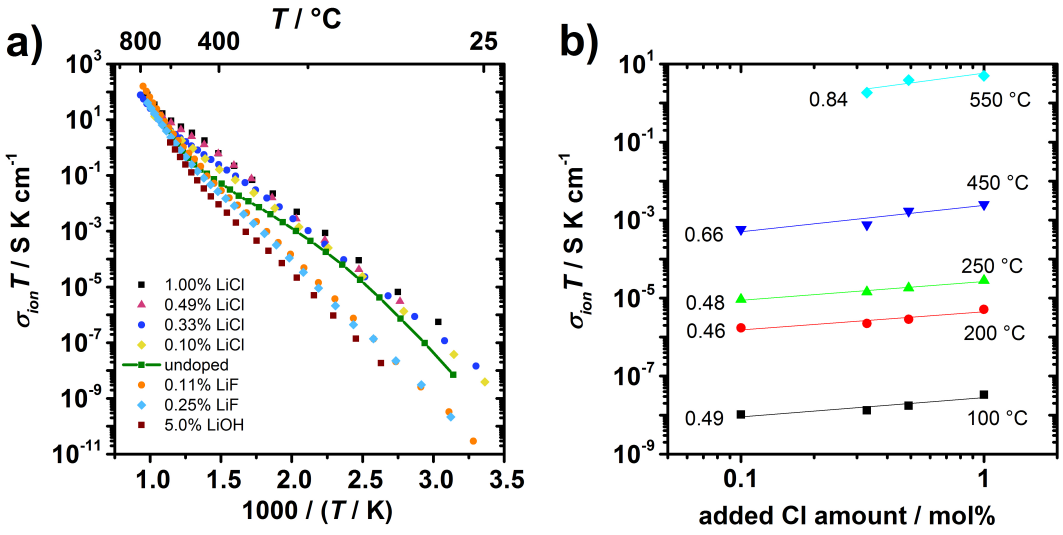

Figure 4.13: Ionic conductivity of doped Li_2S as a function of a) temperature and b) added LiCl amount.

Furthermore, both for the positively doped case and the nominally undoped sample three regimes are seen, indicating that a small positive metal dopant concentration (compare Table 1.1) is additionally present in the Li_2S sample labeled undoped. Based on ICP-OES measurements of sintered Li_2S pellets a background doping level of 0.003 mol% is estimated by combining Fe and Zn impurities, as shown in Table 3.1, since both have suitable ionic radii for substitution.

Upon adding 0.11 mol% LiF to the undoped Li_2S (Figure 4.13a), the ionic conductivity (measured after allowing the material to stabilize as shown in Figure 4.7) decreases at temperatures below 450 °C relative to the vacancy dominated transport observed in Figure 4.14b. A plausible doping reaction is that the fluoride ion (1.33 $\AA$) is added to the typically large interstitial site in antifluorites

$$\mathrm{LiF} + 2V_i^{\times} \leftrightharpoons \mathrm{Li}_i^{\bullet} + \mathrm{F}_i' \tag{4.12}$$

leading in the limit to ($[\mathrm{F}_i'] = [\mathrm{Li}_i^{\bullet}]$). In this scenario each added fluorine is charge-balanced by the formation of a lithium interstitial. The background doping would be overcompensated and a switch to interstitial dominated transport would appear. This could explain

the large difference observed in activation energies between LiCl- and LiF-doped Li_2S. Additionally, a third regime is absent for LiF doping, indicating that association of interstitials is negligible in this temperature range.

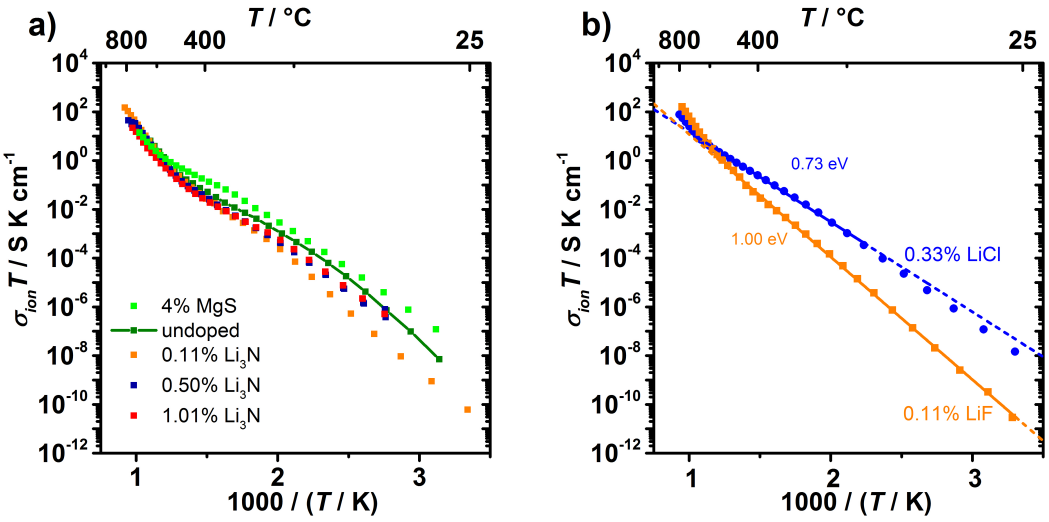

Figure 4.14: Conductivity as a function of temperature of lithium sulfide doped with a) MgS and Li_3N. A change in mobile species from lithium vacancies to interstitials in Li_2S is shown in b).

This is reasonable in light of the larger binding distances between interstitial sites than between lithium and positive dopant sites. When the LiF doping amount is increased from 0.11 to 0.25 mol%, no further change in ionic conductivity is observed. The solubility limit is thus expected to be between 0.003 mol% (the estimated background positive doping level) and 0.11 mol%. This interpretation can be checked by LiOH-doping. The hydroxide ion (1.37 *Å*) should also be added on the interstitial site, since it exhibits a similar ionic radius as the fluoride ion (1.33 *Å*). Indeed, after doping with 5 mol% $LiOH{\cdot}H_2O$, the extrinsic conductivity shows an identical activation energy (1.00 eV) as for the LiF-doped samples (also 1.00 eV). However, the $LiOH{\cdot}H_2O$-doped conductivity is a factor of four lower, consistent with a lower solubility limit of hydroxide ions compared to fluoride ions. Thus most of the added $LiOH{\cdot}H_2O$ likely remains undissolved. The undissolved $LiOH{\cdot}H_2O$ is expected to react and decompose to Li_2O during sintering.

Doping with Li_3N or MgS in several concentrations was also explored as shown in Figure

4.14. For such doping the following effects can be presumed

$$\mathrm{MgS} + 2\mathrm{Li}_{\mathrm{Li}}^{\times} \leftrightharpoons \mathrm{Li_2S} + \mathrm{Mg}_{\mathrm{Li}}^{\bullet} + V_{\mathrm{Li}}^{\prime} \tag{4.13}$$

$$\mathrm{Li_3N} + \mathrm{S}_{\mathrm{S}}^{\times} + V_i^{\times} \leftrightharpoons \mathrm{Li_2S} + \mathrm{Li}_i^{\bullet} + \mathrm{N}_{\mathrm{S}}^{\prime} \tag{4.14}$$

Indeed, for MgS doping (Mg^{2+} 0.57 $\AA$) the conductivity increases with little change in activation energy, consistent with $[\mathrm{Mg}_{\mathrm{Li}}^{\bullet}] = [V_{\mathrm{Li}}^{\prime}]$ with a solubility limit most likely below 0.5 mol%. In contrast, adding nitrogen in various amounts consistently led to a lower ionic conductivity. It is expected that it was added to the interstitial site (1.46 $\AA$), but substitution of sulfur may equally happen. Three temperature regimes are still present for Li_3N-doped Li_2S, which suggests a very low solubility limit for nitrogen, most likely due to the larger ionic radius or valence of N^{3-} compared to F^- and OH^-. In the analysis that follows, only the LiCl- and LiF-doped samples are considered.

The fits according to regime I to III for undoped polycrystalline Li_2S are

$$\text{regime I}: \quad \sigma_{ion}T = 10^{7.37}\exp\left(-0.97\frac{\mathrm{eV}}{k_BT}\right)\frac{\mathrm{SK}}{\mathrm{cm}} \tag{4.15}$$

$$\text{regime II}: \quad \sigma_{ion}T = 10^{3.53}\exp\left(-0.64\frac{\mathrm{eV}}{k_BT}\right)\frac{\mathrm{SK}}{\mathrm{cm}} \tag{4.16}$$

$$\text{regime III}: \quad \sigma_{ion}T = 10^{8.46}\exp\left(-1.38\frac{\mathrm{eV}}{k_BT}\right)\frac{\mathrm{SK}}{\mathrm{cm}} \tag{4.17}$$

For the single crystal plotted in Figure 4.9 the fits are

$$\text{regime I}: \quad \sigma_{ion}T = 10^{7.14}\exp\left(-0.90\frac{\mathrm{eV}}{k_BT}\right)\frac{\mathrm{SK}}{\mathrm{cm}} \tag{4.18}$$

$$\text{regime II}: \quad \sigma_{ion}T = 10^{3.01}\exp\left(-0.57\frac{\mathrm{eV}}{k_BT}\right)\frac{\mathrm{SK}}{\mathrm{cm}} \tag{4.19}$$

$$\text{regime III}: \quad \sigma_{ion}T = 10^{10.20}\exp\left(-1.67\frac{\mathrm{eV}}{k_BT}\right)\frac{\mathrm{SK}}{\mathrm{cm}} \tag{4.20}$$

For doped Li_2S the conductivity follows

$$0.11\ \text{mol\% LiF} \quad \text{regime II}: \quad \sigma_{ion}T = 10^{6.04}\exp\left(-0.99\frac{\text{eV}}{k_BT}\right)\frac{\text{SK}}{\text{cm}} \tag{4.21}$$

$$\text{regime I}: \quad \sigma_{ion}T = 10^{9.34}\exp\left(-1.50\frac{\text{eV}}{k_BT}\right)\frac{\text{SK}}{\text{cm}} \tag{4.22}$$

$$0.25\ \text{mol\% LiF} \quad \text{regime II}: \quad \sigma_{ion}T = 10^{5.48}\exp\left(-1.01\frac{\text{eV}}{k_BT}\right)\frac{\text{SK}}{\text{cm}} \tag{4.23}$$

$$\text{regime I}: \quad \sigma_{ion}T = 10^{8.44}\exp\left(-1.39\frac{\text{eV}}{k_BT}\right)\frac{\text{SK}}{\text{cm}} \tag{4.24}$$

$$0.10\ \text{mol\% LiCl} \quad \text{regime III}: \quad \sigma_{ion}T = 10^{6.33}\exp\left(-0.87\frac{\text{eV}}{k_BT}\right)\frac{\text{SK}}{\text{cm}} \tag{4.25}$$

$$\text{regime II}: \quad \sigma_{ion}T = 10^{4.78}\exp\left(-0.74\frac{\text{eV}}{k_BT}\right)\frac{\text{SK}}{\text{cm}} \tag{4.26}$$

$$0.33\ \text{mol\% LiCl} \quad \text{regime III}: \quad \sigma_{ion}T = 10^{5.60}\exp\left(-0.81\frac{\text{eV}}{k_BT}\right)\frac{\text{SK}}{\text{cm}} \tag{4.27}$$

$$\text{regime II}: \quad \sigma_{ion}T = 10^{4.86}\exp\left(-0.73\frac{\text{eV}}{k_BT}\right)\frac{\text{SK}}{\text{cm}} \tag{4.28}$$

$$0.49\ \text{mol\% LiCl} \quad \text{regime III}: \quad \sigma_{ion}T = 10^{5.75}\exp\left(-0.81\frac{\text{eV}}{k_BT}\right)\frac{\text{SK}}{\text{cm}} \tag{4.29}$$

$$\text{regime II}: \quad \sigma_{ion}T = 10^{3.70}\exp\left(-0.70\frac{\text{eV}}{k_BT}\right)\frac{\text{SK}}{\text{cm}} \tag{4.30}$$

Lithium selenide

Attempts were made to dope Li_2Se with LiBr, LiF, and Li_3N. The results obtained during the initial heating sequence are compared to undoped Li_2Se in Figure 4.15. The conductivities obtained fall within one order of magnitude of undoped Li_2Se. A preliminary interpretation is based on vacancy dominated transport for undoped Li_2Se at low temperatures and interstitial transport at high temperatures, as was found for Li_2S.

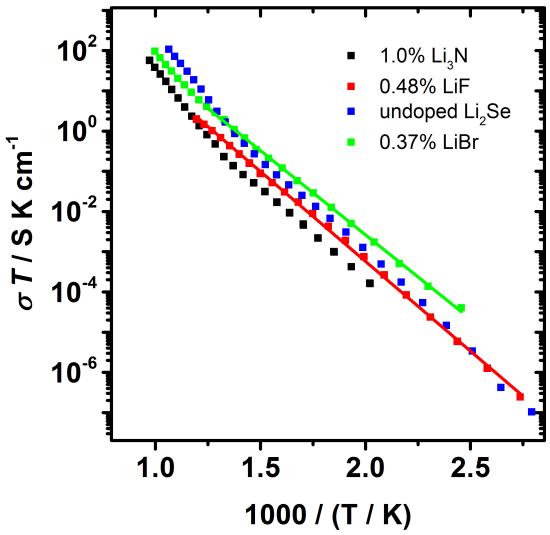

Figure 4.15: Preliminary conductivity data of doped Li_2Se.

The extracted conductivities at low temperatures follow the relations

$$0.48 \text{ mol\% LiF} \qquad \sigma_{ion}T = 10^{5.69}\exp\left(-0.89\frac{\text{eV}}{k_BT}\right)\frac{\text{SK}}{\text{cm}} \tag{4.31}$$

$$0.37 \text{ mol\% LiBr} \qquad \sigma_{ion}T = 10^{5.79}\exp\left(-0.83\frac{\text{eV}}{k_BT}\right)\frac{\text{SK}}{\text{cm}} \tag{4.32}$$

$$1.0 \text{ mol\% } Li_3N \qquad \sigma_{ion}T = 10^{5.31}\exp\left(-0.88\frac{\text{eV}}{k_BT}\right)\frac{\text{SK}}{\text{cm}} \tag{4.33}$$

Assuming the limits of bromine substitution for selenium ($[Br^{\bullet}_{Se}] = [V'_{Li}]$), the conductivity should increase. If nitrogen and fluorine favor the interstitial positions (in the limit: $3[N'''_i] = [Li^{\bullet}_i]$ and $[F'_i] = [Li^{\bullet}_i]$), then these dopants should decrease the vacancy concentration and conductivity, eventually switching to interstitial transport. Indeed this interpretation is in qualitative agreement with Figure 4.15. The given concentrations in Equation 4.31 through 4.33 are the nominal values used in the sintering, but a lower solubility limit is expected since the conductivity does not scale with such large doping concentrations. Another possibility is non-uniform mixing of the dopant. For undoped Li_2Se the relations

are

$$\text{regime} \quad \text{III}: \qquad \sigma_{ion}T = 10^{7.89}\exp\left(-1.06\frac{\text{eV}}{k_BT}\right)\frac{\text{SK}}{\text{cm}} \tag{4.34}$$

$$\text{regime} \quad \text{II}: \qquad \sigma_{ion}T = 10^{6.26}\exp\left(-0.91\frac{\text{eV}}{k_BT}\right)\frac{\text{SK}}{\text{cm}} \tag{4.35}$$

$$\text{regime} \quad \text{I}: \qquad \sigma_{ion}T = 10^{9.24}\exp\left(-1.34\frac{\text{eV}}{k_BT}\right)\frac{\text{SK}}{\text{cm}} \tag{4.36}$$

Comparing the enthalpies obtained in region II for all four samples, little scatter is observed, resulting in an average value of $\Delta_m H = 0.88 \pm 0.05 \frac{\text{eV}}{k_BT}$. The unknown absolute doping concentrations, as discussed above, lead to uncertainty in the calculation of the entropies, as will be shown below.

Lithium telluride

The ionic conductivity from nominally undoped (same as in Figure 4.9d) and 0.1 mol% LiF doped Li_2Te samples are shown in Figure 4.16a. The fit lines for undoped Li_2Te (Figure 4.9d) are

$$\text{regime} \quad \text{Ia}: \qquad \sigma_{ion}T = 10^{9.48}\exp\left(-1.28\frac{\text{eV}}{k_BT}\right)\frac{\text{SK}}{\text{cm}} \tag{4.37}$$

$$\text{regime} \quad \text{Ib}: \qquad \sigma_{ion}T = 10^{8.22}\exp\left(-1.11\frac{\text{eV}}{k_BT}\right)\frac{\text{SK}}{\text{cm}} \tag{4.38}$$

$$\text{regime} \quad \text{II}: \qquad \sigma_{ion}T = 10^{4.83}\exp\left(-0.70\frac{\text{eV}}{k_BT}\right)\frac{\text{SK}}{\text{cm}} \tag{4.39}$$

and for LiF-doped Li_2Te are

$$\text{regime} \quad \text{I}: \qquad \sigma_{ion}T = 10^{9.76}\exp\left(-1.34\frac{\text{eV}}{k_BT}\right)\frac{\text{SK}}{\text{cm}} \tag{4.40}$$

$$\text{regime} \quad \text{II}: \qquad \sigma_{ion}T = 10^{6.84}\exp\left(-0.92\frac{\text{eV}}{k_BT}\right)\frac{\text{SK}}{\text{cm}} \tag{4.41}$$

Since regime I is unchanged with doping, it can be attributed to intrinsic behavior, while regime II depends on doping and thus reflects extrinsic behavior. The change in activation energy in regime II upon LiF doping can again be explained by a change from lithium vacan-

cies to interstitials as the dominant mobile charge carrier. The two regimes in the LiF-doped sample are therefore attributed to extrinsic and intrinsic interstitial behavior, while the three regimes of undoped Li_2Te are attributed to extrinsic vacancy, intrinsic vacancy, and intrinsic interstitial transport, respectively.

To check this interpretation, switching from interstitials to vacancies should yield the same difference in activation energy in both the extrinsic and intrinsic cases. These differences are 0.23 eV (comparing regime II between the two samples) and 0.17 eV (comparing regimes Ia and Ib for the undoped sample in Figure 4.9d), showing reasonable agreement. Alternatively, the enthalpy of Frenkel cation disorder can be independently derived for these two samples as discussed below. Good agreement is observed between the obtained values (0.72 and 0.84 eV), providing further support for the interpretation here. Doping with LiI was also investigated as shown in Figure 4.16b.

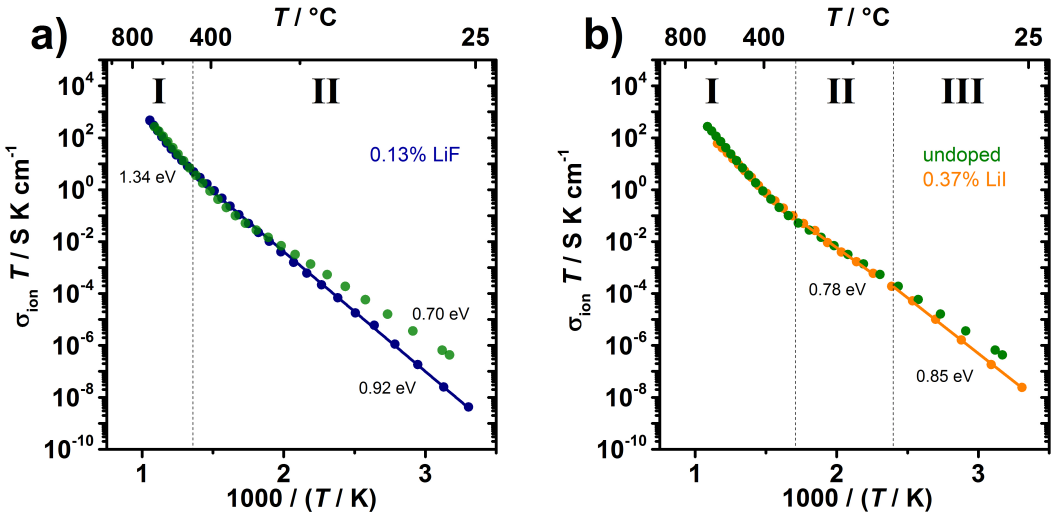

Figure 4.16: Conductivity of doped Li_2Te as a function of temperature with a) LiF doping and b) LiI doping.

Iodide ions have a similar radius as telluride ions, so substitution was expected. However, the addition of 0.37 mol% LiI yielded no changes above 200°C, while at lower temperatures the conductivity appeared to decrease with a steeper activation energy. One possible explanation is that the amount of dissolved iodide is lower than the background impurity level (e.g., because the solubility limit is low), and simultaneously that an association reaction is

responsible for the change at low temperatures. The fit line in the extrinsic and association region are

$$\text{regime} \quad \text{II}: \qquad \sigma_{ion}T = 10^{5.64}\exp\left(-0.78\frac{\text{eV}}{k_B T}\right)\frac{\text{SK}}{\text{cm}} \tag{4.42}$$

$$\text{regime} \quad \text{III}: \qquad \sigma_{ion}T = 10^{6.55}\exp\left(-0.85\frac{\text{eV}}{k_B T}\right)\frac{\text{SK}}{\text{cm}} \tag{4.43}$$

It is noteworthy that preliminary measurements were performed at higher temperatures, and these data suggested that the conductivity of Li_2Te starts to plateau above 700°C (Figure 4.17. Such a plateau could reflect a transition to a fully disordered (superionic) sublattice as occurs in PbF_2.[123] This finding merits further investigation in future work.

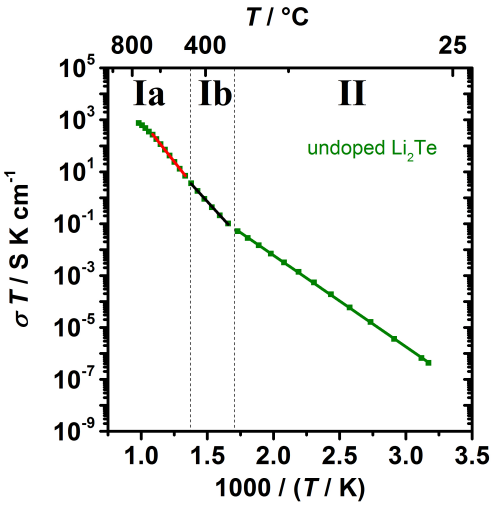

Figure 4.17: The observed bend of the high temperature conductivity of Li_2Te may indicate a transition to a superionic state above 700 °C.

4.5 Evaluation of thermodynamic and kinetic parameters: A detailed point defect model

The enthalpies and entropies of Frenkel disorder, vacancy migration, and vacancy-dopant association can now be extracted and compared to literature.

For halide-doped Li_2X, the vacancy and interstitial mobility in the extrinsic regime can be

calculated from Equation 2.30 using the conductivity measurements and the known dopant amounts. For Li_2O only vacancy transport was observed in both the undoped and LiF doped samples. Comparing both impurity concentrations, which are below the solubility limit, good agreement is seen as shown in Figure 4.18.

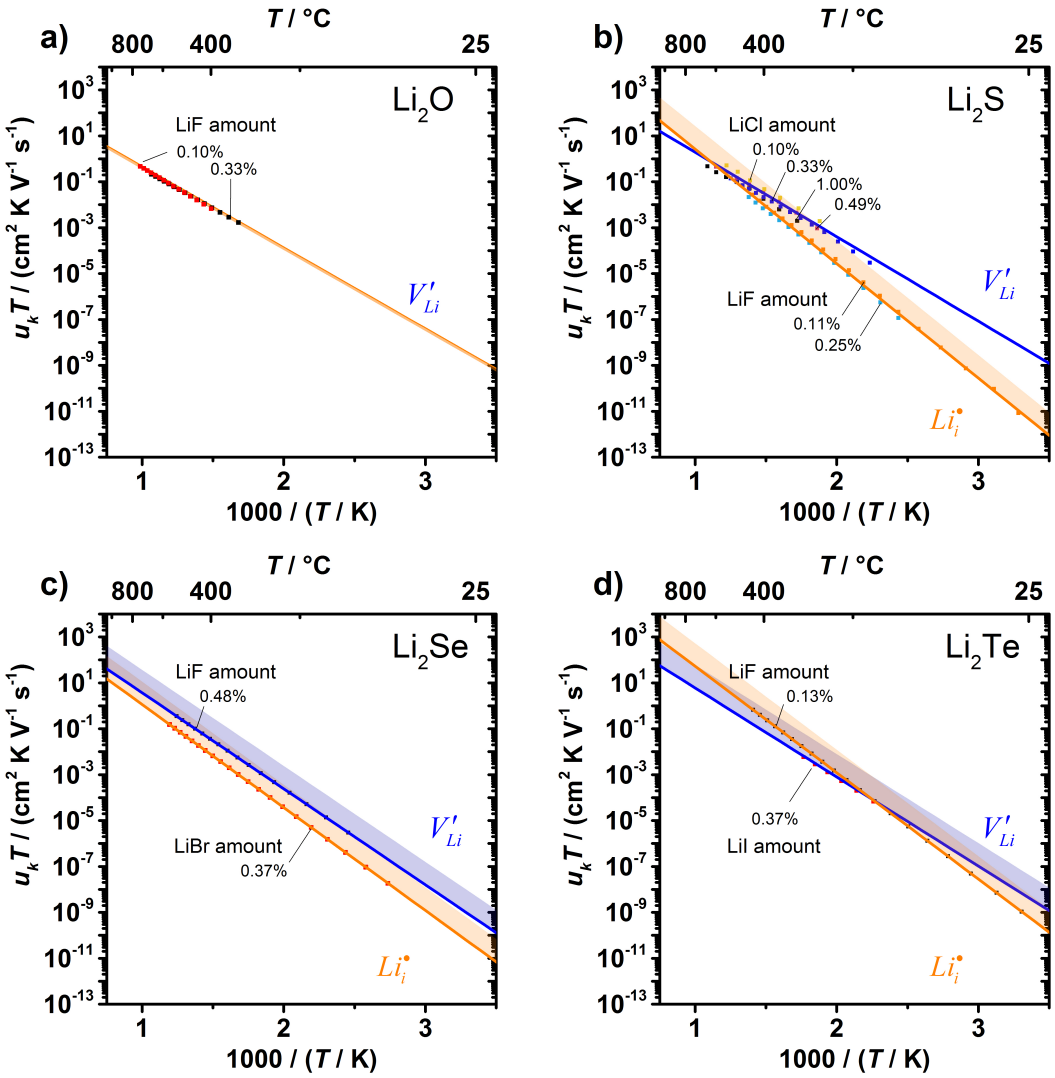

Figure 4.18: Mobilities of interstitials and vacancies of all four materials. Shaded regions indicated the uncertainty in the dissolved doping concentration.

It was shown in Figure 4.14b for Li_2S, that interstitial and vacancy transport can be dominating depending on doping. The solubility limit for LiF was ≤ 0.11 mol% and therefore the mobility of both samples is calculated according to this. However, the solubility limit

could be up to an order of magnitude lower, and this uncertainty is indicated by the shaded region of the interstitial mobility. For LiCl doped Li_2S the solubility limit was ≥ 0.5 mol%, and good agreement is observed for the vacancy mobility from four different samples.

It is expected, that the solubility limits for doping in Li_2Se and Li_2Te are similar to Li_2S and Li_2O. However, due to the lack of several doped samples for Li_2Se and Li_2Te, full dissolution of the indicated impurity concentrations was assumed for the calculation of the mobilities. The concentrations of dopants in Li_2Se and Li_2Te are expected to be within one order of magnitude lower than indicated, however, even smaller concentrations would be possible, but are considered less likely.

A transition from vacancy- to interstitial-dominated conduction was found previously in both BaF_2[124] and β-PbF_2,[110] while in SrF_2[94] a crossover was not observed. The results in Figure 4.18 show that for Li_2S and Li_2Te a similar crossover occurs. The interstitial mobility is not yet accurately known for Li_2O due to a low solubility of negative dopants. For Li_2Se uncertainty exists, but a transition may occur above 800 °C.

The plotted mobilities in Figure 4.18a) are derived from the equations reported with the conductivity plots. Rearranging Equation 2.31 and considering the relevant concentrations, average mobilities are obtained. For Li_2O Equation 4.8 and 4.10 result in a lithium vacancy mobility of

$$\mathrm{Li_2O} \qquad u_{V'_{Li}} T = 10^{3.22\pm0.16} \exp\left(-0.70 \pm 0.03 \frac{\mathrm{eV}}{k_B T}\right) \frac{\mathrm{cm^2 K}}{\mathrm{Vs}} \tag{4.44}$$

For Li_2S Equation 4.26, 4.28 and 4.30 give the lithium vacancy mobility and 4.21 and 4.23 result in interstitial mobility of

$$\mathrm{Li_2S} \qquad u_{V'_{Li}} T = 10^{3.93\pm0.20} \exp\left(-0.73 \pm 0.01 \frac{\mathrm{eV}}{k_B T}\right) \frac{\mathrm{cm^2 K}}{\mathrm{Vs}} \tag{4.45}$$

$$u_{Li_i^\bullet} T = 10^{5.3\pm1} \exp\left(-0.99 \pm 0.01 \frac{\mathrm{eV}}{k_B T}\right) \frac{\mathrm{cm^2 K}}{\mathrm{Vs}} \tag{4.46}$$

For Li_2Se uncertainty exists in the absolute doping concentration. Considering full dissolu-

tion of LiF and Equation 4.31 or for LiBr Equation 4.32 than the mobilities are

$$\mathrm{Li_2Se} \qquad u_{V'_{Li}} T = 10^{4.75+1} \exp\left(-0.83 \pm 0.08 \frac{\mathrm{eV}}{k_B T}\right) \frac{\mathrm{cm^2 K}}{\mathrm{Vs}} \tag{4.47}$$

$$u_{Li_i^\bullet} T = 10^{4.54+1} \exp\left(-0.89 \pm 0.1 eV \frac{\mathrm{eV}}{k_B T}\right) \frac{\mathrm{cm^2 K}}{\mathrm{Vs}} \tag{4.48}$$

The uncertainties in the enthalpies are due to comparison with nominally undoped Li_2Se and Li_3N doped Li_2Se while the pre-factors have approximated uncertainties that allow for up to 10 times lower solubility limits than calculated. The same approach was used for calculating the mobilities in Li_2Te:

$$\mathrm{Li_2Te} \qquad u_{V'_{Li}} T = 10^{4.66+1} \exp\left(-0.77 \pm 0.06 \frac{\mathrm{eV}}{k_B T}\right) \frac{\mathrm{cm^2 K}}{\mathrm{Vs}} \tag{4.49}$$

$$u_{Li_i^\bullet} T = 10^{6.36+1} \exp\left(-0.92 \pm 0.1 \frac{\mathrm{eV}}{k_B T}\right) \frac{\mathrm{cm^2 K}}{\mathrm{Vs}} \tag{4.50}$$

A comparison to previously studied fluorite compounds is shown in Figure 4.19. The slopes and even absolute magnitudes are remarkably similar between the fluorites and antifluorites.

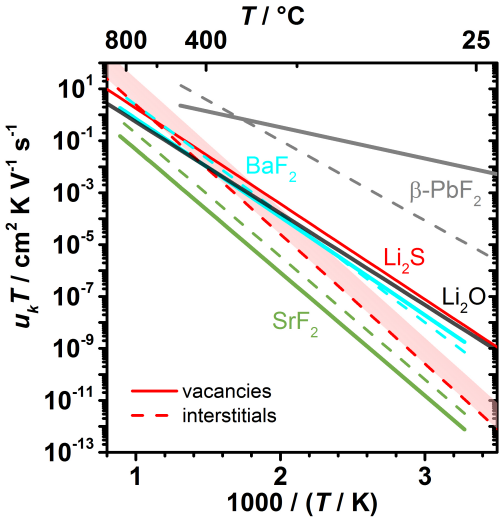

Figure 4.19: Mobilities of interstitials and vacancies of Frenkel disordered cubic fluorites (PbF_2,[110] BaF_2,[124] and SrF_2[94]) and antifluorites (this work) are shown.

Turning to the intrinsic regime, at the transition from regime II to I, the concentration of both lithium vacancies or interstitials are known due to doping and Equation 2.17. Consequently the Frenkel equilibrium constant can be evaluated for Li_2X. The intrinsic concentration of lithium vacancies and interstitials in Li_2O and Li_2S was independently studied by neutron diffraction previously. Good agreement is obtained for the slopes as shown in Figure 4.20 between this work (line) and the neutron data (points) after converting the interstitial site occupancy factor[52,61] to units of concentration.

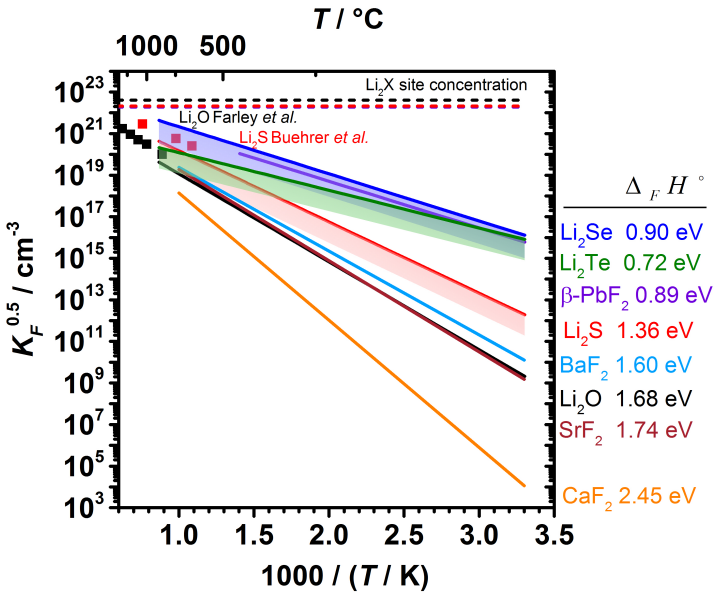

Figure 4.20: Intrinsic defect concentrations of Frenkel disordered fluorites (PbF_2,[110] BaF_2,[124] CaF_2,[125] and SrF_2[94]) and antifluorites (Neutron data Li_2O[52] and Li_2S[60]) are plotted as a function of inverse temperature. The colored ranges represent the uncertainty from impurity concentrations.

The absolute concentrations obtained from neutron diffraction measurements are found to be typically higher than from conductivity measurements.[126] The agreement still provides good evidence for the defect model presented. Compared to previously studied alkaline earth fluoride compounds, the thermodynamics of the Frenkel disorder show a decrease in enthalpy and increase in entropy upon going to more polarizable anions (from Ca to Pb - Meyer Neldel rule). These results support the idea that fluorite and antifluorite materials behave analogously in terms of defect chemistry. In both structures, the increasing

polarizability of the immobile ion leads to higher intrinsic defect concentrations and higher mobilities. In both fluorite and antifluorite, the interstitial mobility typically overtakes the vacancy mobility when the temperature increases.

The Frenkel equilibrium was evaluated assuming interstitial transport in regime I for Li_2S, Li_2Se, and Li_2Te and vacancy transport in regime I for Li_2O. For lithium oxide the Frenkel equation was obtained by dividing Equation 4.4 by 4.44 which results in

$$K_{F,Li_2O} = 10^{46.6\pm0.4} \exp\left(-1.68 \pm 0.06 \frac{\text{eV}}{k_B T}\right) \text{cm}^{-6} \tag{4.51}$$

The same approach for Li_2S using Equation 4.18 and 4.46 results in

$$K_{F,Li_2S} = 10^{47.2\pm1} \exp\left(-1.36 \pm 0.02 \frac{\text{eV}}{k_B T}\right) \text{cm}^{-6} \tag{4.52}$$

From Equation 4.36 and 4.48 for Li_2Se, and for Li_2Te from 4.37 and 4.50, it follows

$$K_{F,Li_2Se} = 10^{47\pm1} \exp\left(-0.90 \pm 0.2 \frac{\text{eV}}{k_B T}\right) \text{cm}^{-6} \tag{4.53}$$

$$K_{F,Li_2Te} = 10^{43.8\pm1} \exp\left(-0.72 \pm 0.2 \frac{\text{eV}}{k_B T}\right) \text{cm}^{-6} \tag{4.54}$$

An extrapolation of the intrinsic Frenkel behavior and Equation 2.6 allows for the calculation of the Frenkel entropy. From the extrapolated intercepts of the mobility data and Equation 2.30 the migration entropy was calculated. Both entropies are summarized for all four materials in Table 4.3. For the calculation the concentrations are converted from mol% to cm^{-3} by $\frac{[k]N_A\rho_{Li_2X}}{M_{Li_2X}}$ with molar mass M (29.88, 45.94, 92.84, and 114.48 g/mol for the four materials) and density ρ (2.01, 1.66, 2.85, and 3.40 g/cm^3).

The association behavior observed when doping Li_2X with halides is analyzed with the help of Equation 2.13 and 2.22 in regime III. The entropies of association are deduced combining the pre-factor of K_A and Equation 2.13. Considering 0.1 and 0.2 mol% LiF doped

Li_2O, the averaged derived association constant follows from Equation 4.7, 4.9, and 4.44 to

$$K_{A,Li_2O} = 10^{-22.6\pm0.4} \exp\left(0.33 \pm 0.06 \frac{\text{eV}}{k_B T}\right) \text{cm}^{-3} \tag{4.55}$$

$$\tag{4.56}$$

The same analysis applied to Li_2S, considering Equation 4.25, 4.27, 4.45, and averaging leads to

$$K_{A,Li_2S} = 10^{-22.7\pm1.3} \exp\left(0.22 \pm 0.08 \frac{\text{eV}}{k_B T}\right) \text{cm}^{-3} \tag{4.57}$$

$$\tag{4.58}$$

while for the undoped Li_2S

$$K_{A,Li_2S} = 10^{-25.5} \exp\left(0.66 \frac{\text{eV}}{k_B T}\right) \text{cm}^{-3} \tag{4.59}$$

$$\tag{4.60}$$

and single crystal sample it follows

$$K_{A,Li_2S} = 10^{-26.1\pm1.3} \exp\left(0.66 \pm 0.08 \frac{\text{eV}}{k_B T}\right) \text{cm}^{-3} \tag{4.61}$$

$$\tag{4.62}$$

For both single crystal (4.19 and 4.20) and undoped Li_2S (4.16 and 4.17) a doping concentration of 30 ppm was estimated from ICP-OES measurements. Considering the preliminary dataset of LiBr doped Li_2Se it follows

$$K_{A,Li_2Se} = 10^{-25.1\pm1.3} \exp\left(0.46 \frac{\text{eV}}{k_B T}\right) \text{cm}^{-3} \tag{4.63}$$

LiI-doped Li_2Te does show a small deviation to lower conductivities as well, and by using

Equation 4.43 and 4.49 we get

$$K_{A,Li_2Te} = 10^{-21.6\pm2} \exp\left(0.22 \pm 0.12 \frac{\text{eV}}{k_B T}\right) \text{cm}^{-3} \tag{4.64}$$

The interpretation of the defect model is based on the assumption that ionic conductivity is dominating over the whole temperature and doping range. This was corroborated by measuring the conductivity (in AC measurements) of a Li_2S pellet equilibrated to different lithium activities as shown in Figure 4.21.

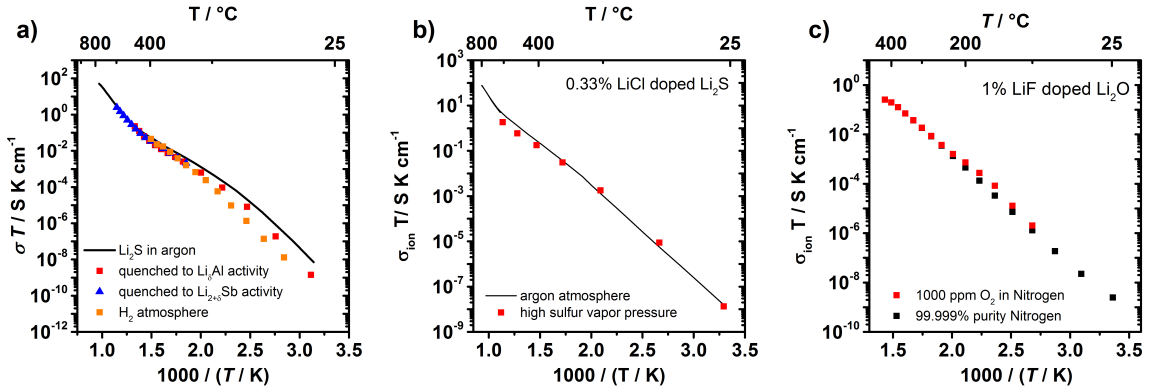

Figure 4.21: Conductivity as a function of temperature for Li_2X quenched to a) different lithium activities and equilibrated to different b) sulfur or c) oxygen partial pressures.

Different activities were set by sintering Li_2S with Li, LiAl or Li_2Sb, Li_3Sb mixtures at high temperatures or by measuring Li_2S in hydrogen atmosphere at high temperatures to achieve high lithium activities due to

$$Li_2S + H_2 \rightarrow H_2S + V_S^{\bullet\bullet} + 2e' + 2Li_{Li}^{\times} \tag{4.65}$$

Equivalently this can be expressed by varying the sulfur partial pressure by

$$S_n + nV_S^{\bullet\bullet} \rightarrow nS_S^{\times} + 2nh^{\bullet} \tag{4.66}$$

Low lithium or high sulfur activities were obtained by measuring the conductivity in an atmosphere of argon flowing over molten sulfur. The partial pressure of sulfur is estimated

to 10^{-2} mbar.[127] Lithium oxide was measured both in nitrogen and at 1000 ppm oxygen in nitrogen. The results are shown in Figure 4.21c. In all cases the conductivity was independent upon changes in lithium activity in agreement with the assumption of predominant ionic disorder.

Table 4.1 compares all available literature results found for defect parameters of Li_2O. The agreement is good with Biefeld *et al.*[42] and considering different doping levels with Chadwick *et al.*[12] and Matsuo *et al.*[43] Similarly, $\Delta_m H$ values obtained for vacancy transport in Li_2O are within a range of 0.3 to 0.9 eV. Consistently, theoretical calculations on the vacancy transport, *i.e.* $\Delta_m H$, show lower values by a factor of 2 and overestimate the Frenkel formation enthalpy. Several references mentioned in the introduction considering transport mechanisms in Li_2O and Li_2S are not reproduced in the tables below due to unreported enthalpies and entropies. The Frenkel enthalpy and entropy obtained from previous works is typically not discussed in terms of a defect model but report the slopes obtained at high temperatures. However, the agreement is still poor between most reports.

Results obtained for Li_2S in this work are compared to previous literature in Table 4.2. The lithium vacancy migration enthalpy measured from several samples (doped, poly-, and single crystal) in this work ranges from 0.57 eV to 0.73 eV. Good agreement is obtained with previous experimental values of 0.70 eV to 0.74 eV, while a lower value was predicted by DFT calculations. In this work, the LiCl-doped samples tend to reach higher enthalpies compared to both undoped single and polycrystalline samples (0.57 and 0.64 eV, respectively), which is an indication of non-ideal behavior in the LiCl-doped samples due presumably to defect interaction and a non-ideally dilute situation any more. Considering the lithium interstitial migration enthalpy again the theoretical predictions (0.45 eV for interstitialcy and 1.58 eV for interstitial hopping mechanisms) do not agree with the measurements.

Table 4.1: Literature compared to results from Li_2O of this work. Associating species ($Y_X^\bullet$) vary within references.

Method	Source	Frenkel		Migration				Association	
				V'_{Li}		$Li_i^\bullet$		$(V'_{Li}Y_X^\bullet)$	
		$\Delta_F H^\circ$ $[eV]$	$\Delta_F S^\circ$ $[k_B]$	$\Delta_m H$ $[eV]$	$\Delta_m S$ $[k_B]$	$\Delta_m H$ $[eV]$	$\Delta_m S$ $[k_B]$	$\Delta_A H^\circ$ $[eV]$	$\Delta_A S^\circ$ $[k_B]$
EIS	**this work**	**1.68±0.06**	**5.2±0.2**	**0.70±0.03**	**2.5±0.02**			**0.33±0.06**	**-0.3±0.6**
NMR, EIS	[10]	1.3		0.55					
EIS	[12]	2.1 - 2.5	4.9 - 8.2	0.21 - 0.49	-1.3 - 2.75				
MD	[16]	2.0							
EIS, NMR	[39]	1.3±0.2		0.55±0.05		0.3± 0.05		0.27	
EIS	[41]			0.94					
EIS	[42]			0.6 - 0.8					
NMR	[43]	1.2 - 1.3		0.38 - 0.52					
EIS	[44]			0.67 - 0.73					
NMR, EIS	[47]	1.3		0.63				0.75	
Neutron	[52]	2.1							
DFT	[53]	2.72±0.04	7.8	0.53±0.02				0.75	
DFT	[54]			0.9 - 1.1					
EIS	[128]	1.2 - 1.3		0.4 - 0.5					
DFT	[129]	2.55		0.26		0.64		-0.94	
DFT	[130]							0.2	
EIS	[131]	2.37 - 2.6	8 - 10.9	0.18 - 0.5	-1.41 - 2.6	0.45 - 1.2	3.19 - 6.0		
DFT	[132]	2.2		0.34		0.58			

Table 4.2: Comparison of literature values with those obtained in this work for Li_2S.

		Frenkel		Migration				Association	
				V'_{Li}		$Li^{\bullet}_{i}$		$(V'_{Li}Y^{\bullet}_{X})$	
Method	Source	$\Delta_F H^\circ$ $[eV]$	$\Delta_F S^\circ$ $[k_B]$	$\Delta_m H$ $[eV]$	$\Delta_m S$ $[k_B]$	$\Delta_m H$ $[eV]$	$\Delta_m S$ $[k_B]$	$\Delta_A H^\circ$ $[eV]$	$\Delta_A S^\circ$ $[k_B]$
EIS	**this work**	**1.36±0.02**	**5.7±0.7**	**0.73±0.01**	**6.4±0.3**	**0.99±0.01**	**8.9±0.4**	**-0.22±0.08**	**-1.8±3.1**
NMR, EIS	[10]	1.5		0.7					
EIS	[41]			0.74					
EIS	[56]			0.74					
EIS	[57]			0.9 - 1.2					
NMR	[58]	1.52		0.70					
DFT	[62]			0.27		0.45			
DFT	[63]	1.31							
DFT	[64]	1.8							

Results for ionic transport in all four materials are compared in Table 4.3, that are in accord with the defect thermodynamics established for region I in Figure 2.3. Ionic disorder is dominating and no transition into region P (hole-dominating) or N (electron-dominating) was observed in this work. A graphical representation of the results of the defect model-

Table 4.3: Thermodynamic and kinetic defect parameters obtained for Li_2X. (Y refers to F, Cl, Br, or I, for Li_2O, Li_2S, Li_2Se, and Li_2Te, respectively.)

		Li_2O	Li_2S	Li_2Se	Li_2Te
Frenkel	$\Delta_F H^\circ$ /eV	1.68±0.06	1.36±0.02	0.90	0.78±0.06
	$\Delta_F S^\circ$ /k_B	2.5±0.1	5.7±0.7	5.0±3	-1.9±3
V'_{Li} Migration	$\Delta_m H$ /eV	0.70	0.73±0.01	0.83	0.77
	$\Delta_m S$ /k_B	-	6.4±0.3	-	-
$Li_i^\bullet$ Migration	$\Delta_m H$ /eV	-	0.99±0.01	0.99	0.92
	$\Delta_m S$ /k_B	-	8.9±0.4	-	-
$(V'_{Li}Y_X^\bullet)$ Association	$\Delta_m H$ /eV	-0.33	-0.22±0.08	-0.46	-0.22±0.12
	$\Delta_m S$ /k_B	-	-1.8±3.1	-7.6±0.6	-0.2±0.02

ing obtained in this work for Li_2S are shown in Figure 4.22. The defect concentrations are plotted as a function inverse temperature and oxygen partial pressure. The unknown parameters such as $K_O = 10^{-75\sqrt{bar}}/_{cm^{12}}$ and $K_B = 10^{25}$ cm^{-6} are estimates. The concentrations calculated from estimates are plotted as dotted lines and therefore the transition from the intrinsic into P or N defect regimes are schematic.

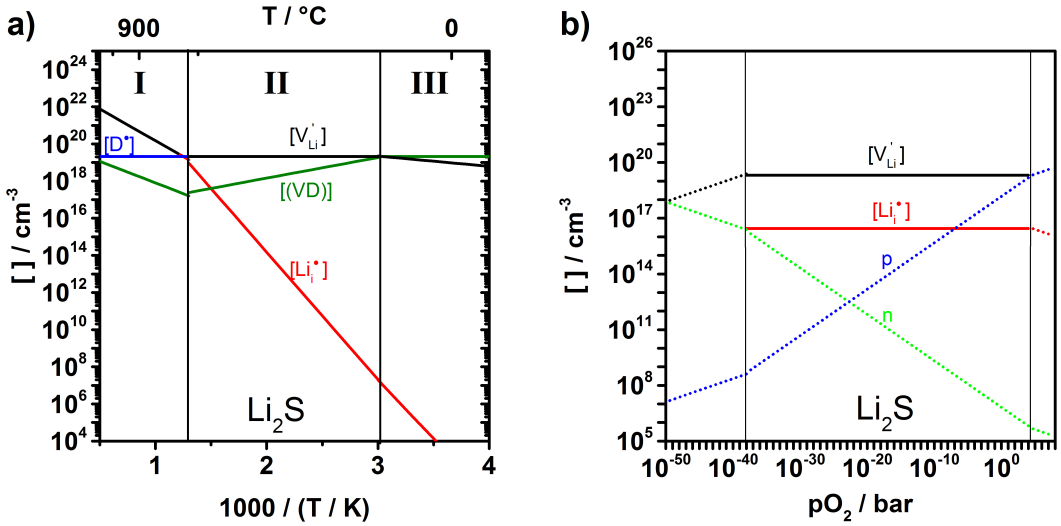

Figure 4.22: Defect concentrations calculated from the obtained thermodynamic parameters for Li_2S as a function of a) inverse temperature ($[D^\bullet] = 0.1$ mol%) and b) partial pressure of oxygen (T = 600 K, $[D^\bullet] = 0.1$ mol%).

A comparison between Li_2O and Li_2O_2 is also possible and shown in Figure 4.23.

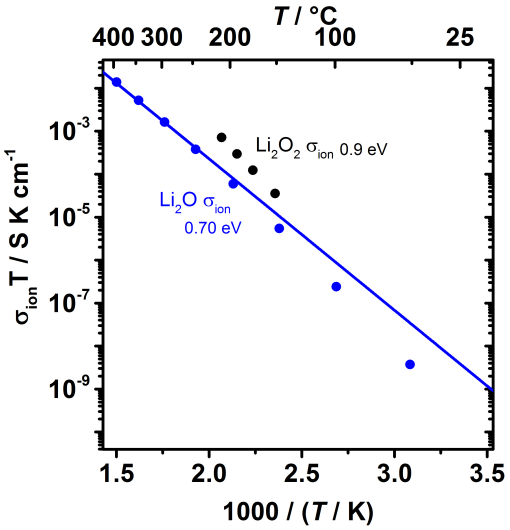

Figure 4.23: Comparison of the conductivity versus inverse temperature of undoped Li_2O with literature data on Li_2O_2 (data from Gerbig *et al.*[24])

In both crystal structures, lithium vacancies are more mobile at low temperatures, with slightly higher activation energies for the peroxide. Association further affects both systems

at low temperatures. While Li_2O exhibits predominant ionic conductivity, it was shown by Gerbig *et al.* that the peroxide is a mixed conductor with $t_{ion} = 0.9$ in a temperature range between 25 and 200 °C. However, it should be emphasized that the high electronic conductivity observed for Li_2O_2 may be affected by leakage currents which are discussed below for Li_2O.

For undoped Li_2X the ionic conductivities are plotted in Figure 4.24 together with those for single crystal fluorites. The global trend of increasing polarizability of the anion is reflected in the intrinsic regime of the conductivity data where Frenkel enthalpies are decreasing. At low temperatures and for high purity fluorites, association is absent and only one low temperature regime (extrinsic) is obtained. For the same reason the conductivities in the antifluorite structure are higher since higher dopant concentrations are assumed. For Li_2Te and PbF_2 the defect formation energies are favorable and these cause very high conductivities that are among the highest observed in the solid state at such high temperatures (800 °C).

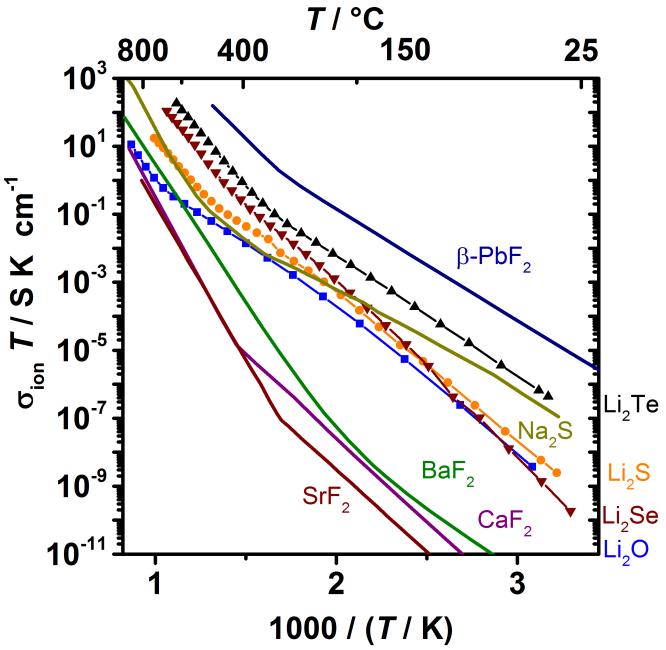

Figure 4.24: Comparison of conductivities obtained from several nominally undoped fluorites(CaF_2,[125] BaF_2,[124] β-PbF_2,[110] and SrF_2[94]) and antifluorites (this work and Na_2S[11]).

and β-PbF_2,[110] while in These similarities in the bulk between antifluorites and fluorites also raise questions about analogous transport at the interface, mentioned in the introduction, which will be discussed in chapter 5.

4.6 Attempts to measure the electronic conductivity

4.6.1 D.C. Polarization

D.C. polarization measurements were performed using sintered bulk pellets of Li_2O and Li_2S contacted on opposing faces by ion-blocking metal electrodes. When a current is applied, the sample becomes polarized. If the metal electrodes are fully ion-blocking, then the steady-state voltage response to an applied current can be attributed to electronic conductivity (as long as the voltage stays below the decomposition voltage). This behavior should not depend on the choice of metal, provided the metal is ion-blocking and non-reactive. Three metals were tried for Li_2O: Au, Pt, and Ru. For Au and Pt, steady-state behavior could not be reached in a reasonable time. Using Ru electrodes, stable values were reached after approximately 10 h and for several p_{O_2} steps as shown in Figure 4.25.

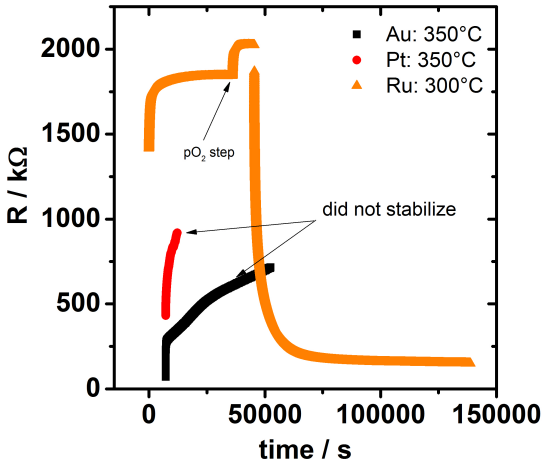

Figure 4.25: Delusive DC stoichiometric polarization results for M = Au, Pt, Ru electrodes in M | Li_2O | M cells at different temperatures, pellet dimensions and currents.

The results imply an ionic transference number of 0.9, which disagrees with the EMF results presented above showing that t_{ion} is close to 1. Thickness scaling experiments and chemical arguments also indicate that the true electronic conductivity is much lower. An alternative interpretation of the d.c. data is that the apparent electronic conductivity is actually an ionic leakage current due to reactivity of Li_2O with typical noble metal electrodes like Pt and Au. Indeed, the electrodes visibly showed corrosion after measurements, and ternary $LiRuO_2$ phase is known to exist from battery measurements on RuO_2.[133] These considerations led to the conclusion that DC polarization was not reliable for determining the electronic conductivity.

4.6.2 Hebb Wagner measurements

First attempts were made using bulk samples with LiAl and Ru electrodes for Li_2S and Li_2O. The obtained polarization is exemplarily shown in Figure 4.26. Certain voltages versus Li/Li^+ were applied and the resulting current was measured at 50 mV steps with equilibration times of several hours.

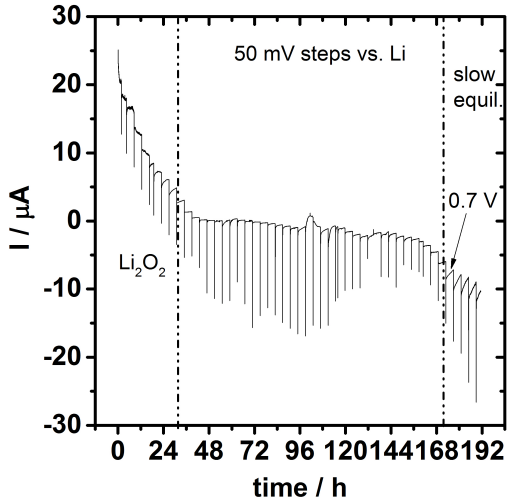

Figure 4.26: Hebb-Wagner results of bulk Li_2O with LiAl and Ru electrodes at 440°C. Theoretical decomposition voltage forming lithium peroxide is indicated as a dashed line at high voltages. Steps are in 50 mV versus Li/Li^+ and a regime with slower equilibration times is indicated at low voltages. It can be seen, that very few of the individual equilibration processes are forming clear plateaus.

Despite the long dwells, it is not clear whether equilibration was reached at any lithium activity. Equilibration also did not succeed at higher temperatures, or for Li_2S instead of Li_2O. Equilibration times exceeding several hours were tested, but these led to drift in the voltages that did not stabilize. At very long times, also the LiAl electrode slowly reacted with water from small but unavoidable leaks and from traces in the flowing argon gas. Additionally, at high temperatures, lithium diffusion at the Li_2X surface, as described in the EMF section, led to short circuits and an unreliable measurement.

In order to overcome the diffusion-limited kinetics, a microelectrode approach was pursued. Here, the applied concentration gradient does not have to equilibrate throughout the whole pellet but only in a confined region near the circular Ru microelectrode.[134] The spreading resistance from this electrode is given by

$$R_{spr} = \frac{1}{2d\sigma_{bulk}} \tag{4.67}$$

with the spreading resistance R_{spr} and the microelectrode diameter d.[87] Consequently it follows for the electronic conductivity

$$\sigma_{eon} = \frac{1}{2d}\frac{dI}{dU} \tag{4.68}$$

Many experimental efforts were made to reduce scatter in these measurements: Single crystals have been prepared and electrodes were sputtered on top without exposure to air. A micro-contact setup is evacuated to 10^{-5} mbar with a turbopump backed by a scroll pump. The sample was shielded from the heater by a Faraday cage to avoid electrical noise. Impedance measurements of the LiAl-Li_2S-Ru pellet combination (Figure 4.27) reveal that changes appear for the mid frequency semicircle, which compared to the bulk study is most likely not a feature of the sample but of the electrodes indicating non-stable electrodes. However, DC measurements are not be effected by these high frequency processes.

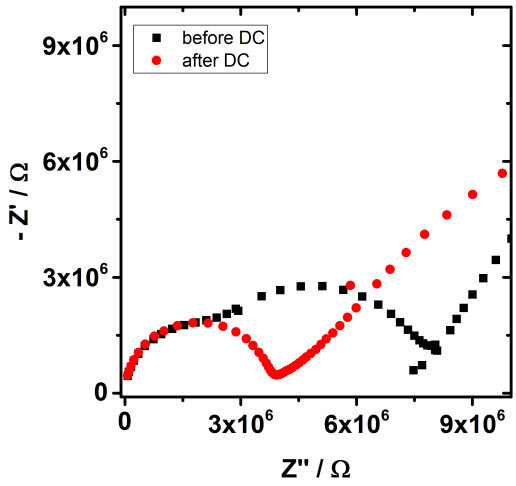

Figure 4.27: Impedance results of single crystalline Li_2S with LiAl and Ru electrodes at 300 °C before and after DC measurements. The mid frequency semicircle is due to a microelectrode decomposition.

The measured current as a function of time is shown in Figure 4.28.

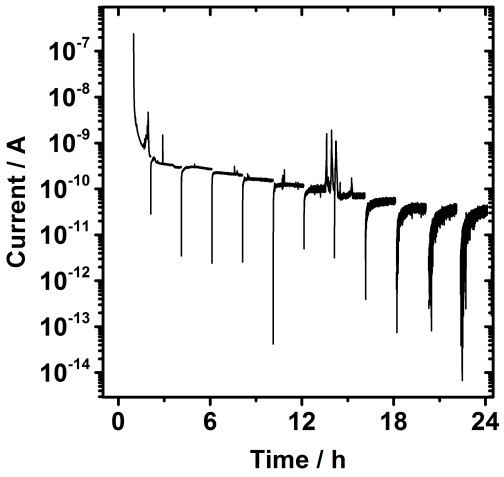

Figure 4.28: Current measurement with Ru microelectrodes on a Li_2S single crystal.

High currents are observed initially and steady-state values are rarely obtained. The electrical noise during these measurements was considerable, despite many efforts made to reduce it. The measurement of currents on the order of pA further requires more advanced

shielding of the sample and cabling due to the very high resistance of the sample. The resulting preliminary electronic conductivity of the Hebb Wagner measurements for Li_2S is shown in Figure 4.29. Steps are in 50 mV versus Li/Li^+ and electrode diameter was 175 μm.

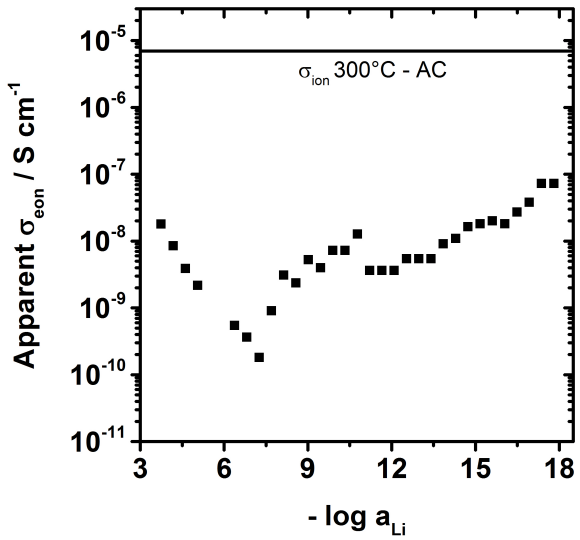

Figure 4.29: Apparent electronic conductivity obtained from microelectrode Hebb-Wagner measurements of single crystalline Li_2S with LiAl and Ru electrodes at 300 °C.

The data are consistent with the EMF measurements presented above showing an ionic transference number above 0.99, i.e. σ_{eon} is at least a factor of 100 below σ_{ion}. It was found that at extreme lithium activities approaching 1 or the decomposition limit of Li_2S, the electronic conductivity may become non negligible. Further investigation is needed to confirm this finding.

5 Results for Thin Films

In section 5.1 the thin film preparation by sputter deposition and evaporation is discussed. Growth characteristics are shown for different conditions and the films are then electrochemically investigated in section 5.2. Enhanced transport is observed which is further discussed in terms of substrate-, size- and doping effects.

5.1 Growth optimization

5.1.1 Sputter deposition

Lithium oxide

Thin films were grown from both ceramic Li_2O or elemental lithium targets with additional oxygen in the plasma. Both methods were able to deposit phase pure polycrystalline Li_2O on Al_2O_3 substrates as indicated by XRD in Figure 5.1a. However, growing Li_2O from ceramic targets had several drawbacks. First, the growth rate using a Li_2O target was approximately 10 times slower than the growth rate using a lithium target and O_2 atmosphere, since metals typically sputter much faster than oxides.[135] In the case of Li_2O, using a ceramic target led to growth times of up to 20 h. Second, the sputtered target was always water-cooled during sputtering, however, the lower thermal conductivity of the ceramic targets resulted in higher temperatures which in turn led to the decomposition of the conventional polymer epoxy used to attach the target to the water-cooled backing plate. This problem was solved by replacing the polymer epoxy with indium metal, which exhibits better heat conduction and contains no polymer. Third, discoloration of the ceramic targets was observed during operation,[68] which led, after extended sputtering, to electric discharges, sparks due to

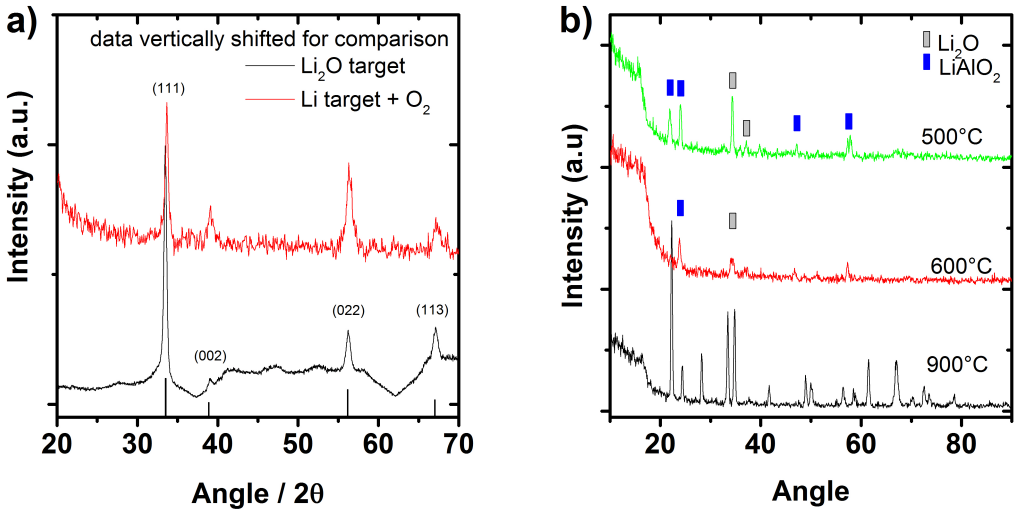

Figure 5.1: XRD of sputtered Li_2O on a) Al_2O_3 substrates from ceramic and elemental targets. Reactivity with the Al_2O_3 substrate is shown for postannealing at the indicated temperatures in b).

metallic lithium precipitation at the target surface (compare Figure 5.2), fluctuations in the plasma power, breakdown of the plasma, and target cracking and chipping. Similar issues appeared with ceramic Li_2S targets.

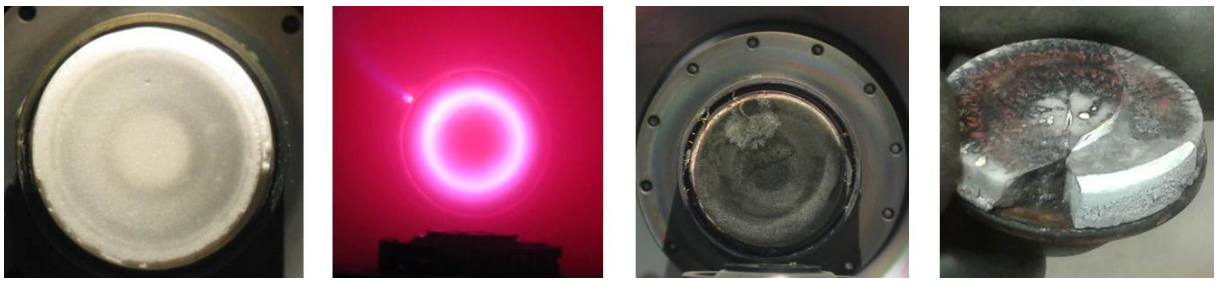

Figure 5.2: F.l.t.r: Target after few minutes of sputter deposition already shows discoloration. Sparks during sputter deposition led to severe plasma fluctuations. Debris was forming at the target surface. Discoloration and cracks were observed after more than 100h of sputter deposition.

In contrast, better film quality and growth control was achieved using an elemental lithium target in an oxygen-containing plasma. The thermodynamically more stable reaction product at 25 °C and ambient pressure is Li_2O_2; however, at 0.01 mbar and higher temperatures Li_2O is more stable, and the formation of lithium peroxide was never observed.

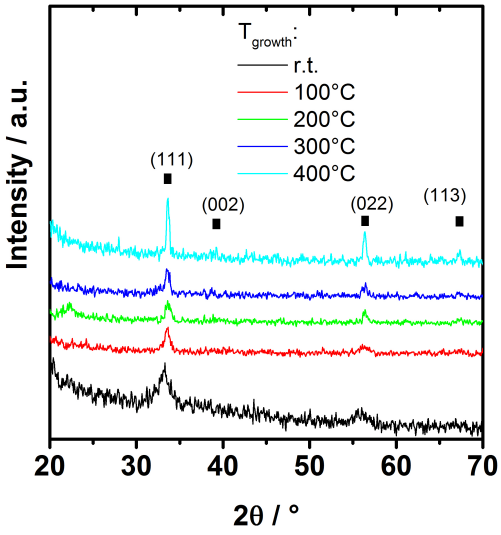

Figure 5.3: Gracing incidence XRD patterns obtained for sputter-deposited Li_2O films at different growth temperatures from a lithium target on Al_2O_3 (0001) substrates.

Phase pure Li_2O was grown from a lithium target on Al_2O_3 (0001) single crystal substrates at various temperatures as shown in Figure 5.3. Reactivity with the substrate is only observed above 400 °C. The films appear polycrystalline with no preferred orientation. Broad diffraction peaks at low deposition temperatures are observed, which indicate small grain sizes. At higher temperatures the peak width decreases and the intensity increases, indicating grain growth. Amorphous Li_2O was never detected in any characterization; however, its presence can not be ruled out. The surface morphology for films grown at different temperatures from elemental lithium at 0.01 mbar (10 % O_2 / 90 % Ar) is shown in Figure 5.4. For electrochemical characterization, dense and homogeneous films with little roughness were desired. The morphology strongly changes with small variations in growth conditions. The lattice mismatch between Li_2O and Al_2O_3 is large so polycrystalline growth is expected at all temperatures. At low temperatures (< 100 °C) the surface diffusion is expected to be low, so impinging Li_2O particles do not pack densely; instead, mounds and valleys form, leading to a rough surface. Around 150 °C the most uniform films are obtained, while above 150 °C surface diffusion is high enough to form semi-regular domains that maybe reflect terraces on the substrate. Due to a small distance between reactive plasma and deposited film, thin

film Li_2O may be removed from the substrate by the nearby plasma and redeposited on the target. However, this was technologically minimized by having target and substrate in an off-axis geometry in the plasma chamber.

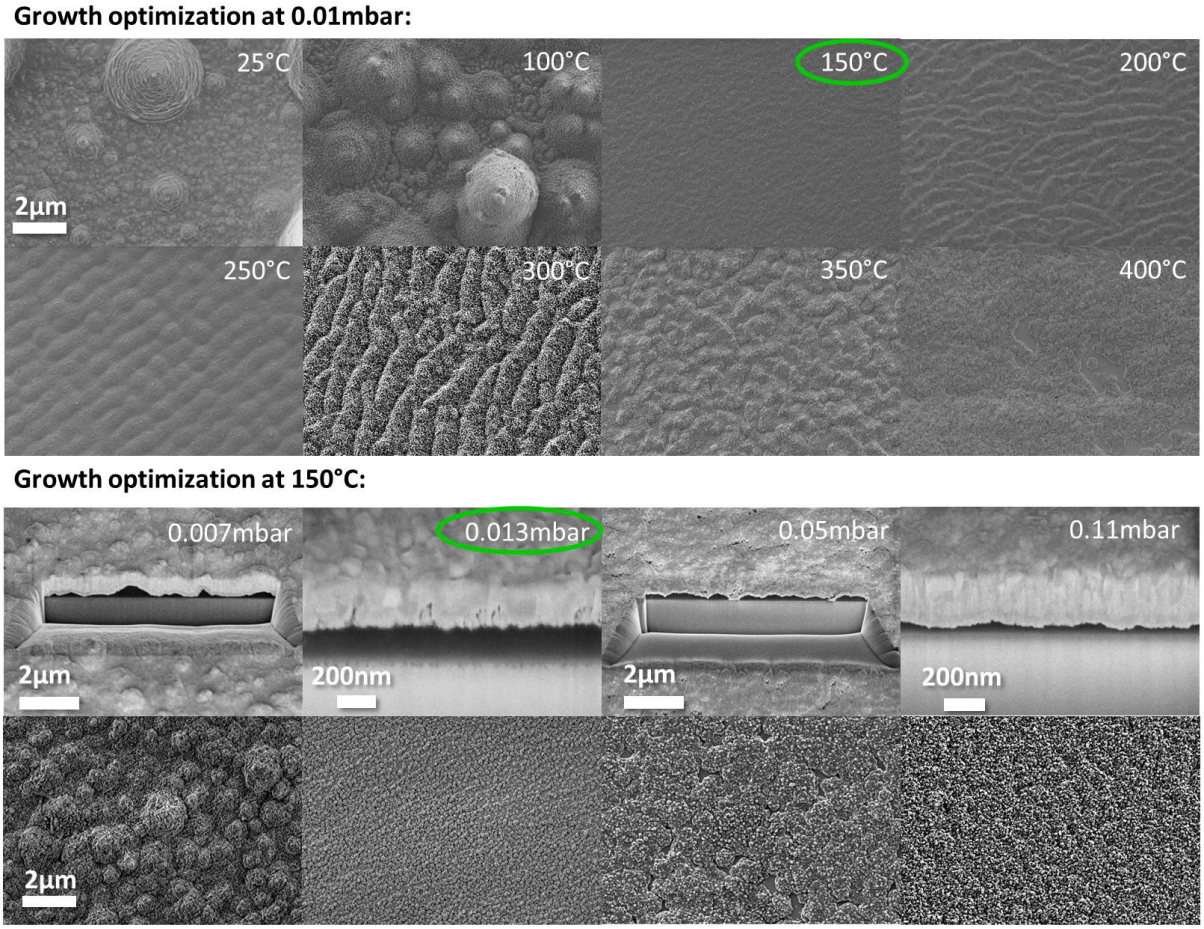

Figure 5.4: Lithium oxide thin film morphology sputtered from the elements on Al_2O_3 (0001) substrates as a function of growth temperature and pressure.

Above 300 °C coarsening becomes noticeable, and ultimately the substrate becomes exposed again, as seen for the film grown at 400 °C. The film morphology at 150 °C was further studied as a function of chamber pressure. Within the pressure limits for sputtering four conditions were tested: 0.007 mbar, 0.013 mbar, 0.05 mbar, and 0.1 mbar. Focused ion beam (FIB) cross sections (Figure 5.4) were cut and the ideal pressure was found at 0.01 mbar. At 0.007 and 0.05 mbar the films were rough and at too high pressures the films got thinner as well. The best Li_2O film obtained by sputtering was grown at 150 °C and

0.01 mbar, which was used for further electrochemical characterization. These films appear dense and non-porous on a scale detectable by SEM.

Due to the observed reactivity of Li_2O with Al_2O_3, a substrate screening led to the conclusion that many conventionally used substrates such as TiO_2, $SrTiO_3$, or other metal oxides form ternary phases with lithium at elevated temperatures. Post-annealing was studied in order to check for reactivity with the substrate and indeed Al_2O_3 forms $LiAlO_2$ at temperatures above 400 °C as shown in Figure 5.1b. MgO substrates were used instead since no ternary Mg-Li-O compound is reported. Metal halide substrates have been investigated as alternative substrates, too, but reactivity and secondary phases were observed. The electrochemical characterization of Li_2O on Al_2O_3 was limited to 350 °C and no sign for reactivity was observed at such low temperatures in any of the reported characterization techniques.

Lithium sulfide

Li_2S sputtered from lithium and sulfur targets grows phase pure and polycrystalline on MgO (100) single crystal substrates as shown in Figure 5.5.

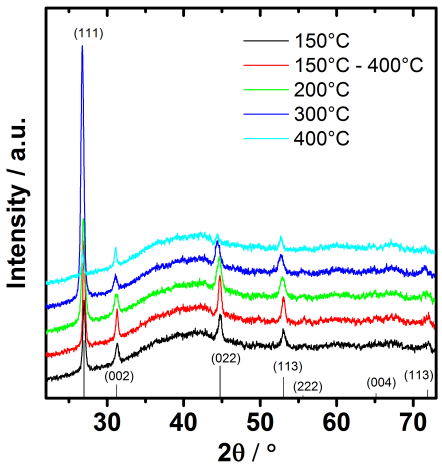

Figure 5.5: XRD patterns of Li_2S films grown on MgO (100) substrates at different temperatures. One sample (label 150 °C - 400 °C) was grown at 150 °C and then post-annealed at 400 °C. A reference pattern from bulk Li_2S (ICSD-657596) is also shown.

A preferred (111) orientation is evident. Polycrystallinity is expected in light of the lattice mismatch of Li_2S on MgO. Peak broadening at low deposition temperatures was less pronounced for Li_2S compared to Li_2O, despite small grain sizes detected in SEM. The growth was optimized by systematically varying temperature as shown in Figure 5.6.

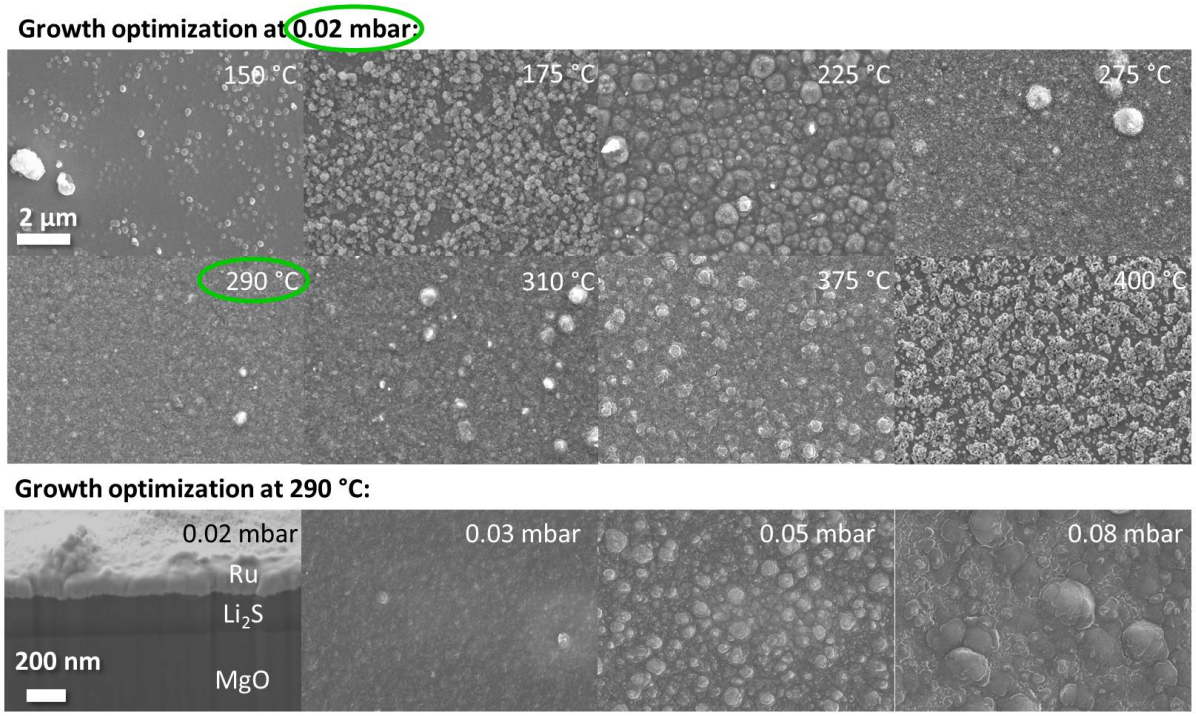

Figure 5.6: SEM images showing the surface morphology of sputtered Li_2S thin films on MgO (100) substrates at various temperatures and growth pressures.

The best morphology was obtained at 0.02 mbar and 290 °C; below and above this temperature, similar porosity and coarsening as for the Li_2O was observed. Separately, the pressure was varied while holding temperature constant; FIB-SEM images of films grown at higher pressures than 0.02 mbar reveal much rougher surfaces.

The thicknesses of several films grown under optimized conditions with different sputtering times were measured by FIB-SEM. The results are summarized in Figure 5.7. From these data, the growth rates for Li_2O and Li_2S are estimated to be 3.5 and 1.2 nm/min. Attempts were also made to measure film thicknesses with a stylus profilometer, but due to the severe humidity sensitivity, the films grew immediately after air exposure in thickness by a factor of 2-3, and the roughness also increased to become on the order of the film thickness itself.

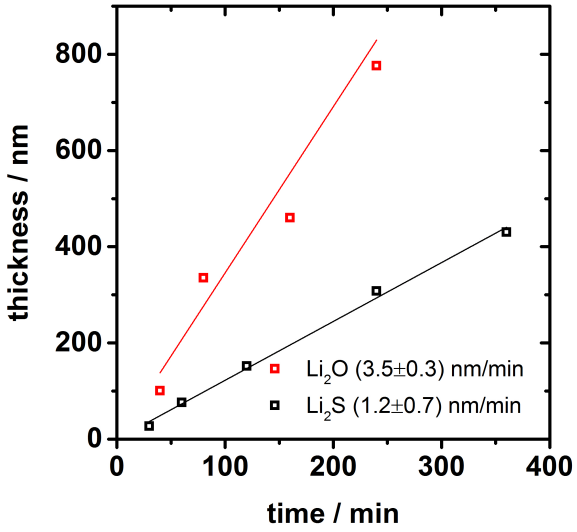

Figure 5.7: Comparison of Li_2O and Li_2S growth rates obtained from reactive sputter deposition.

To summarize, thin films sputtered from the elements at 150 °C and 0.01 mbar (Li_2O) and 290 °C and 0.02 mbar (Li_2S) appear dense, uniform and fairly smooth by FIB-SEM, phase pure by XRD and Raman, and exhibit grain sizes below 50 nm. These films are therefore suitable for electrochemical investigation.

A few additional observations are worth reporting. First, the lithium target was seen to react with the oxygen gas or residual sputtered S to form Li_2O or Li_2S on the target. Consequently, alternating between sputtering Li_2O and Li_2S in the same chamber required up to several hours of target "cleaning" by sputtering in pure argon to restore a pure lithium surface and thereby prevent cross contamination. Additionally, the sulfur target was consumed quickly and lasted for only a few films. Surprisingly, the power to sustain the sulfur plasma was lower than 5 W. Since the growth pressure of 10^{-2} mbar is fairly high, it may introduce gas molecules as impurities.

5.1.2 Molecular Beam Epitaxy

As an alternative to r.f. sputtering, evaporation in an MBE chamber was explored. Evaporation from both compound ceramic material (Li_2O and Li_2S, SnS_2) and from elemental sources (Li, S, O_2 gas, and Se) was tried.

Growing Li_2X from ceramic precursors would require temperatures above 1000 °C (compare Figure 5.8b) and crucible materials that do not react. However, Li_2X does not sublime, but decomposes upon evaporation[136,137] with lithium having the highest vapor pressure over Li_2X. Indeed, it was found in this work that high temperature evaporation of Li_2O from Al_2O_3 crucibles led to metallic conducting thin films consisting most likely of lithium. Presumably, the actively pumped MBE chamber hinders the growth of stoichiometric Li_2X and additional chalcogen has to be supplied. Al_2O_3 crucibles also react with Li_2O which leads to cracks and dysfunction of the effusion cells.

Instead, evaporation of elemental sources was tested. Lithium was evaporated from molybdenum crucibles, and sulfur and selenium from carbon crucibles. Molecular oxygen can be supplied by a leak valve.

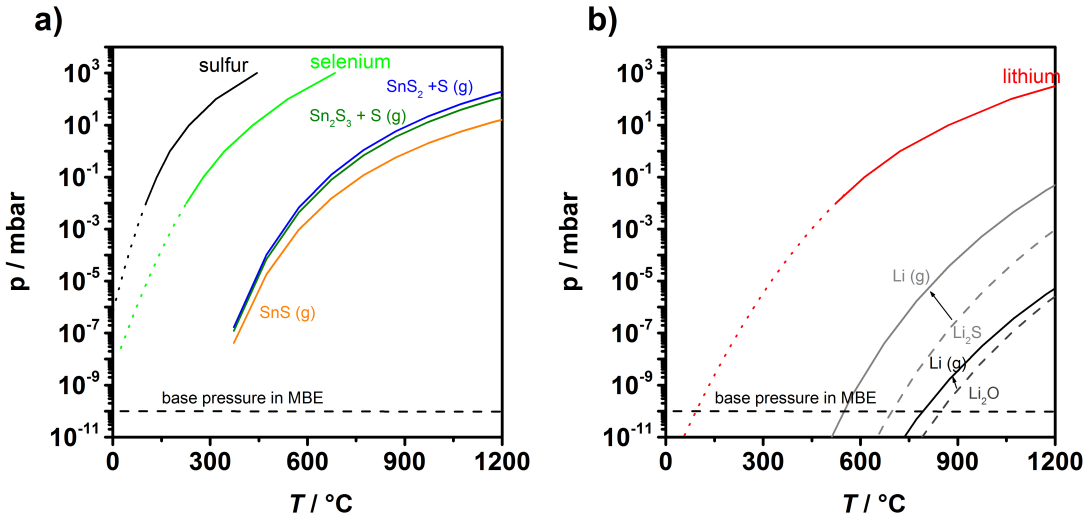

Figure 5.8: Vapor pressures relevant for growing Li_2X thin films in the MBE are shown for a) sulfur over sulfur,[127] SnS_2 and SnS_2S_3,[138] and selenium over selenium,[127] and the sublimation of SnS.[138] The vapor pressures in b) are reported for lithium over lithium,[127] Li_2S,[137] and Li_2O[139]

The vapor pressures of the elements are shown in Figure 5.8. As indicated, sulfur has a very high vapor pressure even at room temperature. It was tested if evaporation of sulfur is possible in a standard Knudsen cell but the pumping of the MBE chamber quickly consumed all sulfur in the crucible, while the background pressure was raised to 10^{-8} mbar.

Instead, metal sulfides such as SnS_2[140] has been used in the literature. Upon decomposition at high temperatures it provides a controllable flux of sulfur. SnS_2 was found to release sulfur already at 500 °C as shown by a thermogravimetric analysis in argon in Figure 5.9a).

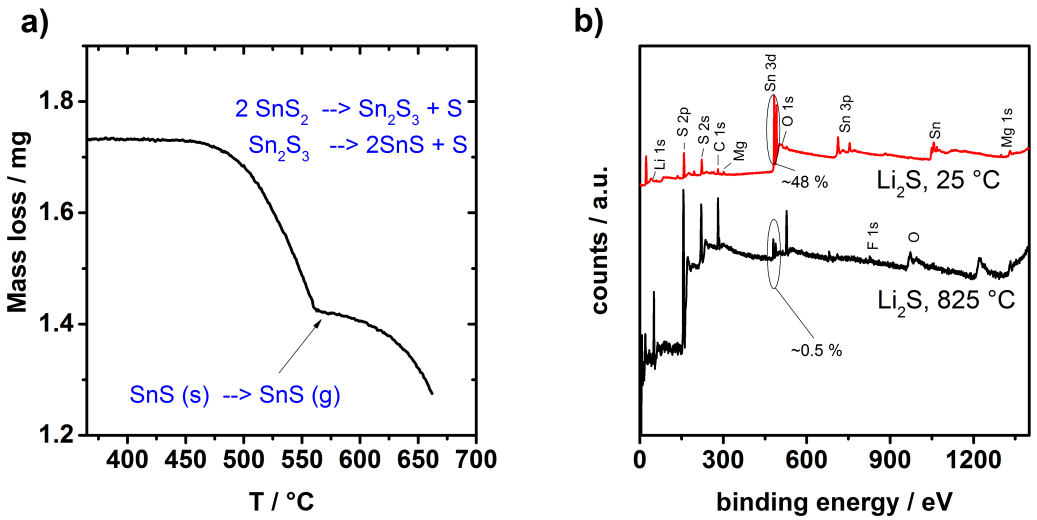

Figure 5.9: a) Thermogravimetric analysis of SnS_2 decomposition under flowing argon and b) XPS results indicating the tin concentration in the films grown at 25 or 595 °C.

The expected mass change from losing 1 sulfur into the gas phase is 17.5 %. The actual mass change up to 560 °C is in excellent agreement with this value. At 450 - 550 °C the disulfide disproportionates into Sn_2S_3 and then SnS, releasing sulfur.[138,141] Further heating above 560 °C results in the sublimation of SnS. For film growth, S release is desirable and SnS sublimation is not. Thus, the TGA data indicate that the effusion cell temperature should be held below 560 °C. In fact, measurements[140] show non-zero vapor pressures of Sn-containing species (Sn_2S_3 and SnS_2) even below 560 °C (compare Figure 5.8a). To investigate if these vapor pressures lead to measurable Sn doping, XPS was performed on a film grown from a SnS_2 source at 500 °C and with a substrate temperature of 25 or 610 °C.

The XPS results in Figure 5.9b show detectable Sn in the Li_2S thin film when the substrate temperature during growth is low.

Better morphologies were obtained at higher substrate temperatures for Li_2S, as will be shown below, and the detectable tin concentrations were well below one percent. However, the formation of a Li-Sn-S or Li-Sn phase can not be ruled out, but was never observed in this work.

Lithium oxide

Figure 5.10 shows the morphology of Li_2O films grown from elemental lithium at $5{\cdot}10^{-6}$ mbar oxygen.

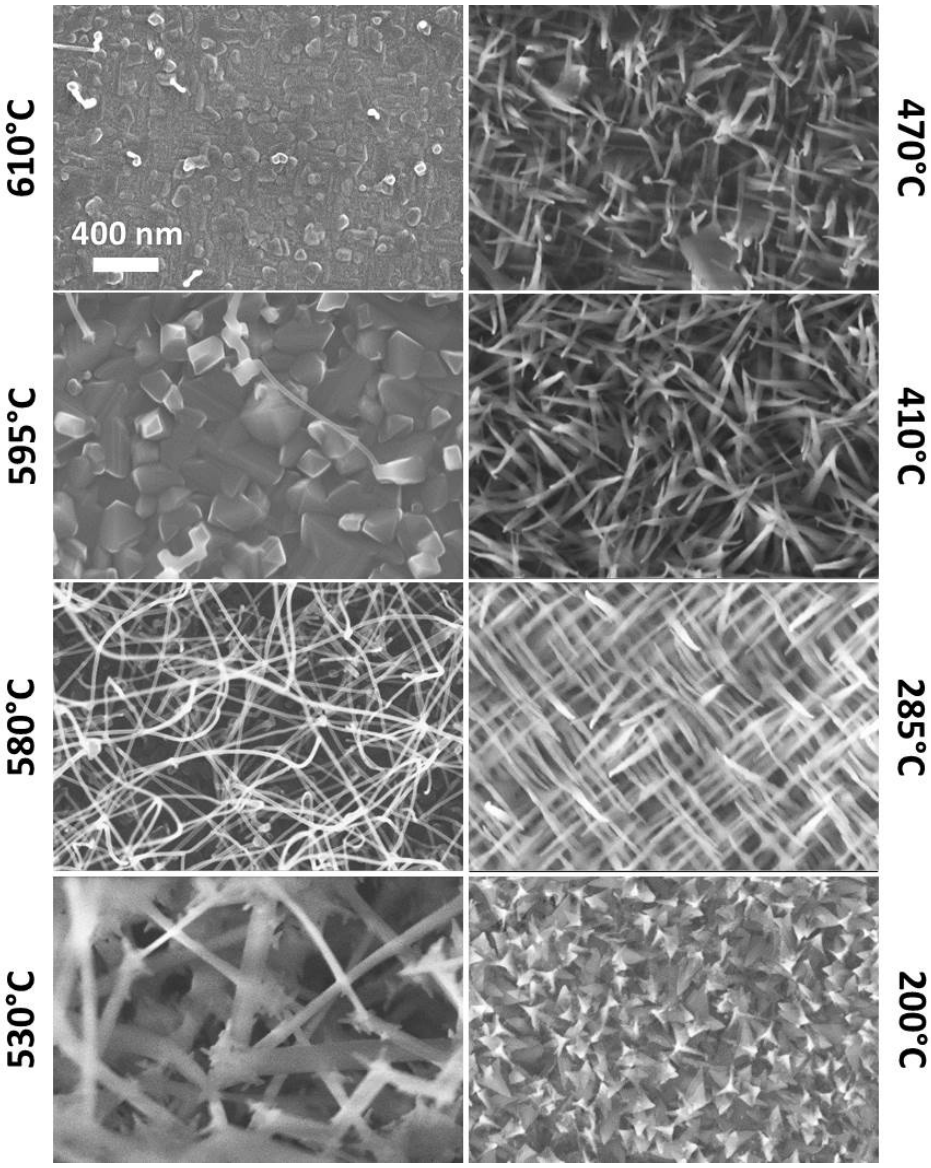

Figure 5.10: SEM images of lithium oxide thin film surface morphologies obtained from evaporation of lithium at 500 °C at $5{\cdot}10^{-6}$ mbar oxygen pressure on MgO (100) at the given substrate temperatures.

Using growth temperatures below 200°C, simple multimeter measurements revealed that electronically conducting films were obtained presumably due to incomplete oxidation of

lithium. At 200 °C, small triangular platelets of Li_2O were grown that arranged in a porous rough film on MgO substrates. Above 200 °C a needle-like morphology was obtained. At higher temperatures the needles became thinner (nanometer scale) resulting in a porous film. At temperatures above 595 °C, these needles either re-evaporated, reacted, or did not form due to low sticking coefficients, leaving a coarsened MgO surface. Varying the oxygen partial pressure (between 10^{-6} and 10^{-8}) did not improve the morphology: lower pressures either favored the growth of metallic lithium films at low temperatures or still resulted in needle-like Li_2O. Higher pressures were not feasible due to risk of oxidation of the resistive heating elements in the MBE chamber.

Li_2O grown at 200 °C was postannealed at 470 °C, but this treatment did not fully densify the films; instead, a porous, columnar film resulted as shown in Figure 5.11. Such films were not considered reliable for quantitative transport measurements.

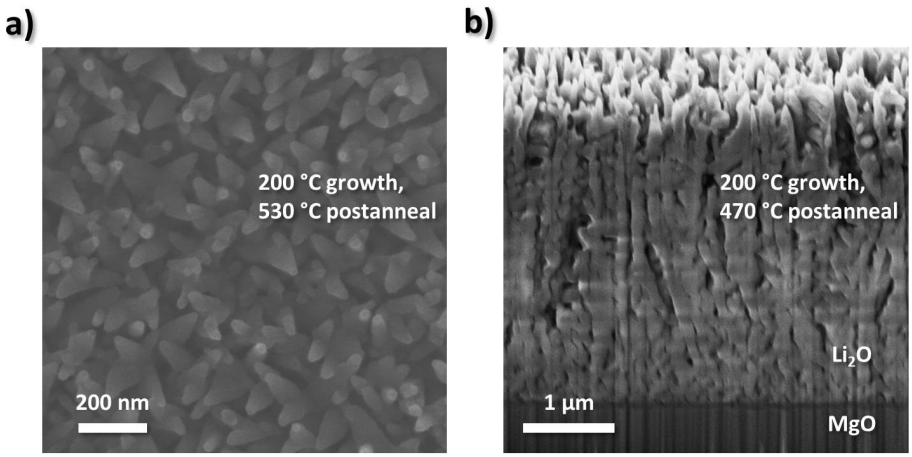

Figure 5.11: SEM image of a lithium oxide thin film grown at 200 °C and postannealed in vacuum at 470 - 530 °C.

Lithium sulfide

The impact of substrate temperature on Li_2S growth is presented in Figure 5.12.

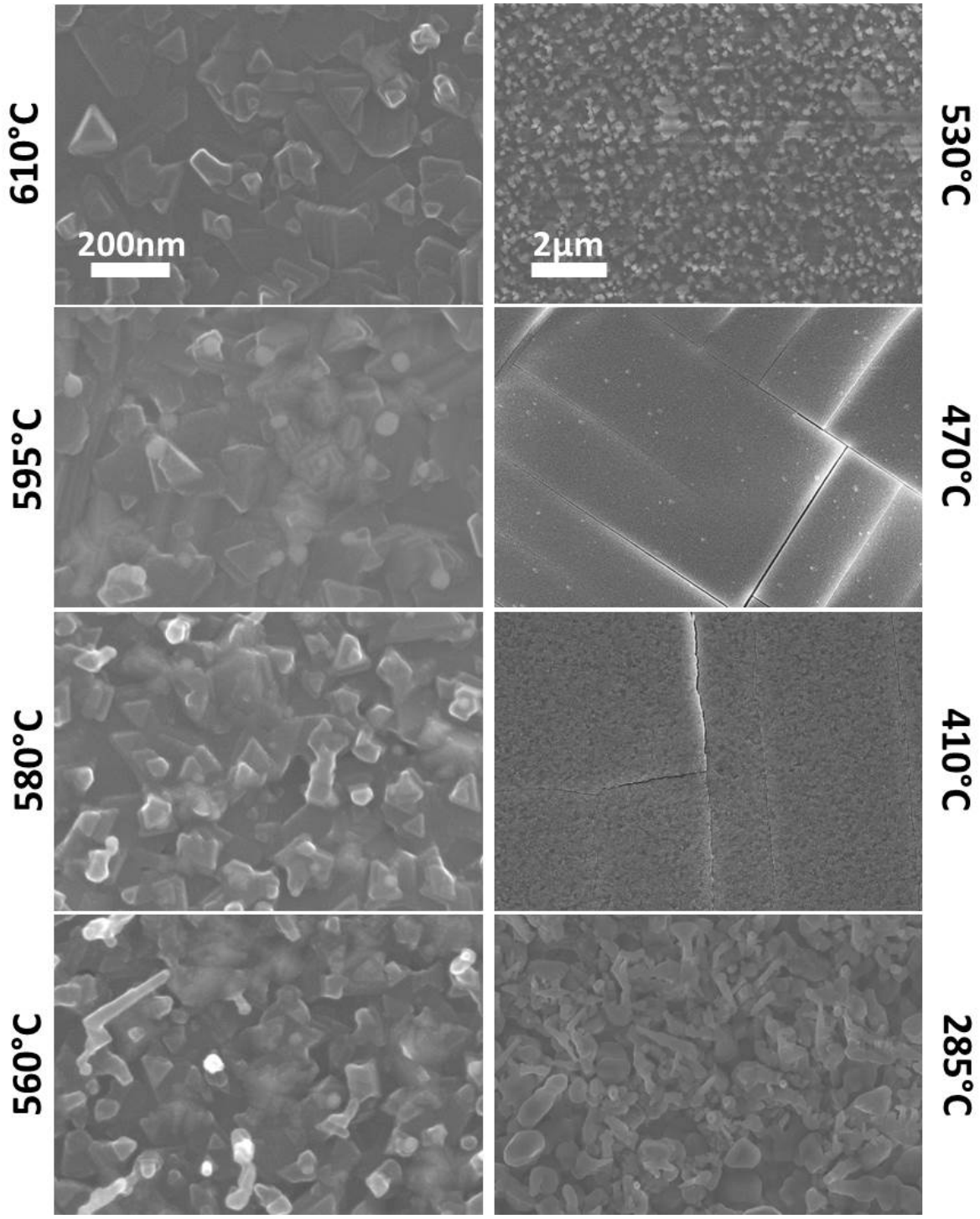

Figure 5.12: Lithium sulfide surface morphology of evaporated thin films on MgO (100) substrates from lithium and SnS_2.

The images show a granular growth at 285 °C that seems to evolve into smaller grains

and a smooth surface with linear cracks. Above 530 °C the cracks close and nanometric Li_2S platelets form. The cracks remained even for very slow substrate cooling after growth (1 °C/min). Films grown at the maximum heater temperature reveal a strong orientation in (111) direction in XRD as shown in Figure 5.13b. In comparison, no preferred orientation was observed for Li_2O.

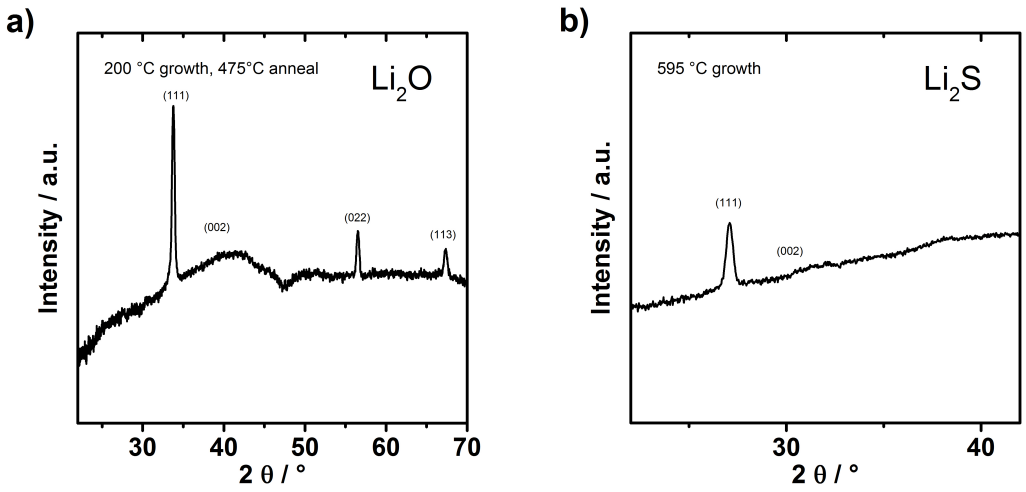

Figure 5.13: XRD patters of a) Li_2O and b) Li_2S films evaporated on MgO at the indicated temperature.

Raman spectroscopy on annealed films revealed no other phases than Li_2S (Figure 5.14). This finding is important because polysulfide content was reported previously when growing Li_2S from ceramic targets at 25 °C;[70] however, in the current study, polysulfides were never observed.

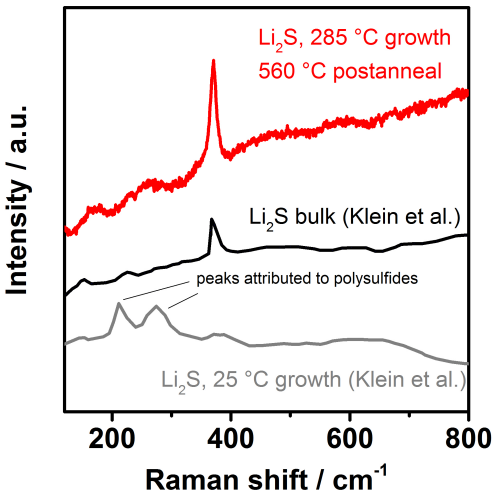

Figure 5.14: Raman spectra acquired from bulk Li_2S (black[70]) and Li_2S evaporated at 285 and postannealed at 560 °C (red, this work) and aputtered at 25 °C (grey[70]).

The melting point of Li_2S is 1372 °C, so growth at 595 °C corresponds to a homologous temperature of 0.65 and at this temperature only modest grain growth and coarsening is expected. Indeed a grain size below 50 nm was estimated from SEM images. Similar grain sizes were obtained for sputtered Li_2S films at much lower growth temperatures, as shown in Figure 5.15.

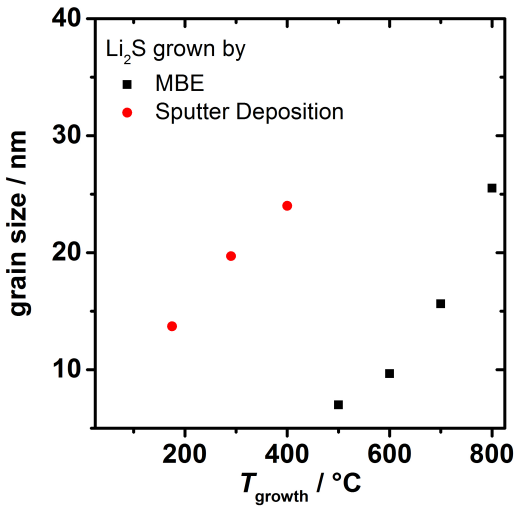

Figure 5.15: Lithium sulfide grain size estimated from SEM image analysis for evaporated and sputter-deposited films at several growth temperatures.

In contrast to the sputter plasma, which provided enough energy for Li and S to react, higher temperatures were required in the MBE since the kinetic energy of effusing lithium is much lower compared to the plasma conditions. For transport measurements presented below, dense, crack-free, sub-50 nm grain size films grown at 610 °C substrate temperature were used.

Lithium selenide

Li_2Se was grown from elemental lithium and selenium on MgO (100) substrates. An optimization of the morphology as a function of temperature is presented in Figure 5.16.

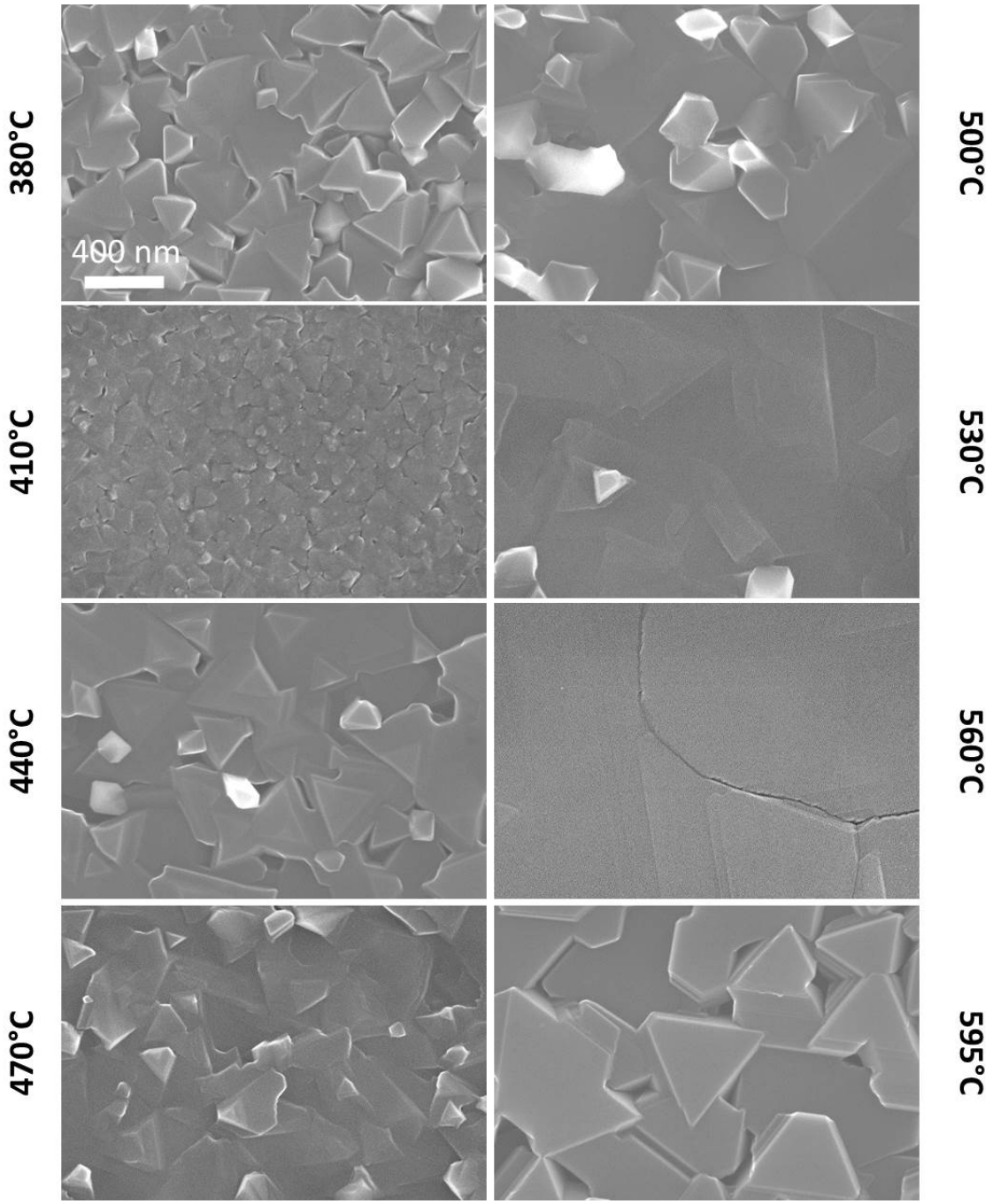

Figure 5.16: Lithium selenide surface morphology of evaporated lithium and selenium onto MgO (100) substrates at several temperatures.

Triangular shaped grains were obtained at all investigated temperatures. The smoothest and most uniform morphology was found between 530 and 560°C. Rougher surfaces are obtained below this temperature range and the films were porous, while above 560 °C grain growth led to porosity. The lattice mismatch between MgO and Li_2Se (1 %) is less pronounced compared to Li_2S (4 %) and Li_2O (9 %).

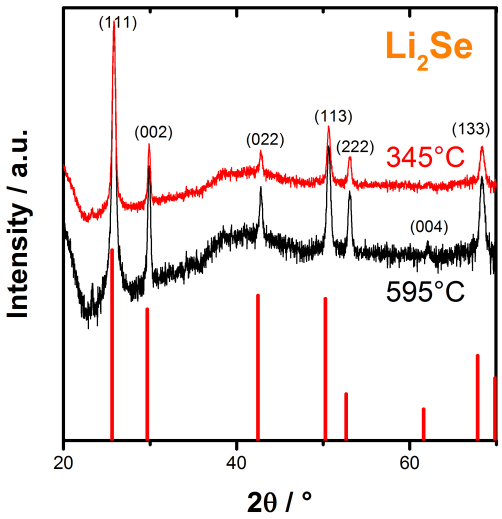

Figure 5.17: XRD patterns obtained from Li_2Se films grown at 345 °C and 595 °C.

Both at low and high temperatures polycrystalline Li_2Se is obtained as shown in Figure 5.17 representative for films grown at 345 and 595 °C. For films grown at 560 °C the resulting cross-section is shown in Figure 5.18.

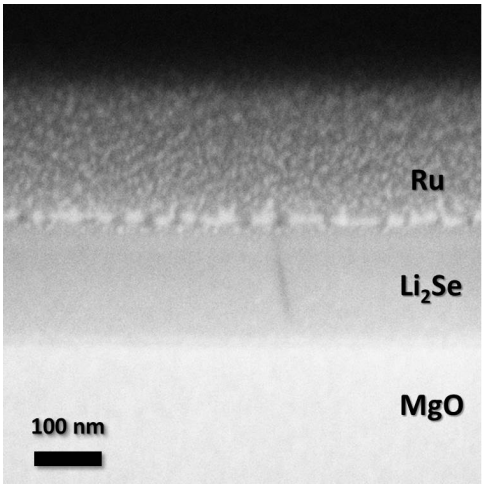

Figure 5.18: A FIB cross-section of a Li_2Se film grown under optimized conditions (MgO (100), 560 °C, Li source at 495 °C, Se source at 135 °C).

Smooth, pore free, polycrystalline films are obtained with grain boundaries between the individual grains.

Bilayers

The growth of bilayers of Li_2O-Li_2S and Li_2S-Li_2Se were also tested. Preliminary results are shown in Figure 5.19.

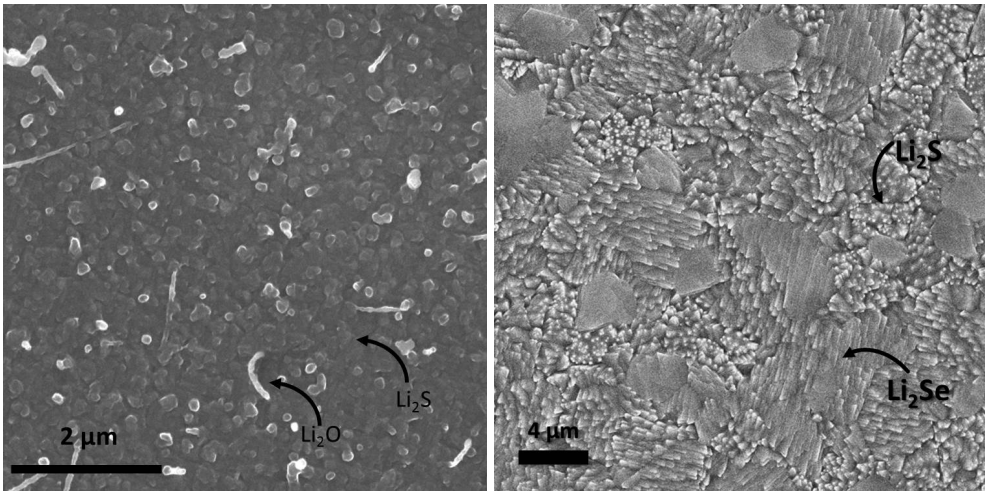

Figure 5.19: SEM images of Li_2O-Li_2S (left) and Li_2S-Li_2Se (right) bilayer morphologies.

Instead of forming two adjacent layers, islands of either polycrystalline Li_2O, Li_2S, or Li_2Se

are obtained. XRD and Raman results presented in Figure 5.20 indicate no reactivity of the two compounds at the synthesis conditions with each other or the substrate and further work is required to optimize the growth of such bilayers or heterolayers.

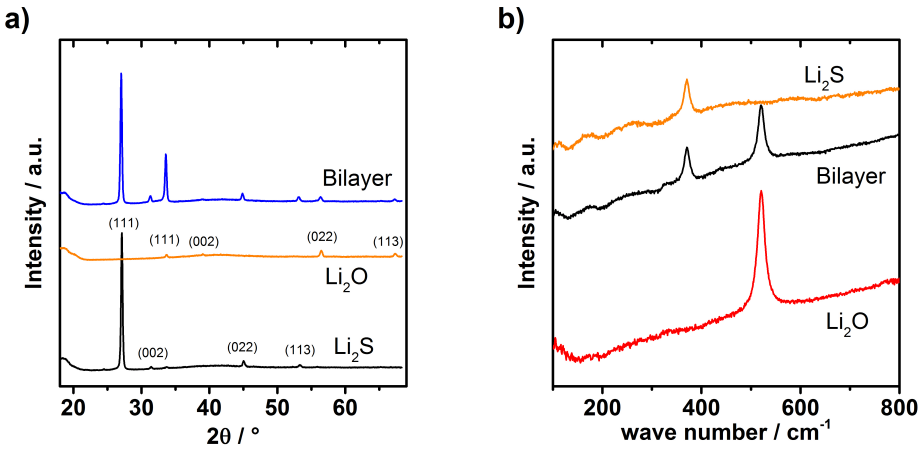

Figure 5.20: a) XRD pattern and b) Raman spectra of Li_2O-Li_2S bilayers.

5.2 Electrochemical analysis

5.2.1 Impedance

The analysis of impedance spectra of polycrystalline samples typically uses a "brick layer" model[142] to deconvolute bulk and grain boundary processes. A typical equivalent circuit is shown in Figure 5.21.[87,88]

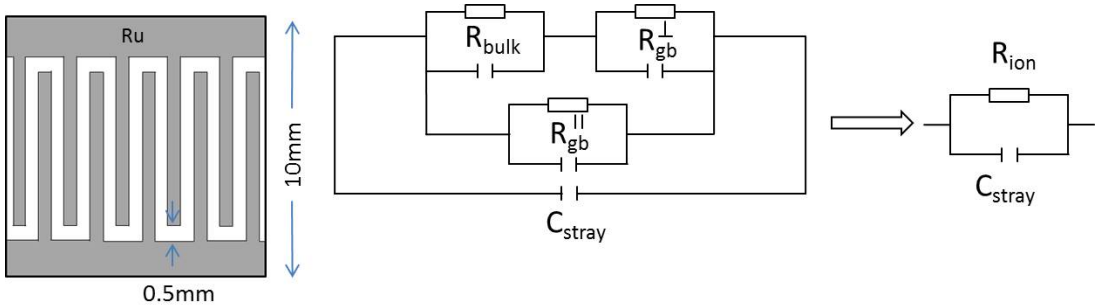

Figure 5.21: Left: Schematic top view of the electrode geometry used for electrical measurements. Right: brick layer model of grain and grain boundary transport. When stray capacitance dominates, the model can be simplified as shown.

To make the resistive films easier to measure near room temperature, interdigitated electrodes were used for measuring the in-plane impedance as shown schematically in Figure 5.21. For all films in this work, the high frequency impedance response was seen to merge into a single semicircle due to stray capacitance, which is on the order of 10^{-12} F. For comparison, in this geometry the bulk capacitance is expected to be far lower - roughly 10^{-16} F, which is not measurable by the impedance setup used. Typical impedance spectra of Li_2O (grown on Al_2O_3) and Li_2S (on MgO) are shown in Figure 5.22.

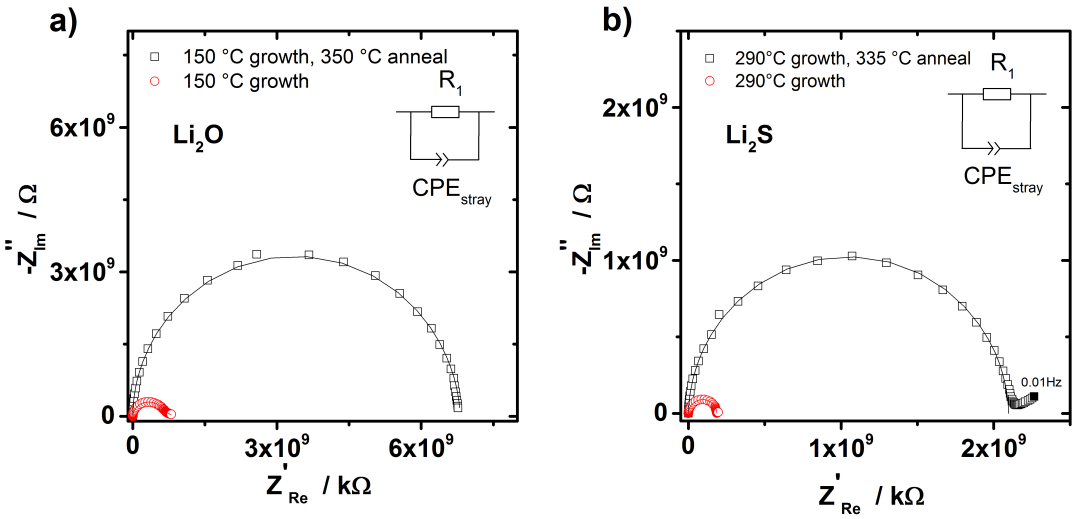

Figure 5.22: a) Typical impedance spectra acquired from sputtered a) Li_2O and b) Li_2S films. Here the films were 460 and 290 nm thick and grown at the indicated temperatures on Al_2O_3 and MgO substrates. Inset shows the equivalent circuit used for fitting the experimental data.

A complete semicircle is measured for the annealed film while for an as-grown film a dispersion at low frequencies is observed. Therefore, the given equivalent circuits are typically condensed into a single R-CPE element, from which the total conductivity was extracted, while the (stray) capacitance was not further analyzed. A diffusive tail is seen at low frequencies and high temperatures due to ion-blocking by the electrodes. Since bulk measurements show that the electronic conductivity is at least two orders of magnitude lower than the ionic conductivity, in thin films the total conductivity was assumed to be entirely due to ions which will be discussed below as well. The resulting ionic conductivity is shown in Figure 5.23. Strikingly, for both materials the conductivity of the as-grown, nominally undoped films is enhanced by more than three orders of magnitude compared to 'undoped' bulk samples.

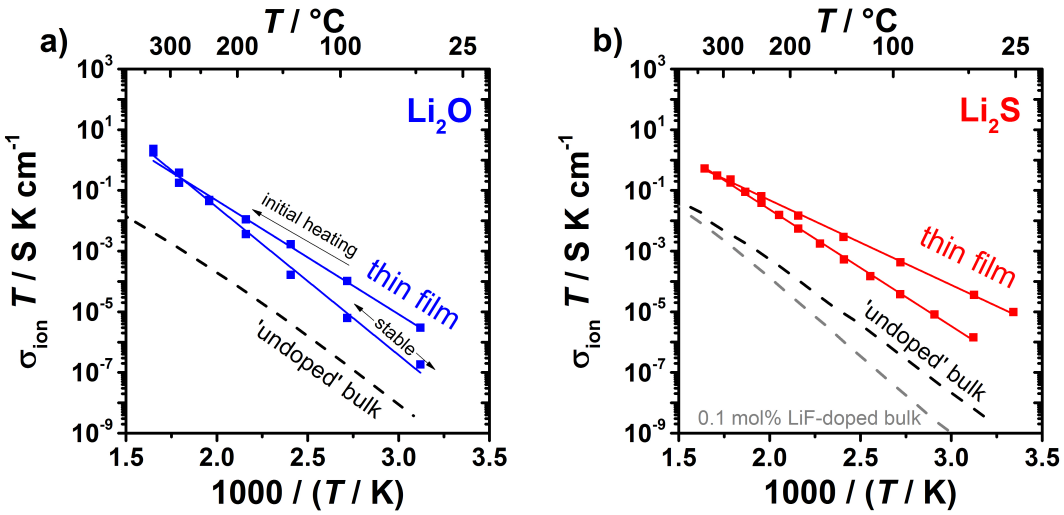

Figure 5.23: Ionic conductivity as a function of inverse temperature for sputtered thin films of a) Li_2O and b) Li_2S compared to bulk data (shown previously in Figure 4.9).

After heating to 350 °C, the enhancement decreases to approximately two orders of magnitude and then remains stable over multiple thermal cycles between 25 and 350 °C. Above 350 °C, severe coarsening of the thin films or reactivity with unstable substrates was observed, leading to porous films and unreliable impedance results. The thermal equilibration temperature was set to 350 °C.

5.2.2 Discussion of enhanced conductivity

One can imagine various mechanisms why thin films would show enhanced transport as indicated in the introduction: the most likely one is a space charge phenomenon at the substrate thin film interface that can cause defect concentrations that are different from the bulk. These can also occur within one material between different grains or between different materials; the preparation of the films could further cause strain or a change in mobile species or the incorporation of impurities. Here, these are considered systematically.

Electronic contribution

The possibility of a non-negligible electronic contribution was tested by comparing results from ion- and electron-blocking electrodes. The results for Li_2O using electron blocking "LICGC" are shown in Figure 5.24. Upon applying a current the voltage quickly reaches a steady value. This behavior indicates predominant ion conduction. As expected, the conductivities obtained by AC and DC measurements show good agreement. Further they agree with results obtained by AC measurements using ion blocking Ru electrodes. Similar results were obtained for Li_2S.

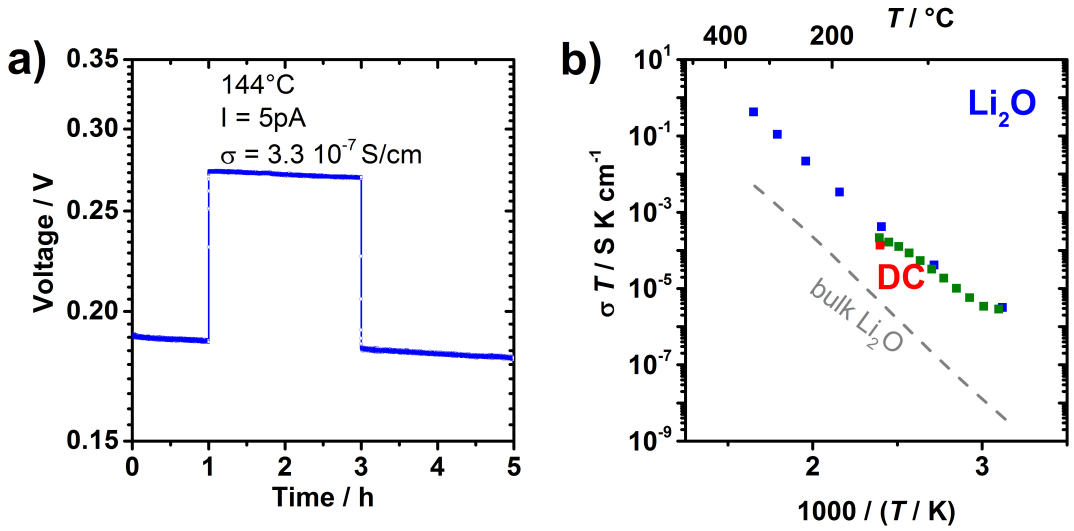

Figure 5.24: a) DC measurement of Li_2O thin films with electron blocking LICGC electrodes. The result obtained matches the AC data plotted in b) from LICGC (green) and Ru (blue) electrodes.

Based on this evidence, dominant electronic contribution in the films is ruled out.

Substrate - film interface

It was shown for LiF thin films sputtered on TiO_2 and Al_2O_3 that the LiF/substrate interface exhibits space charge effects that strongly affect the ionic conductivity near the interface.[85] For Li_2X, a possible interface enhancement was tested, by measuring films of various thicknesses as shown in Figure 5.25. The change in normalized conductance ($\Delta Y^{||}$) at the in-

terface is found by extrapolating the conductivity results of annealed films with various thicknesses to zero thickness.[143] This corresponds to the space charge contribution of the film-substrate interface. The obtained value of $\Delta Y^{\parallel}$ for both Li_2O and Li_2S is quite small. Evidently there is a negligible change in ionic conductivity at the Li_2O/Al_2O_3 and Li_2S/MgO interfaces.

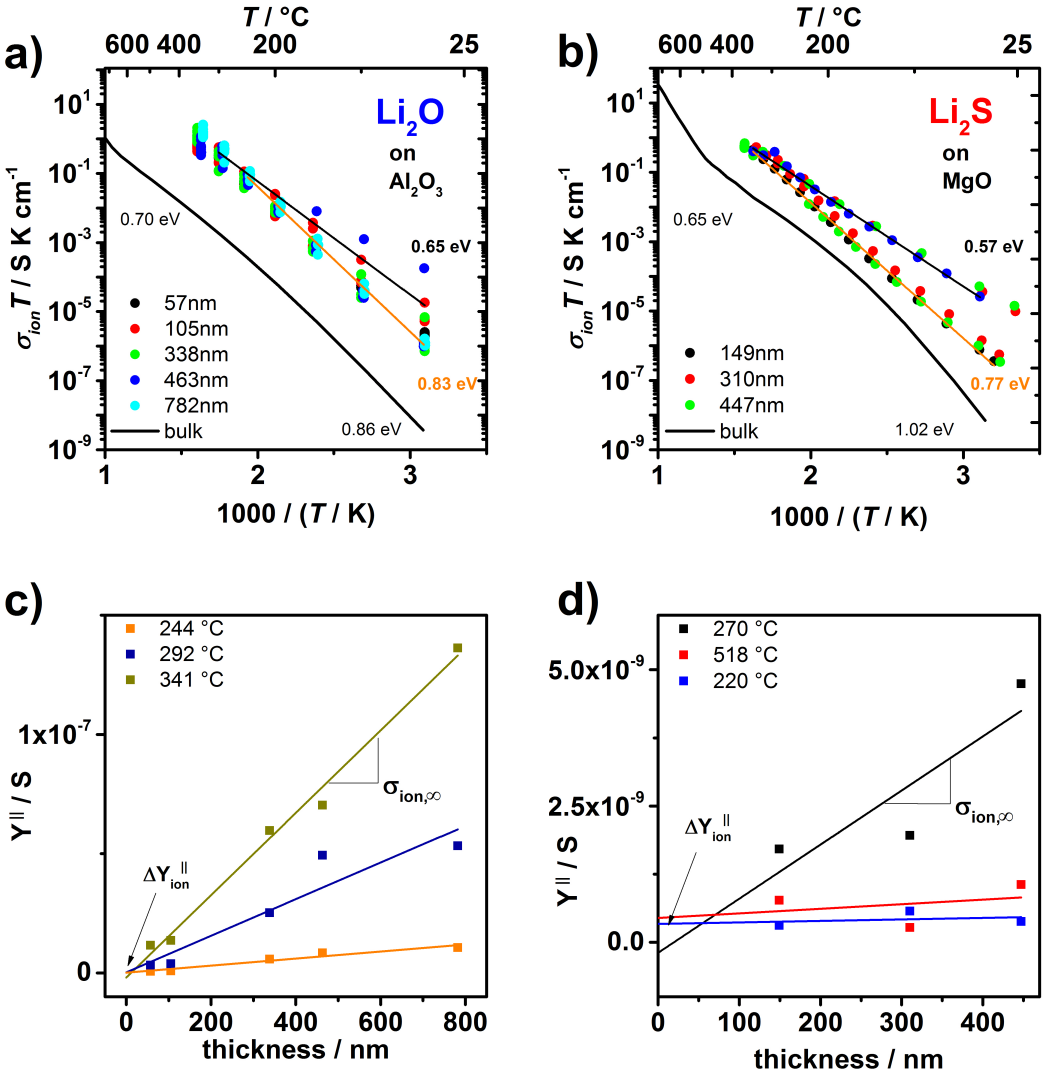

Figure 5.25: Enhanced conductivity of a) Li_2O and b) Li_2S thin films independent of thickness on Al_2O_3 or MgO substrates, respectively. Normalized conductance versus film thickness for c) Li_2O and d) Li_2S.

Other substrate effects

Interface effects caused by the substrate could originate from the formation of unobserved compounds due to reactivity with the substrate, which would be a source of doping. Stray conduction through the substrate rather than the film are an alternative path. A change in film morphology due to different lattice parameters or orientations could also influence the measured conductivity.

To explore those possibilities, other substrates besides Al_2O_3 were tried for Li_2O growth. Figure 5.26 compares the results obtained using MgO, Al_2O_3, LiF, and MgF_2 single crystals as substrates.

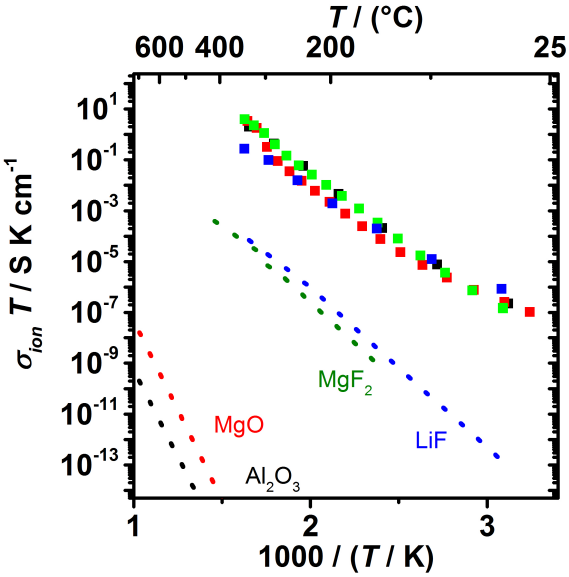

Figure 5.26: Conductivity of sputtered Li_2O on different substrates (points). Substrate conductivities (dashed lines) are also shown in the same color as the Li_2O on top for MgO,[144] Al_2O_3,[145] MgF_2,[146] and LiF.[147]

Roughly the same transport is observed in all cases. These data strongly suggest that the substrate effects listed above are not the underlying source of the enhanced transport.

LiOH formation

Due to the humidity sensitivity, variations in conductivity upon leakage were tested. An intentionally opened impedance cell during the measurement showed a decreased ionic

conductivity as shown in Figure 5.27. The formation of LiOH was assumed, which can not explain the enhancement. However, the conductivity is still higher compared to bulk LiOH for reasons that are unknown.

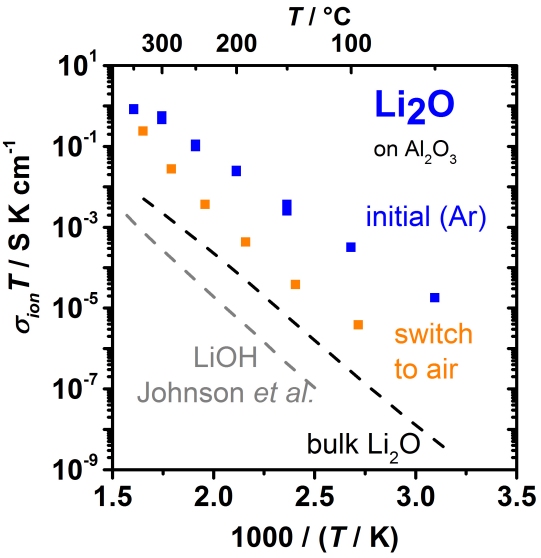

Figure 5.27: Conductivity of sputtered Li_2O exposed to argon in the initial heating and then to air upon heating. Bulk Li_2O and LiOH results are shown as dashed lines for comparison.

Grain boundaries

An alternative explanation for the observed enhancement could be fast grain boundary transport which was reported for CaF_2.[80] By using ball-milling, nanocrystalline CaF_2 was obtained that showed up to 3 orders of magnitude higher transport.

It was observed for Li_2O thin films that grain size increases upon heating as shown in Figure 5.28a) and b). XRD results indicated a change from approximately 30 to 60 nm crystallite size by comparing freshly grown sputtered thin films with 300 °C annealed films. In order to probe if the enhancement seen in the thin films is due to fast transport along the grain boundaries, nanocrystalline Li_2X was prepared.

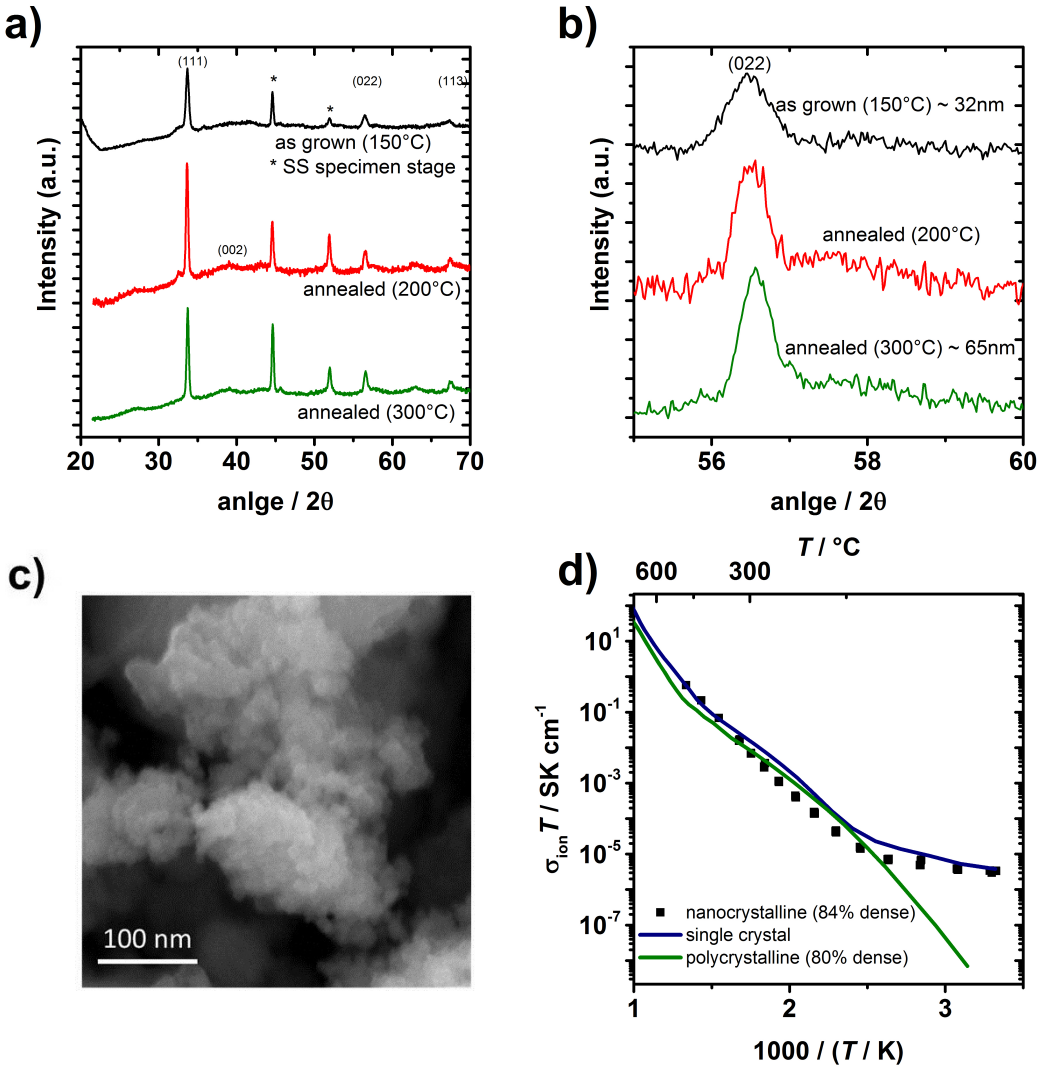

Figure 5.28: Grain boundary characterization in (a, b) Li_2O and (c, d) Li_2S: a) XRD patterns acquired before and after annealing, b) expanded view of a), c) SEM image of nanocrystalline Li_2S powder, d) transport comparison for bulk Li_2S.

For a dense pellet of nanocrystalline Li_2S, the relative grain boundary density is much larger than with macro-sized crystals and a percolating fast grain boundary path should be detectable, when present. Figure 5.28c) shows SEM images from freshly synthesized nano-Li_2S and agglomerates of nanocrystalline powder is obtained. Hot-pressed pellets, however, do not show higher conductivities in impedance measurements compared to bulk or single crystal samples as shown in Figure 5.28d). This result indicates that grain boundaries do not provide a faster grain boundary transport than the bulk. Note that densities do not vary

considerably between sintered microcrystalline and hot-pressed nanocrystalline samples.

A comparison between conductivities obtained from thin film and bulk samples with different grain sizes is shown in Figure 5.29.

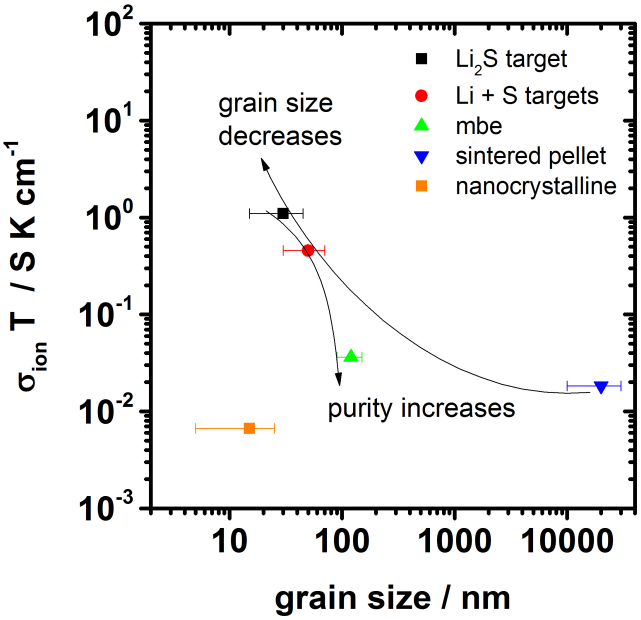

Figure 5.29: Comparison of conductivity obtained from thin films and bulk samples versus grain size of Li_2S.

The grain sizes increase from sputtering to MBE grown films due to a higher processing temperature (from 150 to 290 to 610 °C) and to sintered pellets (900 °C). For nanocrystalline samples the conductivity is still low. Comparing sputter deposition and MBE, the possibility of incorporating impurities decreases due to a much lower process pressure in the mbe, and it is assumed that MBE grown films have much higher purity. According to these findings, the enhanced transport seen in the annealed sputtered thin films is not due to fast grain boundary conductivity but is correlated with impurities incorporated in the films.

Impurities from the sputter target

The thermally stable enhanced conductivity obtained for thin films was found to be independent of sputter method as shown in Figure 5.30. For the initial enhancement different conductivities are obtained, especially for Li_2S thin films from the ceramic target, which showed extreme values. However, once the temperature exceeded the growth temperature, films grown by both methods showed the same stable enhancement in transport over the bulk conductivity.

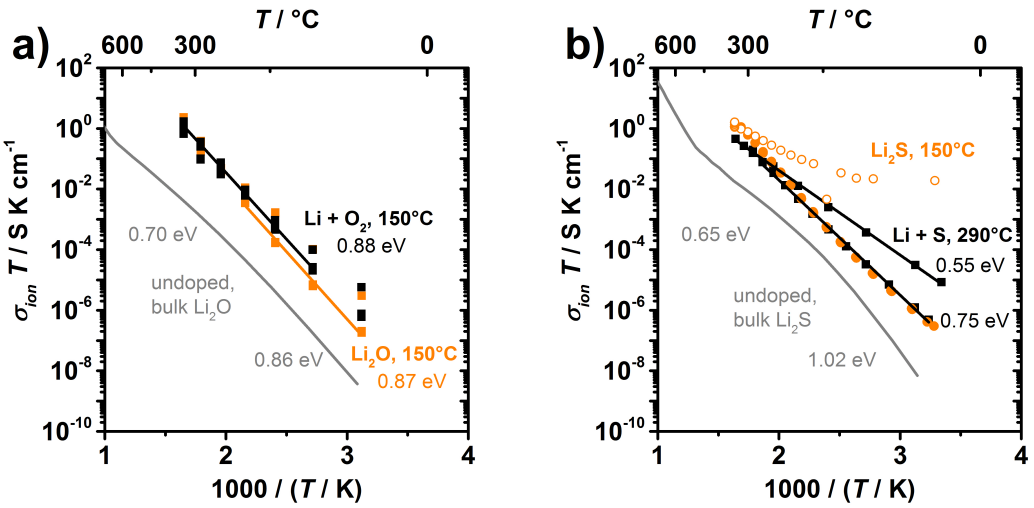

Figure 5.30: Comparison of conductivity data obtained for several growth mechanisms compared to bulk conductivity data for a) Li_2O and b) Li_2S.

The initial enhancement observed for Li_2S (and Li_2O) thin films, single crystals, and nanocrystalline pellets show a different activation energy. For Li_2S thin films 0.55 eV is obtained, which is tentatively attributed to 2D defects, such as dislocations on the surface, or amorphous content from grinding the pellets, or stress causing enhanced lithium vacancy concentrations. This behavior was reported for TiO_2[148] and PbF_2[121] as well.

Compared to the bulk conductivity, the thermally equilibrated thin films show activation energies of 0.87 eV for Li_2O and 0.75 eV for Li_2S. These processes are attributed to the association regime. A tentative explanation of the enhanced transport observed in thin films is based on large doping concentrations that led to association up to 350 °C. Compared to

the bulk conductivity data, positive doping concentrations of approximately 4 mol% are necessary to achieve such high conductivities.

The charge carrier concentration in antifluorite Li_2X was shown above to strongly depend on doping. In order to probe if such high doping concentrations are achievable, several attempts were made to dope bulk samples. The highest measured conductivity for bulk samples (compare Figure 5.31) in Li_2S was found using 1% LiCl, while the solubility limits of metals were typically lower. All tested dopants reached presumably their solubility limit and bulk doping was never sufficient to reach the high conductivities found in Li_2O and Li_2S thin films as shown in Figure 5.31.

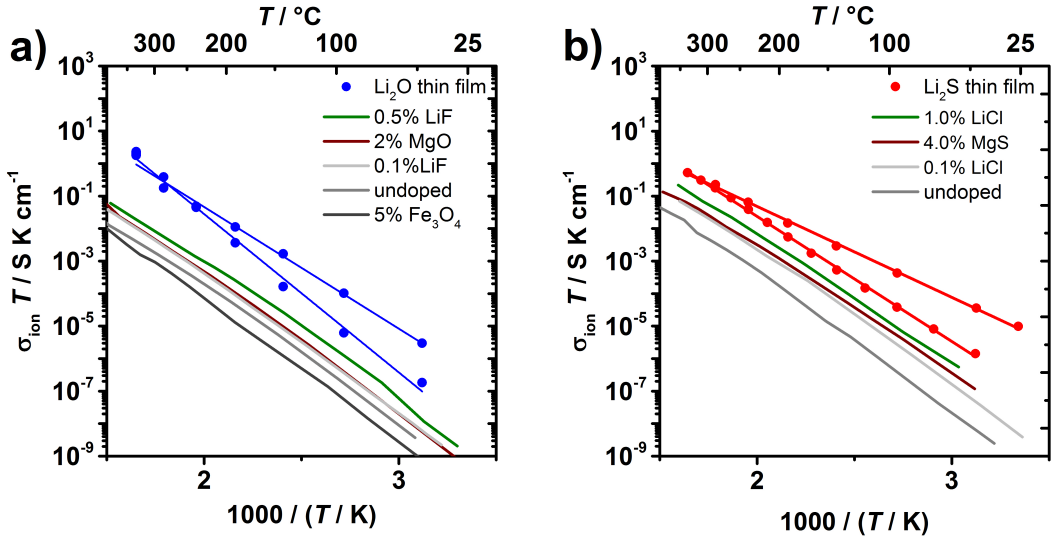

Figure 5.31: Comparison of nominally undoped Li_2O and Li_2S thin films with bulk samples doped with the indicated species and concentrations. For the films, lines are linear fits.

The impurity concentrations in thin films grown on MgO and Al_2O_3 obtained from reactive sputtering were further measured directly. ICP-OES measurements on the dopant concentration in sputtered Li_2O thin films from elemental lithium on Al_2O_3 and MgO, indicate considerable impurity concentrations of B, Al, Ca, Fe, and Ti impurities that in total could account for 1-8 mol%. Due to the very limited thin film mass, these data are considered preliminary.

It was observed in several fluorites, that solid solutions and high doping concentrations

can exist. For single crystal PbF_2 up to 12 mol% Al[149] or 33 mol% KF[150] are soluble and the ionic conductivity is then influenced by cluster formation. In sol-gel prepared CaF_2 up to 40 mol% Y is soluble,[151] while for ball-milling the full solid solution of LaF_3-BaF_2 is possible.[152] Given the overall good agreement between antifluorite and fluorite, it is hypothesized, that up to 4 mol% of yet unknown dopants are incorporated in the Li_2O and Li_2S thin films during sputtering. These are either metastabily incorporated and not reproducible in the bulk, or the right conditions are not yet found to incorporate such high doping concentrations in the bulk.

5.2.3 Transport in MBE films

To test the hypothesis that high doping concentrations are the origin of the enhanced transport, transport in thin films of Li_2O, Li_2S, and Li_2Se grown by evaporation was also measured; Figure 5.32 shows the results.

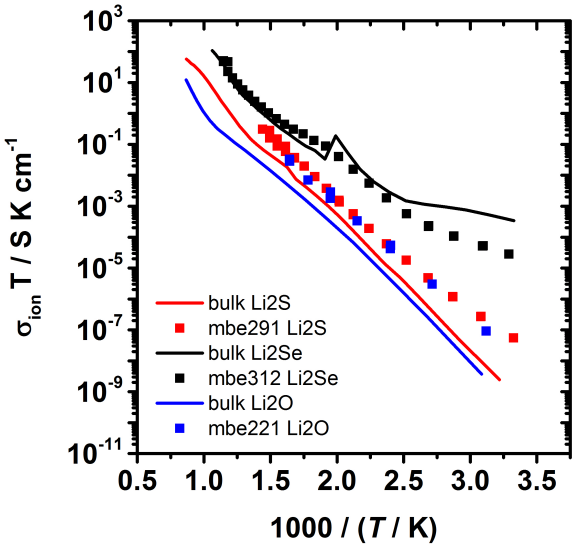

Figure 5.32: Ionic conductivity of Li_2X thin films grown by MBE compared to the nominally undoped bulk values.

The conductivity of Li_2Se thin films is compared to the bulk results as well. The interpretation of bulk Li_2Se in chapter 4 is based on high temperature equilibrated, stable conductivity

measurements. However, these are lower than the data obtained for Li_2Se thin films. The initial conductivity data for both bulk and thin film Li_2Se do however show good agreement. A possible interpretation is, that the initial enhancement seen for both Li_2Se bulk and thin film is attributed to dislocations. Conductivity of bulk samples and thin film values of Li_2Se at elevated temperatures show good agreement. This finding requires further proofs.

For Li_2O, the film was grown at 200 °C and porous. Upon measuring, the roughness increased and the specific conductivity for this sample uses only an averaged thickness. Therefore, this comparison is only preliminary.

The conductivity of evaporated Li_2S thin films is still higher than for the bulk values. In light of the use of SnS_2 as sulfur source, up to 0.5 mol% tin can be expected from XPS measurements as dopant concentration in the films. Indeed, only approximately 0.3 mol% are required for the observed enhancement seen in evaporated Li_2S thin films.

In summary, Li_2X thin films can be prepared both by sputter deposition and evaporation. Sputter deposition leads to high initial conductivities for the freshly grown films. Upon mild annealing at 350 °C, the enhancement has vanished, but a stable conductivity that is still higher than the bulk is obtained. Such high conductivity can be explained by high doping concentrations of approximately 4 mol%. In bulk samples, such high doping concentrations were not yet achieved. In contrast, evaporated thin films show lower conductivities, in agreement with a preparation in an ultrapure environment that leads to lower dopant concentrations. The defect chemistry of bulk and thin film is in good agreement and the implications of the higher observed transport of Li_2X films are discussed in chapter 6.

6 Summary and Outlook

Summary

In this thesis the defect chemistry in both bulk and thin film samples of the lithium chalcogenides has been discussed.

For the bulk, the ion transport behavior in Li_2X was shown to be well described by a defect model based on Frenkel cation disorder. At high temperatures, interstitial lithium ions are more mobile than lithium vacancies in Li_2S, Li_2Se, and Li_2Te; for Li_2O this statement may also be true, but it could not be confirmed (because interstitial-dominated transport was never observed, despite experiments with several plausible dopants). At lower temperatures, lithium vacancies are more mobile. However, they tend to associate with nearest-neighbor positive dopants. In contrast, association of lithium interstitials with (next-nearest-neighbor) negative dopants was never observed. The temperature trends of ionic conductivity were fit and values were extracted for the enthalpies and entropies of Frenkel disorder, vacancy and interstitial migration, and vacancy-dopant association. Excellent agreement was observed between these parameters for Li^+ transport in antifluorite Li_2X and the analogous parameters measured previously for F^- transport in the MF_2 fluorite family of compounds. Furthermore, for both antifluorites and fluorites a larger and more polarizable immobile counterion leads to more favorable intrinsic defect formation energetics and somewhat higher defect mobilities. It was also shown from EMF and Hebb-Wagner measurements that over a wide range of temperatures and activities the electronic transference number remains smaller than 0.01.

Sputtered thin films show an initially high conductivity due to dislocations and other defects. Upon annealing, these are healed and a lower conductivity is obtained, that is

still higher than the bulk conductivities. Scaling from bulk results, an impurity concentration of approximately 4% would be required to cause the stable enhancement observed for sputtered thin films. It is expected that high impurity concentrations are metastably incorporated in these films that were not achieved by bulk doping. High temperature annealing after growth of sputtered films led to coarsening which prohibited the investigation of impurity precipitation. Films grown by MBE are expected to have higher purity and show less enhanced transport (Li_2S) or values close to the bulk (Li_2Se). Films grown by MBE provide better control over morphology and can be grown at higher temperatures with higher purity. These should serve as a base for further investigation of interface transport in Li_2X.

Implications for battery research

Two applications where the defect chemistry of Li_2X plays a critical role are shown below in Figure 6.1.

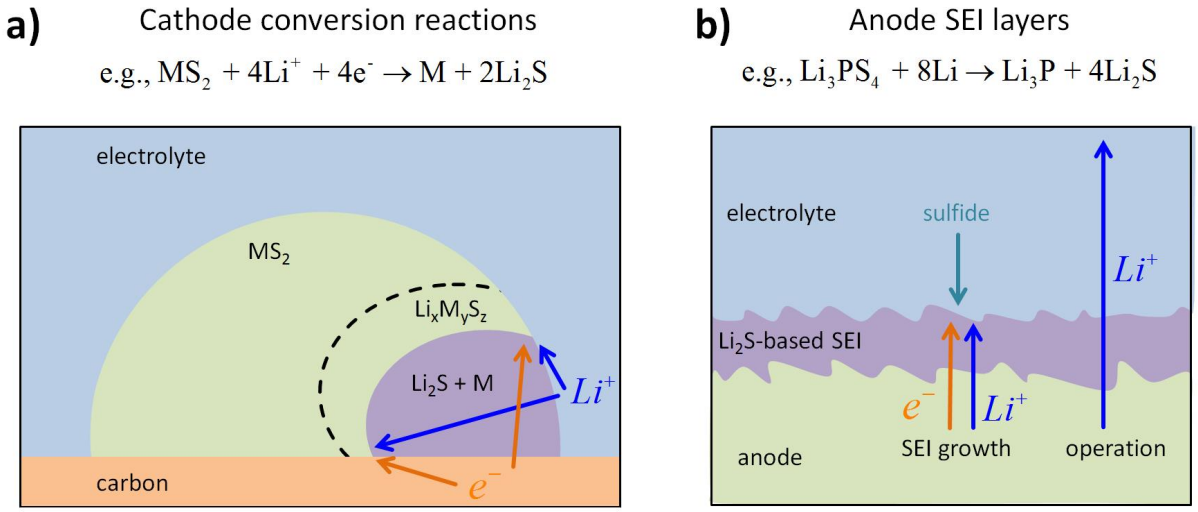

Figure 6.1: Impact of charge carrier chemistry in lithium chalcogenides on battery components of a) cathode conversion reactions and b) anode SEI layers.

In lithium ion battery cathode conversion reactions (Figure 6.1 a), metal chalcogenides are lithiated and converted (through intermediate states) into Li_2X and metallic species. The kinetics of this process are not well-understood, but they clearly depend on charge transport in the individual component phases.[153,154] The results in this thesis therefore

provide a foundation on which any rigorous treatment of such conversion reactions must surely be based.

Figure 6.1b) schematically shows the SEI[155] of a lithium ion battery that forms between low voltage anode and electrolyte due to thermodynamical instability. Here, the lithium conductivity through the SEI would ideally be high, while the electronic conductivity would ideally be low to minimize SEI growth and the associated interfacial resistance and electrolyte consumption.

In this thesis the doping dependence of the ionic conductivity in bulk Li_2X was quantified and found to vary by several orders of magnitude. For example, at 30 °C, the ionic conductivity of Li_2S can range from 10^{-15} to 10^{-11} S/cm. The higher end of this range can be reached by doping with Cl^- or metal ions like Mg^{2+}, while the lower end was observed upon doping with F^- or OH^-. Using the presented defect model, the conductivity can be predicted for any temperature and doping situation that arises. Doping could also be an important tool for manipulating and improving the transport properties of the SEI. For example, one could consider using Li_2X as an artificial SEI. This thesis provides a guide for which dopants would be best (positive dopants like Cl, Mg), which would be poor choices (N), and in which cases it depends (F is a positive dopant for Li_2O but a negative dopant for Li_2S). These doping considerations may also be important for naturally-forming SEI layers. Here a major open question is whether or not dopants dissolved in the electrolyte are transferred and incorporated as dissolved dopants in the SEI component phases. If so, then electrolyte additives could be used to tune not just the SEI component phases but also the doping levels in these phases.

The mentioned dopants are important in lithium-sulfur-batteries since they are present in the *in-situ* formed SEI: due to the sulfide-shuttle mechanism, a major component of the SEI is Li_2S; the standard electrolyte salt, $LiPF_6$, is expected to form a LiF-containing SEI; unavoidable water content in the electrolyte solution results in the formation of LiOH and Li_2O; a conventionally used additive, Li_3NO_4, decomposes during operation to form the highly conducting Li_3N at the SEI; magnesium and other metals may further be present as background impurities. All these components can appear in the forming SEI and are thus important for the overall properties. Even though the above mentioned solubility limits for N, OH, F, and

others in Li_2S are low, they can alter the overall SEI conductivity by orders of magnitude. One needs to know the precise impurity concentrations of the SEI for a description of the conductivity, however, the defect chemical modeling enables the prediction.

These results are also applicable to solid state batteries. For example, the SEI resistances that develop when $Li_{10}GeP_2S_{12}$,[156] Li_6PS_5X (X = Cl, Br, or I),[157] and $Li_7P_3S_{11}$[158] are contacted by Li metal can limit the overall device performance. XPS measurements reveal for $Li_7P_3S_{11}$ that only binary compounds are stable, such as Li_2S and Li_3P, with Li_2S as the major volume fraction.[158] If one considers bulk transport behavior of Li_2S for such an SEI layer, neglecting other effects such as grain boundaries or dislocations, the ionic conductivity is too low to account for the observed SEI resistances. Specifically, transport at 25 °C can be estimated for vacancy- or interstitial-dominated transport in a 10 nm thick Li_2S layer as shown in Figure 6.2. The obtained range of resistances if 10^4-10^8 Ωcm^2, which is higher than the values found for real SEI layers by 1-3 orders of magnitude.

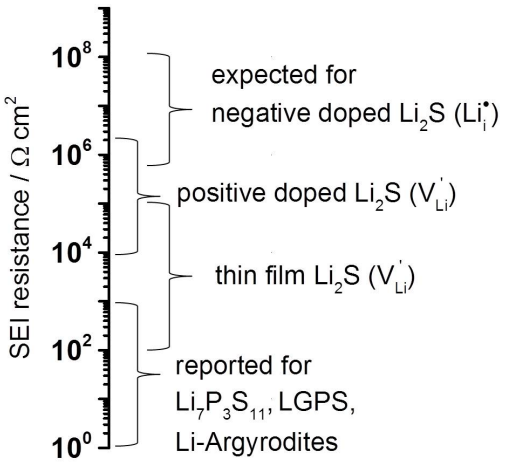

Figure 6.2: Expected SEI resistance for a 10 nm thick Li_2S layer with the indicated defect situation. For comparison, the SEI resistances measured from $Li_{10}GeP_2S_{12}$,[156] Li-Argyrodites of Li_6PS_5X (X = Cl, Br, or I),[157] and $Li_7P_3S_{11}$[158] is also included.

Evidently, an SEI model based on the bulk properties of Li_2S alone is insufficient to explain the behavior in real systems.

The thin film results obtained in this thesis may fill the gap. In particular, dislocations and amorphous content are likely to arise in practice. Dopants that are incorporated metastably

in larger concentrations than feasible in bulk samples have been shown to explain the higher transport in thin films. They are a possible origin of the low resistance found in SEIs forming in real devices, too.

Outlook

In spite of the rather comprehensive knowledge on defect chemistry of the lithium chalcogenides obtained here, a variety of open questions remain.

In light of the analogous behavior of antifluorite and fluorite compounds, several questions arise on properties, that have been observed previously in the fluorite class.

For bulk compounds, interstitial association was observed in alumina-doped PbF_2[149] and one can speculate that this appears for Li_2S below 25 °C as well. The onset of superionic behavior in Li_2Te was reported as preliminary result in this work and it seems plausible compared to the behavior found for PbF_2.[123] However, several experimental difficulties exist for the investigation of superionic behavior by impedance spectroscopy, such as reactivity with the electrodes[159] or high conductivity that has to be deconvoluted from inductive effects. The precise measurement of the electronic minority conductivity is still lacking due to the discussed difficulties. For Hebb-Wagner measurements, a combination of low temperatures, avoiding surface diffusion of lithium, and microelectrodes in an high purity environment with good electronic shielding, and transfer without exposure to air is necessary to measure the very low electronic conductivity in Li_2X. Alternatively, high temperature transport measurements under defined chalcogen gas pressures could be used to investigate minority carrier transport if the reactivity with the electrodes can be resolved and sealing is provided.

For thin films, enhanced transport at Li_2O-Li_2S or Li_2S-Li_2Se can be hypothesized in comparison to the space charge effects observed for CaF_2-BaF_2. However, several requirements have to be fulfilled for the investigation of analogous behavior. Both CaF_2 and BaF_2 could be grown epitaxially. The issue of substrate stability during growth of Li_2X hinders the choice of lattice matched substrates and epitaxial growth was not obtained in this work. Buffer layers of thermodynamically stable compounds such as alkali-halides could overcome this problem. The rather high temperatures used to obtain good film quality in this work could

thereby be reduced, depending on growth conditions for epitaxial growth. This could further help with growing bilayers, since preliminary experiments indicate intermixing of Li_2S and Li_2Se at the high temperatures used. The thin film growth is further complicated by the use of the SnS_2 source that provides sulfur in the MBE. It was shown by XPS that Sn is a plausible impurity in Li_2S thin films, which could be avoided by using a different effusion technique.

Acknowledgments

I would like to thank Professor Joachim Maier for the opportunity to work in his group and his supervision. All the fruitful discussions and his feedback on talks, writing, and experiments throughout the last years were very valuable to me.

I would also like to thank Professor Thomas Schleid and Professor Frank Gießelmann for being part of my examination committee.

I am very grateful to Dr. Robert Usiskin for all his teaching and supervision on a daily basis: the willingness to share his expertise, his patience in proof-reading, and motivating attitude helped me enormously.

The group of Physical Chemistry of Solids really makes working at the institute enjoyable: Special thanks go to Sofia Weiglein, who was great support since the beginning. I would like to thank Dr. Rotraut Merkle for fruitful discussion and experimental guidance in the lab. Thanks to our technical team: Armin Sorg and Florian Kaiser for all things related to numerous hours of repairing thin film equipment, Dr. Helga Hoier for her collaboration and guidance with our XRD equipment, Uwe Traub, Udo Klock, Annette Fuchs, and Babara Reichert for all the help they offered. Many thanks go to my fellow PhD students and those who helped initially such as Federico, Chia-Chin, and Jan and more recently to Max H., Max S., Markus, Kyungmi, Alessandro, Maryam, Reihaneh, and especially to my office members Torben and Andreas who always had time to chat about the ups and downs during the time at the institute.

All the support I shared at the institute is greatly acknowledged: thanks go to the technology group, Dr. Dieter Fischer for collaborating with his XRD equipment, Bernhard Fenk for many hours of FIB/SEM preparation.

Last but not least, I am deeply thankful to my family and Nina, who supported me in every aspect, motivated, and accompanied me during the PhD time.

List of Symbols and Abbrevations

$\Delta_A H^\circ$ ..... Standard Enthalpy of Association

$\Delta_A S^\circ$ ..... Standard Entropy of Association

$\Delta_F H^\circ$ ..... Standard Frenkel Formation Enthalpy

$\Delta_F S^\circ$ ..... Standard Frenkel Formation Entropy

$\Delta_m H$ ..... Enthalpy of Migration

$\Delta_m S$ ..... Entropy of Migration

ϵ_0 ..... Vacuum Permitivity, $8.854 \cdot 10^{-12}$ F m^{-1}

ϵ_R ..... Dielectric Constant

ν_0 ..... Jump Attempt Frequency

ω ..... Phase Change

σ_{eon} ..... Electronic Conductivity

σ_{ion} ..... Ionic Conductivity

A ..... Specimen Area

a_0 ..... Unit Cell Dimension

a_{Li} ..... Lithium Activity

d ..... Specimen Thickness

E ..... Electric Field

e ..... Elementary Charge

fcc ..... Face Centered Cubic

J ..... Current Density

j ..... Imaginary Unit

K_A ..... Association Constant

k_B ..... Boltzmann Constant

K_F ..... Frenkel Constant

L ..... Specimen Length

N_k ..... Site Concentration on Site k

p_{O_2} ..... Oxygen Partial Pressure

Q ..... Constant Phase Element Magnitude

R ..... Resistance

r_k ..... Distance between sites in a unit cell

R_{spr} ..... Spreading Resistance

T ..... Temperature

t_{ion} ..... Ionic Transference Number

u_k ..... Mobility of species k

V_{Nernst} ..... Nernst Voltage

Z ..... Impedance

z_k ..... Charge of species k

AC ..... Alternating Current

CPE ..... Constant Phase Element

DC ..... Direct Current

DFT ..... Density Functional Theory

EIS ..... Electrochemical Impedance Spectroscopy

EMF ..... Electromotive Force

F-centers ..... Color Center

FIB ..... Focused Ion Beam

ICP-OES ..... Inductively Coupled Plasma Optical Emission Spectroscopy

LGPS ..... $Li_{10}GeP_2S_{12}$

MBE ..... Molecular Beam Epitaxy

NMR ..... Nuclear Magnetic Resonance

OCV ..... Open Circuit Voltage

SEI ..... Solid Electrolyte Interface

SEM ..... Scanning Electron Microscopy

THF ..... Tetrahydrofuran

XPS ..... X-ray Photoelectron Spectroscopy

XRD ..... X-ray Diffraction

List of References

[1] J. Maier, *Angewandte Chemie - International Edition* **2013**, *52*(19), 4998–5026.

[2] P. G. Bruce, S. A. Freunberger, L. J. Hardwick, J.-M. Tarascon, *Nature Materials* **2012**, *11*(1), 19–29.

[3] L. F. Nazar, M. Cuisinier, Q. Pang, *MRS Bulletin* **2014**, *39*(05), 436–442.

[4] C. Xia, C. Y. Kwok, L. F. Nazar, *Science* **2018**, *361*(6404), 777–781.

[5] T. Ogasawara, A. Débart, M. Holzapfel, P. Novák, P. G. Bruce, *Journal of the American Chemical Society* **2006**, *128*(4), 1390–1393.

[6] J. He, W. Lv, Y. Chen, K. Wen, C. Xu, W. Zhang, Y. Li, W. Qin, W. He, *ACS Nano* **2017**, *11*(8), 8144–8152.

[7] F. Wu, J. T. Lee, Y. Xiao, G. Yushin, *Nano Energy* **2016**, *27*, 238–246.

[8] A. Donato, *Fusion Engineering and Design* **1998**, *38*(4), 369–392.

[9] B. Bertheville, H. Bill, H. Hagemann, *Journal of Physics: Condensed Matter* **1998**, *10*(9), 2155–2169.

[10] M. Mousa, Y. S. Oei, H. Richtering, *Journal de Physique* **1980**, *41*(C6), C6–223 – C6–226.

[11] B. Bertheville, D. Low, H. Bill, F. Kubel, *Journal of Physics and Chemistry of Solids* **1997**, *58*(10), 1569–1577.

[12] A. V. Chadwick, K. W. Flack, J. H. Strange, J. Harding, *Solid State Ionics* **1988**, *28*, 185–188.

[13] N. Sata, K. Eberman, K. Eberl, J. Maier, *Nature* **2000**, *408*(6815), 946–949.

[14] E. Zintl, A. Harder, B. Dauth, *Zeitschrift fuer Elektrochemie und Angewandte Physikalische Chemie* **1934**, *8*, 588–593.

[15] A. Grzechnik, A. Vegas, K. Syassen, I. Loa, M. Hanfland, M. Jansen, *Journal of Solid State Chemistry* **2000**, *154*(2), 603–611.

[16] P. Goel, N. Choudhury, S. L. Chaplot, *Journal of Physics: Condensed Matter* **2007**, *19*(38), 386239–1–8.

[17] A. Lazicki, C. S. Yoo, W. J. Evans, W. E. Pickett, *Physical Review B - Condensed Matter and Materials Physics* **2006**, *73*(18), 1–7.

[18] R. D. Shannon, *Acta Crystallographica Section A* **1976**, *32*(5), 751–767.

[19] F. Kubel, B. Bertheville, H. Bill, *Zeitschrift fuer Kristallographie - New Crystal Structures* **1999**, *214*(3), 302.

[20] H. Okamoto, *Journal of Phase Equilibria and Diffusion* **2013**, *34*(2), 169.

[21] P. T. Cunningham, S. A. Johnson, E. J. Cairns, *Journal of The Electrochemical Society* **1972**, *119*(11), 1448.

[22] J. Sangster, A. D. Pelton, *Journal of Phase Equilibria* **1997**, *18*(2), 181–184.

[23] J. Sangster, A. D. Pelton, *Journal of Phase Equilibria* **1992**, *13*(3), 300–303.

[24] O. Gerbig, R. Merkle, J. Maier, *Advanced Materials* **2013**, *25*(22), 3129–3133.

[25] J. Lu, Y. J. Lee, X. Luo, K. C. Lau, M. Asadi, H. H. Wang, S. Brombosz, J. Wen, D. Zhai, Z. Chen, D. J. Miller, Y. S. Jeong, J. B. Park, Z. Z. Fang, B. Kumar, A. Salehi-Khojin, Y. K. Sun, L. A. Curtiss, K. Amine, *Nature* **2016**, *529*(7586), 377–382.

[26] Y. Asaoka, H. Moriyama, K. Iwasaki, K. Moritani, Y. Ito, *Journal of Nuclear Materials* **1991**, *183*(3), 174–179.

[27] M. W. Chase, *NIST-JANAF Thermochemical Tables*, **1998**.

[28] R. Rauh, F. Shuker, J. Marston, S. Brummer, *Journal of Inorganic and Nuclear Chemistry* **1977**, *39*(10), 1761–1766.

[29] F. W. Bergstrom, *Journal of the American Chemical Society* **1926**, *48*(1), 146–151.

[30] J. Conder, R. Bouchet, S. Trabesinger, C. Marino, L. Gubler, C. Villevieille, *Nature Energy* **2017**, *2*, 1–7.

[31] K. Atobe, *physica status solidi (a)* **1982**, *71*(1), K25–K28.

[32] E. Kotomin, A. Popov, *Nuclear Instruments and Methods in Physics Research Section B: Beam Interactions with Materials and Atoms* **1998**, *141*(1-4), 1–15.

[33] J. M. Baker, A. Cox, A. J. O'Connell, R. C. C. Ward, *Journal of Physics: Condensed Matter* **1991**, *3*(32), 6189–6193.

[34] H. Ohno, S. Konishi, T. Nagasaki, T. Kurasawa, H. Katsuta, H. Watanabe, *Journal of Nuclear Materials* **1985**, *133-134*(C), 181–185.

[35] Y. Oishi, Y. Kamei, M. Akiyama, T. Yanagi, *Journal of Nuclear Materials* **1979**, *87*(2-3), 341–344.

[36] M. Akiyama, K. Ando, Y. Oishi, *Journal of Nuclear Science and Technology* **1980**, *17*(2), 154–155.

[37] M. Akiyama, K. Ando, Y. Oishi, *Solid State Ionics* **1981**, *3-4*(C), 469–472.

[38] I. Shindo, S. Kimura, K. Noda, T. Kurasawa, S. Nasu, *Journal of Nuclear Materials* **1979**, *79*(2), 418–419.

[39] Y. S. Oei, H. Richtering, *Berichte der Bunsengesellschaft für physikalische Chemie* **1976**, *80*(10), 1007–1017.

[40] Z. H. Xie, M. E. Smith, J. H. Strange, C. Jaeger, *Journal of Physics: Condensed Matter* **1995**, *7*(12), 2479–2487.

[41] R. A. Huggins, *Electrochimica Acta* **1977**, *22*(7), 773–781.

[42] R. M. Biefeld, R. T. Johnson, *Journal of The Electrochemical Society* **1979**, *126*(1), 1–6.

[43] T. Matsuo, H. Ohno, K. Noda, S. Konishi, H. Yoshida, H. Watanabe, *Journal of the Chemical Society, Faraday Transactions 2* **1983**, *79*(8), 1205–1216.

[44] S. Konishi, H. Ohno, *Journal of Nuclear Materials* **1988**, *152*(1), 9–13.

[45] S. Indris, P. Heitjans, H. E. Roman, A. Bunde, *Physical Review Letters* **2000**, *84*(13), 2889–2892.

[46] J. H. Strange, S. M. Rageb, a. V. Chadwick, K. W. Flack, J. H. Harding, *Journal of the Chemical Society, Faraday Transactions* **1990**, *86*(8), 1239.

[47] J. H. Strange, Z. H. Xie, *Journal of Non-Crystalline Solids* **1994**, *174*, 1262–1269.

[48] A. Annamareddy, J. Eapen, *Entropy* **2017**, *19*(5), 1–11.

[49] A. D. Mulliner, P. C. Aeberhard, P. D. Battle, W. I. David, K. Refson, *Physical Chemistry Chemical Physics* **2015**, *17*(33), 21470–21475.

[50] R. M. Fracchia, G. D. Barrera, N. L. Allan, T. H. Barron, W. C. Mackrodt, *Journal of Physics and Chemistry of Solids* **1998**, *59*(3), 435–445.

[51] P. Goel, N. Choudhury, S. L. Chaplot, *Physical Review B - Condensed Matter and Materials Physics* **2004**, *70*(17), 1–8.

[52] T. W. D. Farley, W. Hayes, S. Hull, M. T. Hutchings, M. Vrtis, *Journal of Physics: Condensed Matter* **1991**, *3*, 4761–4781.

[53] M. Hayoun, M. Meyer, A. Denieport, *Acta Materialia* **2005**, *53*(10), 2867–2874.

[54] M. Hayoun, M. Meyer, *Acta Materialia* **2008**, *56*(6), 1366–1373.

[55] M. Hayoun, M. Meyer, *Surface Science* **2013**, *607*, 118–123.

[56] Z. Lin, Z. Liu, N. J. Dudney, C. Liang, *ACS Nano* **2013**, *7*(3), 2829–2833.

[57] B. Schoch, E. Hartmann, W. Weppner, *Solid State Ionics* **1986**, *18-19*, 529–533.

[58] F. Altorfer, W. Buehrer, I. Anderson, O. Schaerpf, H. Bill, P. Carron, H. Smith, *Physica B: Condensed Matter* **1992**, *180-181*, 795–797.

[59] P. M. Mjwara, J. D. Comins, P. E. Ngoepe, W. Buehrer, H. Bill, *Journal of Physics: Condensed Matter* **1991**, *3*(23), 4289–4292.

[60] W. Buehrer, F. Altorfer, J. Mesot, H. Bill, P. Carron, H. G. Smith, *Journal of Physics: Condensed Matter* **1991**, *3*(9), 1055–1064.

[61] F. Altorfer, W. Buehrer, I. Anderson, O. Schaerpf, H. Bill, P. L. Carron, *Journal of Physics: Condensed Matter* **1994**, *6*(46), 9937–9947.

[62] A. Moradabadi, P. Kaghazchi, *Applied Physics Letters* **2016**, *108*(21), 213906–1–4.

[63] B. S. D.-H. Kim, M. S. B. Lee, K.-Y. Park, K. Kang, *Chemistry - An Asian Journal* **2016**, *11*(8), 1288–1292.

[64] S. P. Jand, Q. Zhang, P. Kaghazchi, *Scientific Reports* **2017**, *7*(1), 2–7.

[65] J. Schneider, T. Schröder, M. Hoelzel, O. Kluge, W. W. Schmahl, O. Oeckler, *Solid State Ionics* **2018**, *325*, 90–101.

[66] H. Kikuchi, H. Iyetomi, A. Hasegawa, *Journal of Physics Condensed Matter* **1998**, *10*(49), 11439–11448.

[67] N. Dudney, *Solid State Ionics* **1992**, *53-56*, 655–661.

[68] N. J. Dudney, J. B. Bates, J. D. Robertson, *Journal of Vacuum Science & Technology A: Vacuum, Surfaces, and Films* **1993**, *11*(2), 377–389.

[69] X. Meng, D. J. Comstock, T. T. Fister, J. W. Elam, *ACS Nano* **2014**, *8*(10), 10963–10972.

[70] M. J. Klein, G. M. Veith, A. Manthiram, *Journal of the American Chemical Society* **2017**, *139*(31), 10669–10676.

[71] Y. Ito, K. Miyauchi, T. Oi, *Journal of Non-Crystalline Solids* **1983**, *57*(3), 389–400.

[72] T. Aaltonen, O. Nilsen, A. Magrasó, H. Fjellvåg, *Chemistry of Materials* **2011**, *23*(21), 4669–4675.

[73] H. Akazawa, *Thin Solid Films* **2014**, *556*, 74–80.

[74] M. B. Tellekamp, J. C. Shank, W. A. Doolittle, *Journal of Crystal Growth* **2017**, *463*, 156–161.

[75] J. C. Shank, M. Brooks Tellekamp, W. Alan Doolittle, *Thin Solid Films* **2016**, *609*, 6–11.

[76] X. Guo, I. Matei, J. Jamnik, J. S. Lee, J. Maier, *Physical Review B - Condensed Matter and Materials Physics* **2007**, *76*(12), 1–7.

[77] X. Guo, J. Maier, *Advanced Functional Materials* **2009**, *19*(1), 96–101.

[78] B. Ruprecht, M. Wilkening, S. Steuernagel, P. Heitjans, *Journal of Materials Chemistry* **2008**, *18*(44), 5412–5416.

[79] J. Maier, *Progress in Solid State Chemistry* **1995**, *23*(3), 171–263.

[80] W. Puin, S. Rodewald, R. Ramlau, P. Heitjans, J. Maier, *Solid State Ionics* **2000**, *131*(1), 159–164.

[81] Y. Saito, J. Maier, *Solid State Ionics* **1996**, *86-88*, 581–584.

[82] Y. Saito, J. Maier, *Journal of The Electrochemical Society* **1995**, *142*(9), 3078–3083.

[83] C. C. Liang, *Journal of The Electrochemical Society* **1973**, *120*(10), 1289.

[84] E. Schreck, K. Läuger, K. Dransfeld, *Zeitschrift für Physik B Condensed Matter* **1986**, *62*(3), 331–334.

[85] C. Li, J. Maier, *Solid State Ionics* **2012**, *225*, 408–411.

[86] U. Lauer, J. Maier, *Solid State Ionics* **1992**, *51*, 209–213.

[87] J. Fleig, J. Maier, *Physical Chemistry Chemical Physics* **1999**, *1*(1), 3315–3320.

[88] J. Fleig, S. Rodewald, J. Maier, *Solid State Ionics* **2000**, *136-137*, 905–911.

[89] A. B. Lidiard, *Handbuch der Physik*, Bd. 111, Springer, **1957**, S. 246–349.

[90] J. Maier, *Physical Chemistry of Ionic Materials: Ions and Electrons in Solids*, John Wiley & Sons, Inc., **2004**.

[91] F. Kroeger, *The Chemistry of Imperfect Crystals*, John Wiley & Sons, Inc., **1964**.

[92] H. Rickert, *Einführung in die Elektrochemie fester Stoffe*, Bd. 106, Springer, Berlin, Heidelberg, **1973**, S. 1323–1330.

[93] W. Bollmann, *Physica Status Solidi (a)* **1974**, *24*(1), 181–190.

[94] W. Bollmann, P. Goerlich, W. Hauk, H. Mothes, *Physica Status Solidi A* **1970**, *2*, 157–170.

[95] T. G. Stoebe, R. A. Huggins, *Journal of Materials Science* **1966**, *1*(2), 117–126.

[96] K. C. Kao, L. J. Giles, J. H. Calderwood, *Journal of Applied Physics* **1968**, *39*(8), 3955–3961.

[97] R. W. Dreyfus, A. S. Nowick, *Physical Review* **1962**, *126*(4), 1367–1377.

[98] S. Nasu, H. Takeshita, *Journal of Nuclear Materials* **1978**, *75*(1), 110–114.

[99] W. Rauch, *Zeitschrift für Physik* **1939**, *111*(9-10), 650–656.

[100] Y. Ishii, J.-i. Murakami, M. Itoh, *Journal of the Physical Society of Japan* **1999**, *68*(2), 696–697.

[101] L. Liu, V. E. Henrich, W. P. Ellis, I. Shindo, *Phys. Rev. B* **1996**, *54*(3), 2236–2239.

[102] R. D. Eithiraj, G. Jaiganesh, G. Kalpana, M. Rajagopalan, *Physica Status Solidi (B) Basic Research* **2007**, *244*(4), 1337–1346.

[103] Y. Malozovsky, L. Franklin, C. Ekuma, D. Bagayoko, *International Journal of Modern Physics B* **2015**, *29*, 1542006.

[104] H. Park, H. S. Koh, D. J. Siegel, *Journal of Physical Chemistry C* **2015**, *119*(9), 4675–4683.

[105] P. Pandit, B. Rakshit, S. P. Sanyal, *Indian Journal of Pure & Applied Physics* **2009**, *47*, 804–807.

[106] S. M. Alay-E-Abbas, N. Sabir, Y. Saeed, A. Shaukat, *Journal of Alloys and Compounds* **2010**, *503*(1), 10–18.

[107] B. Bahloul, L. Amirouche, A. Dekhira, A. Bentabet, *Computational Materials Science* **2014**, *86*, 49–56.

[108] Y. Wang, F. Tian, D. Li, D. Duan, Y. Liu, B. Liu, Q. Zhou, T. Cui, *Materials Research Express* **2017**, *4*, 015701.

[109] H. Mehrer, *Diffusion in Solids*, Bd. 155 von *Springer Series in Solid-State Sciences*, Springer, **2007**, S. 601.

[110] R. W. Bonne, J. Schoonman, *Journal of The Electrochemical Society* **1977**, *124*(1), 28 – 35.

[111] F. Fong, *Progress in Solid State Chemistry* **1967**, *3*, 135–212.

[112] H. Eyring, *The Journal of Chemical Physics* **1935**, *3*(2), 107–115.

[113] J. Maier, *Modern Aspects Of Electrochemistry*, Bd. 41, **2007**.

[114] M. E. Orazem, B. Tribollet, *Electrochemical Impedance Spectroscopy*, John Wiley & Sons, Inc., **2008**.

[115] E. Barsoukov, J. R. Macdonald, *Impedance Spectroscopy: Theory, Experiment, and Applications, 2nd Edition*, John Wiley & Sons, Inc., **2005**.

[116] C. Wagner, *Proceedings of the 7th Meeting of the International Committee on Electrochemical Thermodynamics and Kinetics* **1955**, 361 – 377.

[117] X. Guo, J. Maier, *Solid State Ionics* **2000**, *130*, 267–280.

[118] W. Weppner, R. Huggins, *Journal of The Electrochemical Society* **1978**, *125*(1), 7–14.

[119] C. J. Wen, B. Boukamp, R. Huggins, W. Weppner, *Journal of The Electrochemical Society* **1979**, *126*(12), 2258–2266.

[120] S. T. Pantelides, *Physical Review Letters* **1975**, *35*(4), 250–254.

[121] A. V. Joshi, *Journal of The Electrochemical Society* **1977**, *124*(8), 1253.

[122] C. Zhan, Z. Yao, J. Lu, L. Ma, V. A. Maroni, L. Li, E. Lee, E. E. Alp, T. Wu, J. Wen, Y. Ren, C. Johnson, M. M. Thackeray, M. K. Y. Chan, C. Wolverton, K. Amine, *Nature Energy* **2017**, *2*(12), 963–971.

[123] C. E. Derrington, M. O'Keeffe, *Nature Physical Science* **1973**, *246*(151), 44–46.

[124] W. Bollmann, *Physica Status Solidi A* **1973**, *18*, 313–321.

[125] W. Bollmann, R. Reimann, *Physica Status Solidi (a)* **1973**, *16*(1), 187–196.

[126] J. Schoonman, *Solid State Ionics* **1980**, *1*(1-2), 121–131.

[127] D. R. Lide, *CRC Handbook of Chemistry and Physics*, **2003**.

[128] H. Ohno, S. Konishi, K. Noda, H. Takeshita, H. Yoshida, H. Watanabe, T. Matsuo, *Journal of Nuclear Materials* **1983**, *118*(2-3), 242–247.

[129] P. W. M. Jacobs, M. L. Vernon, *J. Chem. Soc. Faraday Trans.* **1990**, *86*(8), 1233–1238.

[130] J. L. Gavartin, A. L. Shluger, C. R. Catlow, *Journal of Physics: Condensed Matter* **1993**, *5*(40), 7397–7408.

[131] A. V. Chadwick, *Philosophical Magazine A* **1991**, *64*(5), 983–998.

[132] A. De Viat, M. J. Gillan, J. S. Lin, M. C. Payne, I. Stich, L. J. Clarke, *Physical Review Letters* **1992**, *68*(22), 3319–3323.

[133] P. Balaya, H. Li, L. Kienle, J. Maier, *Advanced Functional Materials* **2003**, *13*(8), 621–625.

[134] S. Lubke, H.-D. Wiemhofer, *Solid State Ionics* **1999**, *117*(3-4), 229–243.

[135] D. Depla, S. Mahieu, *Reactive Sputter Deposition*, Bd. 109, Springer, **2008**.

[136] R. H. Lamoreaux, D. L. Hildenbrand, *Journal of Physical and Chemical Reference Data* **1984**, *13*(1), 151–173.

[137] H. Kimura, M. Asano, K. Kubo, *Journal of Nuclear Materials* **1981**, *97*(3), 259–264.

[138] V. Piacente, S. Foglia, P. Scardala, *Journal of Alloys and Compounds* **1991**, *177*(1), 17–30.

[139] H. Kudo, C. H. Wu, H. R. Ihle, *Journal of Nuclear Materials* **1978**, *78*(2), 380–389.

[140] A. Wangperawong, S. M. Herron, R. R. Runser, C. Hägglund, J. T. Tanskanen, H.-B.-R. Lee, B. M. Clemens, S. F. Bent, *Applied Physics Letters* **2013**, *103*(5), 052105.

[141] T. Shibata, Y. Muranushi, T. Miura, T. Kishi, *Journal of Materials Science* **1991**, *26*(18), 5107–5112.

[142] J. Maier, *Berichte der Bunsen-Gesellschaft für Physikalische Chemie* **1986**, *90*, 26–33.

[143] J. Maier, *Solid State Ionics* **1987**, *23*(1-2), 59–67.

[144] S. P. Mitoff, *J. Chem. Phys.* **1962**, *36*, 1383.

[145] R. J. Brook, J. Yee, F. A. Kröger, *Journal of the American Ceramic Society* **1971**, *54*(9), 444–451.

[146] D. S. Park, A. S. Nowick, *Journal of Physics and Chemistry of Solids* **1976**, *37*, 607–617.

[147] G. Geschwind, *Journal of Physics and Chemistry of Solids* **1969**, *30*(6), 1631–1635.

[148] K. K. Adepalli, M. Kelsch, R. Merkle, J. Maier, *Physical Chemistry Chemical Physics* **2014**, *16*(16), 4942–4951.

[149] J. Schoonman, *Journal of The Electrochemical Society* **1979**, *126*(8), 1385.

[150] S. Hull, P. Berastegui, S. G. Eriksson, N. J. Gardner, *Journal of Physics Condensed Matter* **1998**, *10*(38), 8429–8446.

[151] T. Krahl, G. Scholz, E. Kemnitz, *The Journal of Physical Chemistry C* **2014**, *118*(36), 21066–21074.

[152] A. Düvel, J. Bednarcik, V. Šepelák, P. Heitjans, *Journal of Physical Chemistry C* **2014**, *118*(13), 7117–7129.

[153] C. Zhu, R. E. Usiskin, Y. Yu, J. Maier, *Science* **2017**, *358*(6369).

[154] R. E. Usiskin, J. Maier, *Physical Chemistry Chemical Physics* **2018**, *20*(24), 16449–16462.

[155] S. Lorger, R. E. Usiskin, J. Maier, *Advanced Functional Materials*, *29*, 1807688.

[156] S. Wenzel, S. Randau, T. Leichtweiß, D. A. Weber, J. Sann, W. G. Zeier, J. Janek, *Chemistry of Materials* **2016**, *28*(7), 2400–2407.

[157] S. Wenzel, S. J. Sedlmaier, C. Dietrich, W. G. Zeier, J. Janek, *Solid State Ionics* **2018**, *318*(February 2017), 102–112.

[158] S. Wenzel, D. A. Weber, T. Leichtweiss, M. R. Busche, J. Sann, J. Janek, *Solid State Ionics* **2016**, *286*, 24–33.

[159] A. D. Reed, D. Lazarus, *Physical Review B* **1983**, *27*(10), 6504–6506.